PACIFIC EARTHQUAKE ENGINEERING RESEARCH CENTER

Final Report of the NGA-West2 Directivity Working Group

Paul Spudich
Editor
Chair, Directivity Working Group
Earthquake Science Center
U.S. Geological Survey
Menlo Park, California

Jeffrey R. Bayless
URS Corporation
Los Angeles, California

Jack W. Baker
Department of Civil and Environmental Engineering
Stanford University

Brian S.J. Chiou
California Department of Transportation
Sacramento, California

Badie Rowshandel
California Department of Conservation and California Earthquake Authority
Sacramento, California

Shrey K. Shahi
Department of Civil and Environmental Engineering
Stanford University

Paul Somerville
URS Corporation
Los Angeles, California

PEER 2013/09
MAY 2013

Final Report of the NGA-West2 Directivity Working Group

Paul Spudich
Editor
Chair, Directivity Working Group
Earthquake Science Center
U.S. Geological Survey
Menlo Park, California

Jeffrey R. Bayless
URS Corporation
Los Angeles, California

Badie Rowshandel
California Department of Conservation
and
California Earthquake Authority
Sacramento, California

Jack W. Baker
Department of Civil and
Environmental Engineering
Stanford University

Shrey K. Shahi
Department of Civil and
Environmental Engineering
Stanford University

Brian S.J. Chiou
California Department of
Transportation
Sacramento, California

Paul Somerville
URS Corporation
Los Angeles, California

PEER Report 2013/09
Pacific Earthquake Engineering Research Center
Headquarters at the University of California, Berkeley

May 2013

ABSTRACT

The 2008 Next Generation Attenuation (NGA-West1) ground motion prediction equations (GMPEs) did not include directivity; it was implemented as a post-facto correction without guidance for its application. The NGA-West2 GMPEs may be developed including the effects of directivity. Four directivity models (DMs) have been developed based on data from the NGA-West2 database and based on numerical simulations of large strike-slip and reverse-slip earthquake. All DMs avoid the use of normalized fault dimension, enabling them to scale up to the largest earthquakes sensibly. Models by Shahi and Baker, Spudich and Chiou, and by Rowshandel are explicitly "narrow-band" (in which the effect of directivity is maximum at a specific period which is a function of earthquake magnitude). The model by Bayless and Somerville is the only model in this report that predicts directivity for fault-normal and fault-parallel motions as well as azimuthally averaged motion. Functional forms and preliminary coefficients of the DMs are presented in this report, but the final coefficients should be produced by including the directivity functional forms *ab initio* in the development of a GMPE. Also shown is a comparison of maps of the directivity amplification from the various DMs applied to a set of test rupture geometries. This comparison suggests that the directivity model predictions are strongly influenced by effects of their assumptions, and more than one model should be used for site-specific studies of directivity from ruptures dipping less than about 65°.

Bayless and Somerville present an improved version of the classic Somerville et al. [*Seismol. Res. Let.* 1997] model, which retains that model's computational simplicity but updates the model with new data and a better functional form. Major changes include rupture-length denormalization, a modified dependence on site azimuth, use of azimuth tapers to obviate the need for an excluded zone, and extension of the algorithm to allow directivity calculations for complicated, noncontiguous rupture zones. A set of coefficients is presented that is adequate for simulating directivity for several different GMPEs.

The directivity model of Rowshandel presented in this report is a major modification of the earlier models developed by the author. Specifically, in comparison with the earlier versions, several major improvements are made: (i) Rupture length de-normalization is used, (ii) in the new model the direction of rupture and the direction of slip both contribute to directivity, and (iii) Unlike the older model, the model presented here is a "narrow-band" model. Many analyses have been performed to assess and quantify the potential impact of the model on the uncertainty term in GMPEs. A few test results based on earthquakes in the NGA-W2 database are also presented.

The Shahi and Baker model is specifically aimed at predicting the characteristics of impulsive ground motions often found at short (< 10 km) distances from fault ruptures (i.e., Lucerne station in the 1992 Landers earthquake). Because the presence of a directivity pulse amplifies spectral acceleration in a narrow band of periods close to the pulse period, their model consists of a wide-band spectral shape plus a superposed narrow-band spectral shape that is multiplied by a logistic variable which is 1 if the pulse is present and zero otherwise. The Shahi and Baker model is the narrowest of the narrow-band models in this report.

Spudich and Chiou present a modified version of the Spudich and Chiou [*Earthquake Spectra* 2008] directivity model. This new model retains the use of Isochrone Directivity Parameter *IDP* as the predictor. However, the new model has the following differences: (1) It is

a “narrow-band” model, and (2) the predictor *IDP* is “centered” by subtracting from it the average *IDP* computed over a “racetrack” of constant R_{Rup} or R_{JB}. Coefficients of a preliminary model are given.

Chiou and Spudich introduce a new directivity predictor, the Direct Point Parameter (*DPP*), although they do not present empirically derived coefficients, so it does not presently constitute a 'model.' The *DPP*, like the *IDP*, is based on isochrone theory but has a stronger theoretical underpinning, as it is based on a special point on a rupture (called the “direct point”) that is more closely correlated with directivity than the *IDP* “closest point,” (point on the fault closest to the site where ground motions are to be evaluated). Because it does not depend on closest point, it is less likely a user’s site will unknowingly be on the high or low side of a discontinuity in the predictor.

ACKNOWLEDGMENTS

This study was sponsored by the Pacific Earthquake Engineering Research Center (PEER) and funded by the California Earthquake Authority, California Department of Transportation, and the Pacific Gas & Electric Company. Any opinions, findings, and conclusions or recommendations expressed in this material are those of the authors and do not necessarily reflect those of the above-mentioned agencies.

During the several years duration of this project, many, many people helped us in innumerable ways, such as providing information about rupture models, stations, etc. To all these people we extend our sincere thanks, and we apologize that we cannot list you all by name, because surely we will omit some. Special thanks go to Jennie Watson-Lamprey, who participated in much of the work and whose ideas contributed to the improvement of our directivity models, but whose directivity model was not quite ready for publication when this report was assembled. D.M. Boore, J.B. Fletcher, B. Rowshandel, and S. Mazzoni provided helpful reviews. We thank also Heidi Tremayne, Claire Johnson, and especially Ann Parker for their editorial work to transform a heterogeneous mish-mash of text into this nicely formatted document.

TABLE OF CONTENTS

LIST OF FIGURES

LIST OF TABLES

1 Overview and Comparison of the NGA-West2 Directivity Models

Paul Spudich and Badie Rowshandel

1.1 INTRODUCTION

The term "directivity" as used in the engineering-seismology literature is a catch-all term meant to describe all the factors that cause ground motion amplitudes and polarization to vary at constant distance from an earthquake rupture. These factors include directivity as known by the seismologist, namely, the ground motion amplitude enhancement caused by the propagation of the rupture front. In the engineering seismology literature [e.g. Somerville et al. 1997], several other physical factors which are spatially correlated with regions of high directivity have been lumped under the rubric "directivity," for example: (1) The tendency for high slip zones to be displaced from earthquake hypocenters [Mai et al. 2005], which causes the largest ground motions to be similarly displaced, (2) the tendency for high slip zones to be spatially compact, which can cause short duration pulses of ground motions, and (3) the double-couple radiation pattern, which places fault-normal motions in zones with high directivity.

1.1.1 Problems in the 2008 NGA-West Approach to Directivity

In the initial Next Generation Attenuation (NGA-West, http://peer.berkeley.edu/ngawest/) project that culminated in the 2008 issue of *Earthquake Spectra* (v. 24, no. 1), directivity was not included as an explicit term in the ground motion prediction equations (GMPEs) that were developed. Instead, directivity functions were developed (e.g., Spudich and Chiou [2008]; Rowshandel [2010]) as *post hoc* "corrections" to the median of a NGA GMPE by fitting directivity functional forms to the residuals of that GMPE. Applying these directivity corrections in practice is challenging, stemming from the facts that the average directivity effect in the observed dataset is implicitly included in the median of a 2008 NGA GMPE, and the reference directivity condition corresponding to that median motion is unclear. The latter could lead to unacceptable outcomes (such as shifting the median of corrected motions over the footprint of a large fault to a level higher than the GMPE median) when a directivity correction is applied with respect to a wrong reference condition.

This approach also poses several problems to the statistical inference of NGA models. For example, there is a question of whether the estimated median is biased due to sampling bias in data. For example, suppose the entire set of M6 events in NGA dataset consisted of the four recordings of the 1966 Parkfield earthquake (Figure 1.1). These stations were all in the forward directivity region (Figure 1.2) and thus likely recorded higher than average motion at long spectral periods.

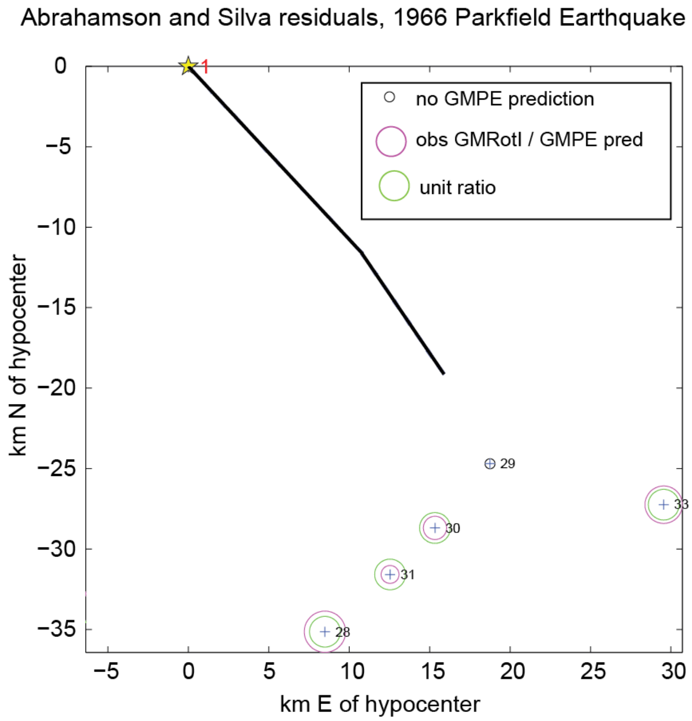

Figure 1.1 **Map of 1966 Parkfield earthquake and total residuals from the Abrahamson and Silva [2008] GMPE. Blue line shows fault trace, star shows epicenter. Crosses show station locations, radius of magenta circles proportional to the residual, i.e., the ratio of observed GMRotI50 [Boore et al. 2006] to GMPE-predicted pseudo-spectral acceleration at 3 sec period. Green circle shows 1:1 ratio.**

On the average, the Abrahamson and Silva [2008] GMPE fits data in the forward direction well, including the probable directivity amplification in the observed ground motions. A non-directive GMPE fit to the Parkfield data would fit them on the average and hence seriously overestimate the median of M 6 earthquake. Potential directivity bias in the entire NGA dataset was not systematically investigated by the post hoc directivity model developers and thus could not be completely ruled out. Another problem of the *post hoc* "correction" process is that some GMPE developers deliberately allowed misfits to the data in order to smooth their predicted motions as functions of periods. The addition of a directivity correction can undo the smoothing intended by the GMPE developers.

1.1.2 Research Plan

In the Next Generation Attenuation West2 (NGA-West2, http://peer.berkeley.edu/ngawest2/) project it was decided by NGA-West2 GMPE developers that ideally the directivity functional form should be included in GMPEs *ab initio*, with its coefficient determined simultaneously with all the other GMPE coefficients (for example the coefficient of the hanging wall effect). Furthermore, the GMPE should be constructed so that if the directivity term were set to zero, the resulting GMPE predicted the median motion for an unbiased directivity condition. To accomplish this, several steps were required.

1. The directivity modelers needed to update their functional forms in light of post-2008 theoretical advances and in light of the new (post-NGAWest) earthquake data available.
2. The directivity modelers were to "center" their predictors, in other words subtract from their predictor (for example, the IDP) its average value around a racetrack of constant Rrup or Rjb. See Spudich and Chiou (this volume) for a more detailed discussion of this centering.
3. The directivity modelers optionally needed to develop approximate coefficients for their new models with respect to one or more of the available GMPEs, so that the GMPE developers had an initial set of coefficients. These coefficients were to be developed by regressing the directivity model predictions against residuals of NGA West2 ground motion database compared with NGA-West (1) or interim GMPEs.
4. The GMPE developers were free to choose which, if any, of the directivity models they wanted to include in their updated GMPE. They were to determine the final coefficients of their new models by including the directivity model functional form in their regressions.

Because the final GMPE-developer-derived coefficients are not available at this time, **the amplitudes of the predicted directivity from each model should be regarded as preliminary, subject to change.**

At the time of this writing, it appears that most GMPE developers will choose to include directivity in their GMPEs by introducing a spatially variable sigma. The Chiou and Youngs team will probably choose to use the Direct Point Parameter (DPP) model (Chiou and Spudich, this volume).

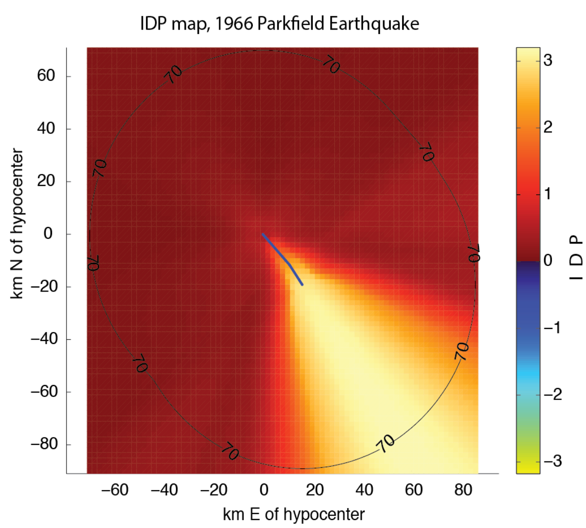

Figure 1.2 **Map of Isochrone Directivity Parameter (IDP [Spudich and Chiou 2008]) around the 1966 Parkfield earthquake. The IDP is by definition positive. The average IDP out to rupture distance Rrup = 70 km (black line) is 0.7621.**

1.1.3 Improvements in NGA-West2

As discussed above, an improvement in NGA-West2 is that one or more of the GMPEs will be developed with a directivity functional form and the associated coefficients will be determined by the NGA GMPE developers (not the directivity model developers) along with the other GMPE coefficients. This is likely to lead to a larger size of the directivity effects, offset by perhaps a smaller magnitude scaling in median motion. **Consequently, any directivity coefficients estimated and presented in this document are likely to change when the directivity functional forms are included in the regressions for GMPE coefficients**. Some directivity modelers have performed extensive calculations to determine the spatial average values of their directivity parameters, to be used to determine the state of "reference directivity condition."

The directivity models themselves have improved in two significant ways as part of the NGA-West2 project. First, all the models now use site distances (e.g., rupture distance Rrup or Joyner-Boore distances Rjb) in km rather than normalizing the dimensions to fault length, as was done by many previous directivity models, e.g., Somerville et al. [1997]. Use of normalized site distances led to the problem indicated in Figure 1.3 where a site at an angle θ= 0° off strike and a distance s = 150 km from the epicenter of a M 7.5 earthquake with length L = 150 km had a Somerville et al. [1999] directivity parameter $Xcos(\theta) = {}^{s}/_{L}\, cos(\theta) = 1$, whereas a similar site 150 km from the epicenter of a 300-km-long M 7.8 earthquake has a directivity parameter of 0.5, meaning that it would experience half the directivity of the site 150 km from the epicenter of a M 7.5 earthquake.

Figure 1.3. Unequal values of Somerville et al. [1997] directivity parameter at sites 150 km from the epicenters of a M 7.5 and a M 7.8 earthquake.

Second, the Rowshandel, Shahi and Baker, and the Spudich and Chiou models are now explicitly "narrow-band" models, in which the directivity peaks at a specific period and decreases away from the peak on both sides of the peak period. The peak period itself increases with magnitude, consistent with the observed dependence of pulse period with earthquake magnitude.

1.2 DEFINITION OF RUPTURE GEOMETRY

To understand the directivity model discussion, it is helpful to understand how earthquake rupture geometry was represented in the NGA-West2 project. In particular, it is crucial to understand the distinction between a *segment* and a *fault* or *strand*.

- *Segment* - A planar quadrilateral, not necessarily rectangular, slip surface having a horizontal top and bottom.

- *Fault* or *Strand* - A slip surface composed of one or more contiguous planar quadrilaterals (segments) that are used to model the change in strike direction and dip. Only a single hypocenter is permitted for a fault or strand.

We impose the following restrictions:

1. The top edges of all quadrilaterals in a fault are horizontal and at equal depth;
2. The bottom edges of all quadrilaterals in a fault are horizontal and at equal depth;
3. All quadrilaterals (except those on the ends of the fault) are joined to their neighbors along the dipping edges with no gaps.
4. Quadrilaterals in a single fault may have differing dips, but dip is less than or equal to 90°, and the strike direction of a quadrilateral is determined by the requirement that the segment dips to the right when looking along-strike (the convention used in Aki and Richards [1980]);
5. The strike vectors of two adjacent quadrilaterals should not converge or diverge. To represent ruptures like the 1995 Kobe, Japan, earthquake, in which the two faults' strikes diverge, it is necessary to represent them as two separate faults, each with its own hypocenter.

Seven earthquakes in the NGA-West2 database were described as multi-fault ruptures, which required special treatment by the directivity modelers because of the multiplicity of hypocenters in each earthquake. Directivity modelers have modeled the directivity effects due to such multi-fault earthquakes differently.

1.3 COMPARISON OF DIRECTIVITY MODELS

1.3.1 The Physics of Directivity as Manifested in the NGA-West2 Models

All NGA-West2 models include the two Somerville et al. [1997] basic insights, that

- Principle 1: Ground motions are largest where the SH radiation pattern lobe (maximum in the direction of slip) aligns with the direction of rupture propagation and the direction to the site. Considering a small earthquake as a point double-force-couple source, one force-couple is aligned with the slip vectors on each side of the fault. The so-called "fault-normal" motion is aligned with the other force-couple. This principle implies that the directivity amplification will be greatest in some cone or wedge radiating from the hypocenter in the direction of rupture because both true directivity and the SH radiation pattern have narrow zones of amplification.
- Principle 2: Directivity is stronger when the distance the rupture travels is longer.

Principle 2 is less strongly grounded in theory than principle 1. Spudich and Chiou [2008] noted that full-waveform simulations of long strike-slip ruptures show that the maximum directivity amplification occurs within the ends of the fault, even for heterogeneous but uniform slip distributions. Schmedes and Archuleta [2008] explained this phenomenon, for uniform homogeneous slip distributions, using isochrone theory. However, without a full understanding of this phenomenon for heterogeneous rupture, all of the directivity modelers have chosen the conservative approach of forbidding directivity amplification to decay with distance from the hypocenter along the fault trace.

Both principle 1 and isochrone theory describe the directivity of S waves. However, because the peak response can occur at any time in a seismogram, the response spectra could be dominated by the S wave in some records, and by surface waves in another records. Consequently, either principle 1 or isochrone theory has been applied by all the directivity modelers to both S waves, S coda, and surface waves in the data (the exception being Shahi and Baker, who, by identifying pulses, are selecting for S waves). Surface wave directivity is expected to behave similarly to S wave directivity (in fact, surface waves were used in the classic reference defining directivity, Ben-Menahem [1961]). S-coda caused by site effects would also be affected by directivity similarly to S waves, so it is only the typically small amplitude later coda, backscattered from many directions, that would not be modeled by S directivity.

The main physical simplification that most models use is the replacement of the effects of a finite fault with use of the point on the fault closest to a site of interest. One of the negative consequences of the use of the closest point is that the closest point is a discontinuous function of the site position; small shifts of the site can cause a large jump in the closest point. An example of the discontinuities is shown in Figure 1.4. Rowshandel's model produces the smoothest maps of directivity amplification because it integrates over the entire fault. The DPP parameter of Chiou and Spudich uses a line integral, and consequently is smoother than the IDP parameter.

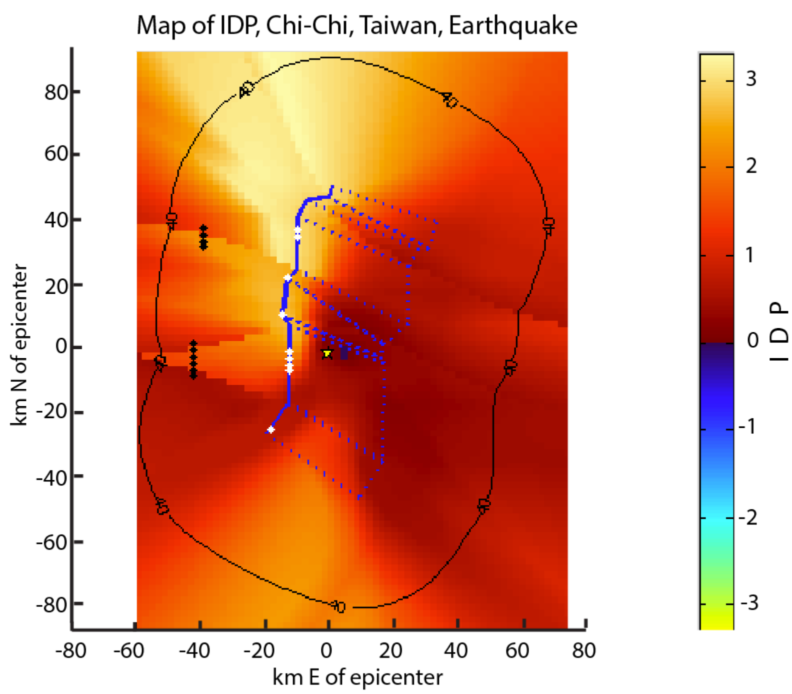

Figure 1.4 **IDP for Chi-Chi, Taiwan, earthquake. Note discontinuities. White dots are closest points to lines of sites shown by black dots. Note that discontinuities in IDP correspond to jumps in the closest point.**

1.3.2 Preliminary Regressions against Data

As part of Step 3 of the Research Plan (see above), preliminary directivity models have been developed by most or all modelers based on sets of ground motion intra-event residuals. A mixed-effects model [Abrahamson and Youngs 1992; Joyner and Boore 1993] with a single free parameter was used to calculate intra-event residuals from the GMPE of every developer team. Some developer teams had created preliminary new GMPEs, so residuals were calculated based on that experience. For other developer teams, residuals were calculated with respect to their 2008 GMPEs. Note that in that case Rotd50 data were differed with GMRotI50 predictions. Directivity modelers chose from among these residual sets and determined preliminary coefficients based upon regressions to fit the residuals.

Table 1.1 Residual sets available to directivity modelers.

Residual w.r.t. which GMPE?	Component	Comment
Interim AS	All	Calc by P. Spudich; max Rjb = 50 and 200 km
BA2008*	All	Calc by P. Spudich; max Rjb = 50 and 200 km
Interim CB	All	Calc by P. Spudich; max Rjb = 50 and 80 km
CY2008*	All	Calc by P. Spudich; max Rjb = 50 and 70 km
Idriss 2008*	All	Calc by P. Spudich; max Rjb = 50 and 200 km
Interim AS	Rotd50	Calc by L. Al-Atik
Interim CB	Rotd50	Calc by T. Ancheta -used CB2008 functional forms and solved for coefs.
CY2008*	SN / SP	Calc by L. Al-Atik
CB2008*	SN / SP	Calc by L. Al-Atik for S4 and H11 basin models
CY2008*	Rotd50	Calc by L. Al-Atik

* AS = Abrahamson and Silva, BA = Boore and Atkinson, CB = Campbell and Bozorgnia, CY = Chiou and Youngs.

1.3.3 Test Cases

Maps of directivity amplification of near-fault ground motion predicted by several directivity models are compared for a variety of pre-determined test earthquake geometries and are summarized in this section. These directivity models have functional forms that depend on the source-site geometry and the source magnitude, and the functional forms are multiplied by empirical coefficients as determined in Section 1.3.2.

Results are presented for a variety of earthquake rupture geometries, as decided on collectively by the authors of the considered models. Detailed information regarding these rupture geometries is available at http://peer.berkeley.edu/ngawest2_wg/directivity-wg/data, and a brief summary is provided here (Table 1.2). Test models consisted of six pure strike-slip events (ss1 – ss5, ss7) on vertical faults, with magnitudes ranging from 5.5 to 8.1, one oblique slip rupture (so6) on a steeply dipping plane having magnitude 7.2, 6 reverse events (rv1 – rv5, rv7) of magnitude 5.5 – 7.5 on planes dipping 30° – 45°, and a 30° dipping oblique slip event (ro6) of magnitude 7.0 (Table 1.2). All faults were planar, except for ss5 and rv7, which had 45° bends. A 45° bend is uncommon for a vertical strike-slip fault, but reverse faults having 90° bends can be found in the SCEC Community Fault Model (http://structure.harvard.edu/cfm/index.html). Hypocenters of all events were about 10% of the fault length from an end of each fault, in order to maximize the forward and minimize the backward directivity. The periods calculated were 1, 3, 5, 7.5, and 10 sec. Not all directivity modelers calculated all models.

Table 1.2 Definition of test models for comparison of directivity predictions.

Test model code	Mechanism	Mw	dip (dg)	rake (dg)	bend angle (dg)	Rupture top (km) Ztop	Hypocenter distance updip from fault bottom (km)
ss1	Strike-slip	5.5	90	180	0	7	2
ss2	Strike-slip	6.5	90	180	0	0	2
ss3	Strike-slip	7.2	90	180	0	0	5
ss4	Strike-slip	7.8	90	180	0	0	5
ss5	Strike-slip	6.7	90	180	45	0	5
so6	SS-oblique	7.2	70	135	0	0	5
ss7	Strike-slip	8.1	90	180	0	0	5
rv1	Reverse	5.5	45	90	0	5	2
rv2	Reverse	6.5	45	90	0	0	4
rv3	Reverse	6.5	45	90	0	5	4
rv4	Reverse	7	30	90	0	0	8
rv5	Reverse	7.5	30	90	0	0	8
ro6	RV-oblique	7	30	135	0	0	8
rv7	Reverse	7.5	30	90	45	0	8

1.3.4 Predictive Models

Results from four predictive models are available at this time. The models are listed in Table 1.3 below.

Table 1.3 Table of directivity models and predictors.

Model	Bayless & Somerville	Chiou & Spudich	Rowshandel	Shahi & Baker	Spudich & Chiou
Abbreviation	bay12	(none)	rowv4	sha12	sc3b
Predictor	f_{geom}	DPP	ξ	s, θ, d, ϕ	IDP
Directivity term	f_D	n/a[1]	f_D	$I_{direc} \cdot \ln Amp(T, T_p)$	$\hat{f}_D$
M range	6.0-8.0	n/a[1]	5.5-8.0	5-7.9	5.75 - 7.9
M taper	5.0 - 6.5	n/a[1]	none	n/a[2]	none
Max distance of directivity effect, D_{max}	$R_{rup} < 80$ km	n/a[1]	period-dependent; 86 km at 10 s 40 km at 1 s	70 km n/a[2]	$R_{rup} < 70$ km
Distance taper	(L or W)/ 2 to (L or W)	n/a[1]	from $D_{max}/2$ to D_{max}	n/a[2]	40 to 70 km
Period range	0.5 - 10 s	n/a[1]	0.5 - 10 s	0.6-10 s	0.5 - 10 s
Bandwidth[3]	Broad-band model	n/a[1]	0.6	0.79*Tp	0.6132
Allowed dip	any	any	any	any	any
Allowed rake	any	any	any	any	any
Allowed bend in strike	Any between segments	n/a[1]	<90°	< 90°	< 90°
Centered predictor?	no	n/a[1]	yes	yes	yes
Number of empirical coefficients	2 per component per period	n/a[1]	3 per component per period	3	6

Model	Bayless & Somerville	Chiou & Spudich	Rowshandel	Shahi & Baker	Spudich & Chiou
Components of motion	RotD50, FN, FP	n/a[1]	RotD50	RotD50, model for arbitrary orientation relative to FP in Shahi and Baker [2011]	RotD50
Physical basis	intuitive model[4] using closest point	isochrone theory based on direct point; result for line source	intuitive model[4] integrating over entire rupture surface	intuitive model[4] for geometry, empirical model for impulsive near-fault ground motions	isochrone theory based on closest point
Flexibility[5]	none	n/a[1]	can include a specific slip distribution; can specify normal or reverse faults		rupture velocity slightly changeable
Representative 10 s intra-event residual before/after	0.635 / 0.621; Section 2.9	n/a[1]	0.601/0.559 Model I 0.601/0.522 Model II; Section 3.2.6	Section 4.5	0.662 / 0.580; Table 5.2

1 Model has not yet been developed.

2 The Shahi and Baker model does not have linear distance tapers that go to zero adjustment at a specific magnitude and distance, but magnitude and distances ranges are provided in the above table based on the range of values associated with identified pulse-like motions, to give an idea as to the ranges over which the model may predict an adjustment.

3 Width parameter of Gaussian function of period.

4 Based on the two principles of Somerville et al. [1997].

5 Non-geometric source factors that the user can vary.

A major difference between the models is that some (Table 1.3) are broad-band and others are narrow-band [Somerville 2003]. Specifically, in some of the models the period- and space-dependences of the directivity amplification are separable, i.e. amplification can be written A(x,T, M) = X(x,M)Y(T), where x is position, T is period, M is magnitude, and X and Y are smooth functions. In separable “broad-band” models like Somerville et al. [1997], Y(T) is a monotonically increasing function of T. Consequently, maps of amplification for a specific earthquake at various periods look the same, except for amplitude. In “narrow-band” models like sha12, rowv4 and sc3b, A(x,T, M) = X(x,M)Y(T,M), and Y(T,M) is peaked at some period related to the magnitude of the earthquake. This difference will be evident in some of the test examples.

Another important difference is that sha12 gives the pseudo-spectral acceleration of a ground motion pulse, which is correlated with directivity but is not exactly the same thing. Pulses are expected to be big only close to ruptures, so the sha12 model has amplitudes concentrated near fault traces.

1.3.5 Results and Observations from Test Cases

This section presents comparisons of spatial pattern of ground motion amplification factor. In other words, an empirical attenuation relation without directivity effect (Sa) can be modified to obtain the spectral acceleration with directivity effects (Sa_{dir}) by the following Equation (1.1):

$$\ln (Sa_{dir}) = \ln (Sa) + f_D \tag{1.1}$$

where f_D is the directivity effect as in Equation (1.2):

$$f_D = c_o + c_1 P \tag{1.2}$$

where P is a directivity parameter like $X \cos\theta$ or the IDP and c_o and c_1 are empirical constants. In the following plots we plot the quantity $exp(f_D)$, which is the ground motion amplification factor. The colorbar scale shows $(exp(f_D) - 1)$ so that if the directivity amplification for a model ranges from 70% to 120% of the nondirective motion, then the colorbar axis runs from 0.7 to 1.2. The quantity plotted for sha12 is CBSB / CBR, which is the ratio of ground motion amplification of two GMPEs. CBSB is the Campbell and Bozorgnia functional form including the Shahi and Baker directivity pulse model fitted to the NGA West2 data, and CBR is the Campbell and Bozorgnia functional form fitted to the NGA West2 data. The ratio CBSB/CBR is not expected to be directly comparable to the other directivity model results because both the magnitude- and distance- dependence change between CBR and CBSB.

Amplification predictions along a cross-section near the fault can also be done online at www.shreyshahi.com/directivity. Amplification comparison software can be downloaded from http://www.shreyshahi.com/directivity/ampcs.html

Two Caveats

- Although the directivity models shown have been fitted to residuals, except for sha12, none has had the underlying GMPE refitted simultaneously. Consequently, **amplitude differences between models might not be significant.** One should primarily look at the spatial distributions of amplitudes.
- The amplifications depicted in this chapter for rowv4 are for the broad-band version of that model. The amplifications for Rowshandel's narrow-

band model have exactly the same spatial distribution as the broad-band model results, but they differ by an untabulated constant factor.

1.3.5.1 Results for Strike-Slip Earthquakes

The directivity models bay12, rowv4, sc3b, and sha12 predict fairly similar patterns of directivity with characteristics of each model that persist over many test rupture geometries. A typical example is M7.2 ss3 in Figure 1.5.

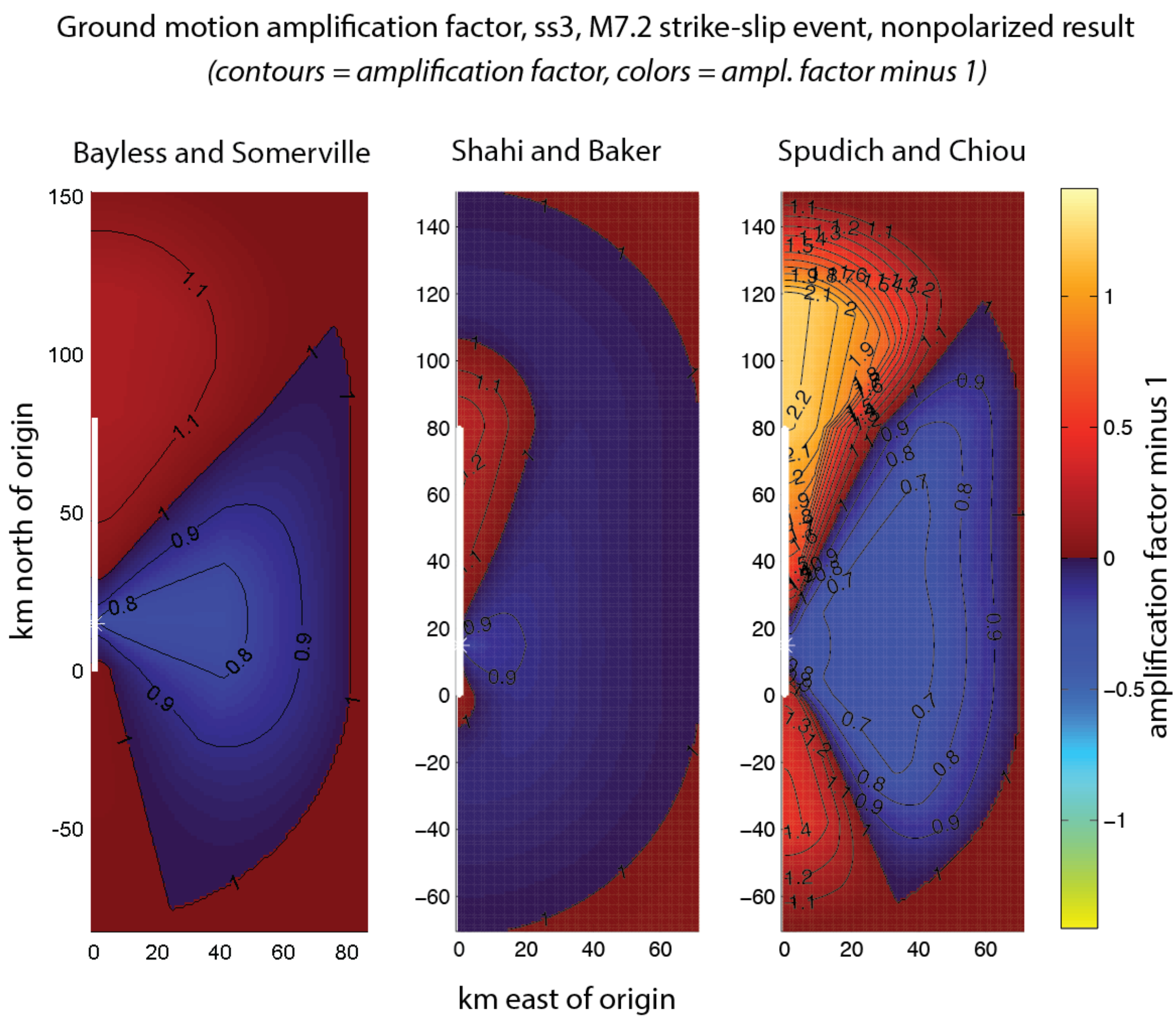

Figure 1.5 Ground motion amplification factor for rupture geometry ss3, M 7.2, comparing models sha12, sc3b, and bay12. Color bar numbers are (amplification factor minus 1). This picture is fairly typical of all strike-slip test geometries.

Relation sha12 (center) keeps the directivity pulse amplification concentrated close to the rupture where pulses are typically found. sc3b (right) and bay12 (left) have fairly similar distributions of amplification. (Results for rowv4 were not available.) We will see, however, that for larger magnitude events bay12 predicts directivity amplification out to much greater distances than the other models.

1.3.5.2 Unnormalized Fault Length and Scaling for Long Strike-Slip Earthquakes

A major advance of NGA West-2 was to provide a setting in which the directivity-scaling of very large earthquakes could be made more physical. A failing of directivity models that use rupture lengths normalized to fault length, like Somerville et al. [1997], is that a site at the end of a short fault can have more directivity than a site at the end of a long fault, as shown earlier in Figure 1.3. Abrahamson [2000] recognized this problem and modified the Somerville et al. [1997] directivity model by capping the X parameter to compensate. All of the NGA West-2 directivity models have been adapted to avoid this problem. In Figure 1.6 we show an example comparing directivity for ss4, a M 7.8 235 km long rupture, with directivity for ss7, a M8.1 400 km long rupture. We omit the result for sha12. The amplification predicted by their directivity model at a spectral acceleration period depends on the period of the pulse, which in turn depends on magnitude. So the amplification at T = 5 sec from a magnitude 7.8 earthquake (ss4) is expected to be different than that from a magnitude 8.1 earthquake (ss7) at the site located same distance down the rupture. Also, when Shahi and Baker include their directivity term, they refit the rest of the GMPE and this changes the magnitude scaling. Because of this, some of the differences in directivity amplification seen in their model are actually due changes in magnitude scaling rather than simply the directivity term. For these reasons, a depiction of their results in the format of Figure 1.6 does not directly illustrate that their directivity term scales logically with rupture length.

It should be noted in Figure 1.6 that the Bayless and Somerville model predicts directivity at much greater distances than the other models (Table 1.3). For the M 8.1 event, ss7, Bayless and Somerville predict directivity amplification out to 400 km perpendicular to the fault, whereas all the other models do not extend much beyond 70 km.

(a)

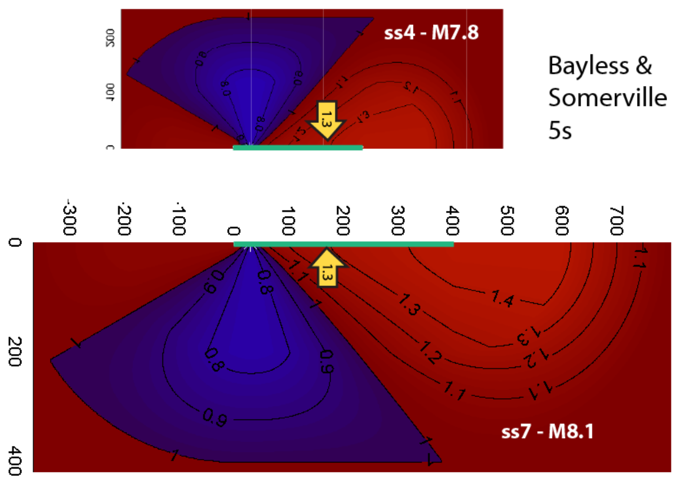

(b)

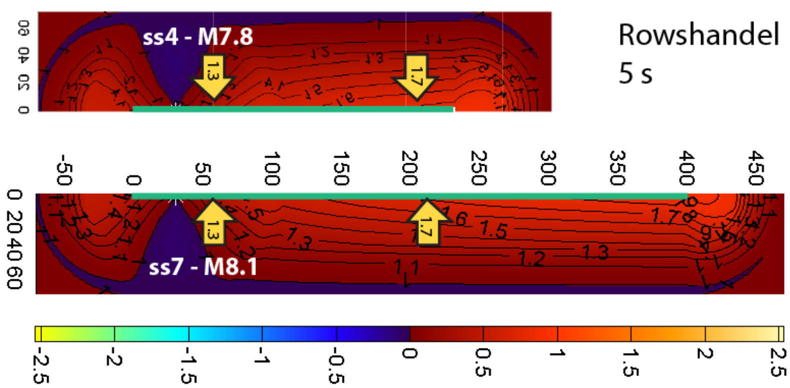

(c)

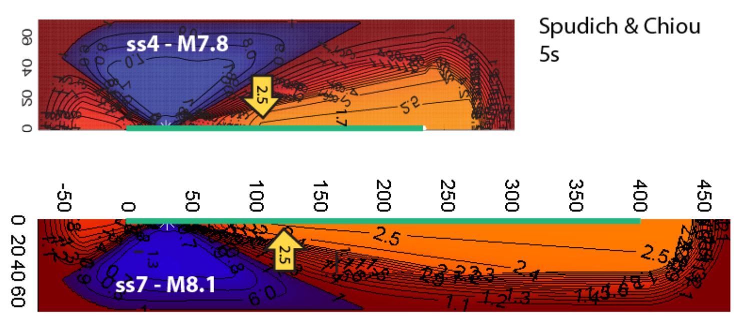

Figure 1.6 **Maps of directivity amplification for models bay12 (top pair) rowv4 (middle pair), and sc3b (bottom pair). Larger map of each pair is for M8.1 400-km-long ss7. Smaller map is the directivity amplification for M7.8 235-km-long ss4. Green arrows show that the directivity amplification at the rightward limit of the zones of rapid directivity growth for ss4 and ss7 rupture models is very similar.**

1.3.5.3 Oblique-Slip Earthquakes

Rupture geometry so6 was modeled after the 1989 Loma Prieta earthquake geometry, which was characterized by a steep dip and oblique slip.

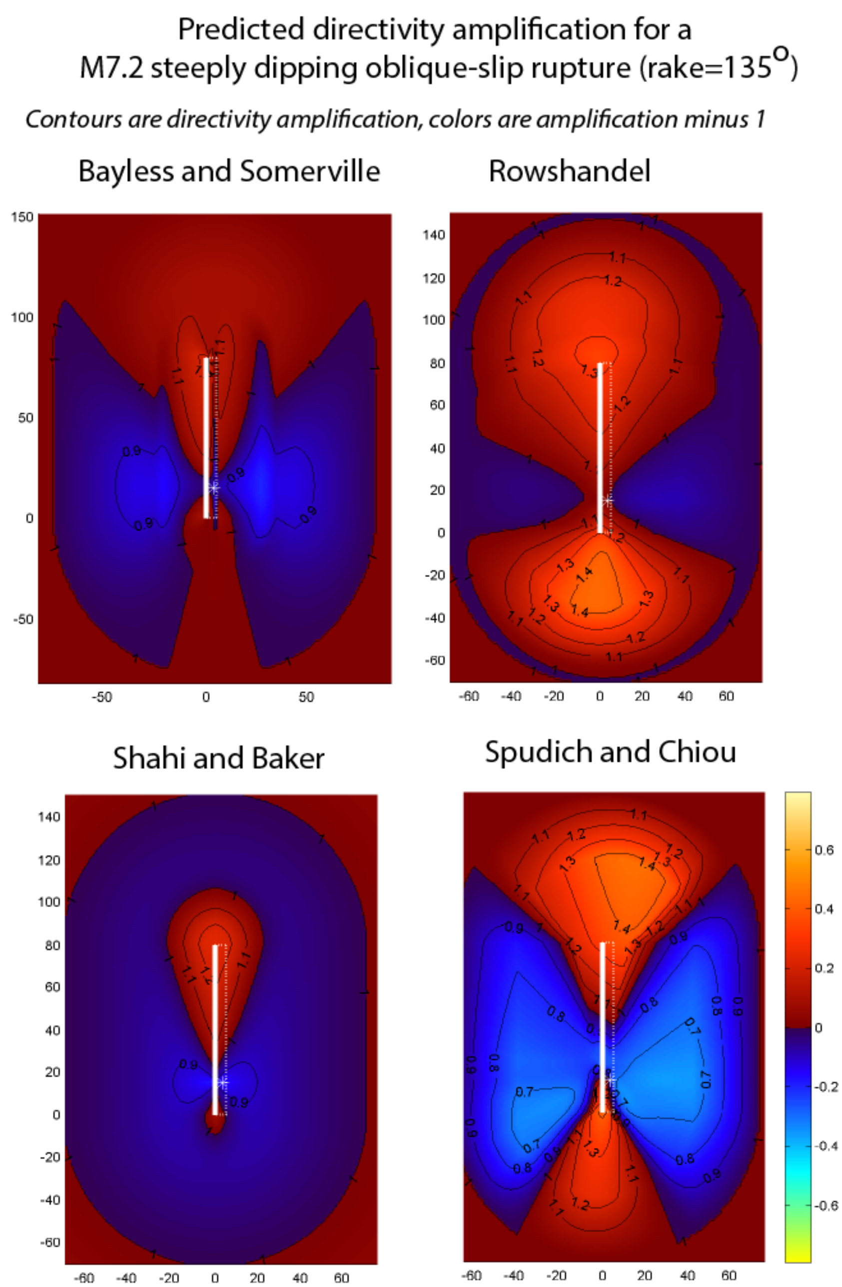

Figure 1.7 Comparison of predicted directivity from models bay12, sha12, sc3b, and rowv4 for M7.2 steeply-dipping oblique-slip test model so6.

Model sha12 has no explicit rake dependence, so the slight asymmetry seen in this model is caused by the slight nonvertical dip of the fault (Figure 1.7). Model sc3b has the strongest rake dependence, owing to its explicit use of rake in the source radiation pattern. The strongest effect is the eastward rotation of the positive lobe north of the fault and the westward rotation of the positive lobe south of the fault. Model rowv4 ground motions have an intermediate perturbation due to oblique slip. The effect of rake rotation in rowv4 might be diminished because the rake and rupture directions are equally weighted. Interestingly, bay12 and rowv4 have their large amplitudes shifted slightly west of the rupture at the north end of the rupture, while sc3b is shifted east at that location.

The effect of rake rotation is more apparent in reverse faulting earthquake ro6, which had a 135° rake.

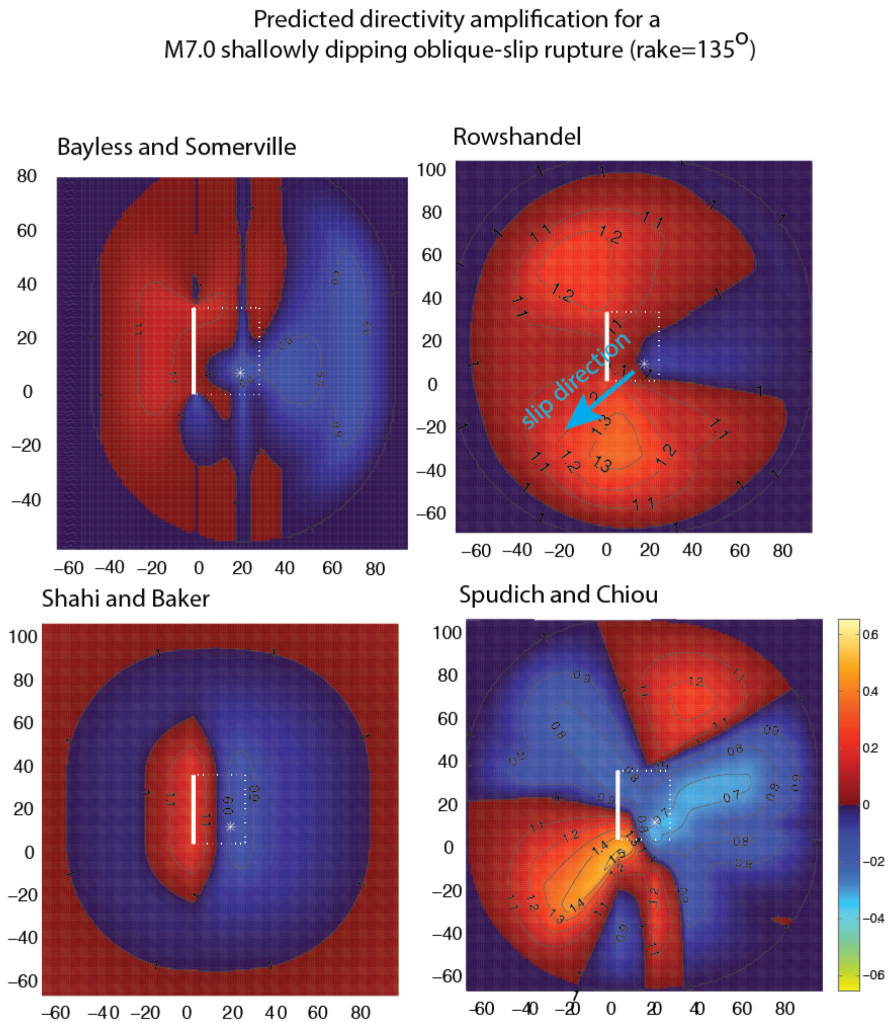

Figure 1.8 Comparison of predicted directivity from models bay12, sha12, sc3b, and rowv4 for M7.0 shallowly-dipping oblique-slip test model ro6.

A very strong tongue of high amplitude pointing SW from the fault is shown in sc3b. This tongue is caused both by the orientation of rake in that direction and also by the fact that the D value is largest for rupture paths from the hypocenter to a corner. The effect of rake is seen in rowv4 through the counterclockwise rotation of all highs and low. We note parenthetically that the directivity predictions of rowv4 and sc3b are almost anti-correlated in the northwest and southeast quadrants. There are strong differences between the predictions. sha12 predicts strong directivity along the entire fault trace. rowv4 has a minimum of directivity over the center of the fault. sc3b has positive directivity on the southern part of the fault and negative directivity along the north end. Also rowv4 predicts directivity amplification to the NW of the N end of the fault whereas sc3b predicts low directivity. bay12 is unique in predicting its maximum directivity to the NW of the fault. sc3b might be affected by the use of the point source radiation pattern of the hypocenter. There is some evidence that the DPP parameter of Chiou and Spudich correlates better with rowv4 maps.

In general, as we will discuss next, the directivity models are in poor agreement for reverse faults.

1.3.5.4 Dipping Faults

Rupture geometry rv4 (Figure 1.9) shows the characteristics common to all reverse faulting tests. rowv4 has strong directivity to the NW, caused by the length of the rupture path from the hypocenter to the NW corner of the fault. The small red island to the SW of the fault is probably also caused by rupture propagation from the hypocenter to the SW corner of the fault. Model sc3b shares some characteristics with rowv4, specifically, it has a tongue of higher amplitudes radiating NW from the fault, probably caused by large D values for rupture paths from the hypocenter to the NW corner. It also has a high amplitude zone just updip from the hypocenter, caused by the point source radiation pattern. Models bay12 and sha12, being untroubled by complicated radiation patterns, predict similar uniform directivity along the fault trace.

Only the Rowshandel model distinguishes between reverse and normal faulting. There are rupture-dynamic reasons [Oglesby et al. 2000] why near-fault motions should be higher for reverse than normal faults, and most GMPEs have mechanism-related terms that yield higher motions for reverse than for normal-faulting ruptures, so it is not clear whether directivity should also be affected by the mechanism. Oglesby et al. [2000] report that even though the stress conditions differ between reverse and normal earthquakes, the average rupture speed does not vary between the two.

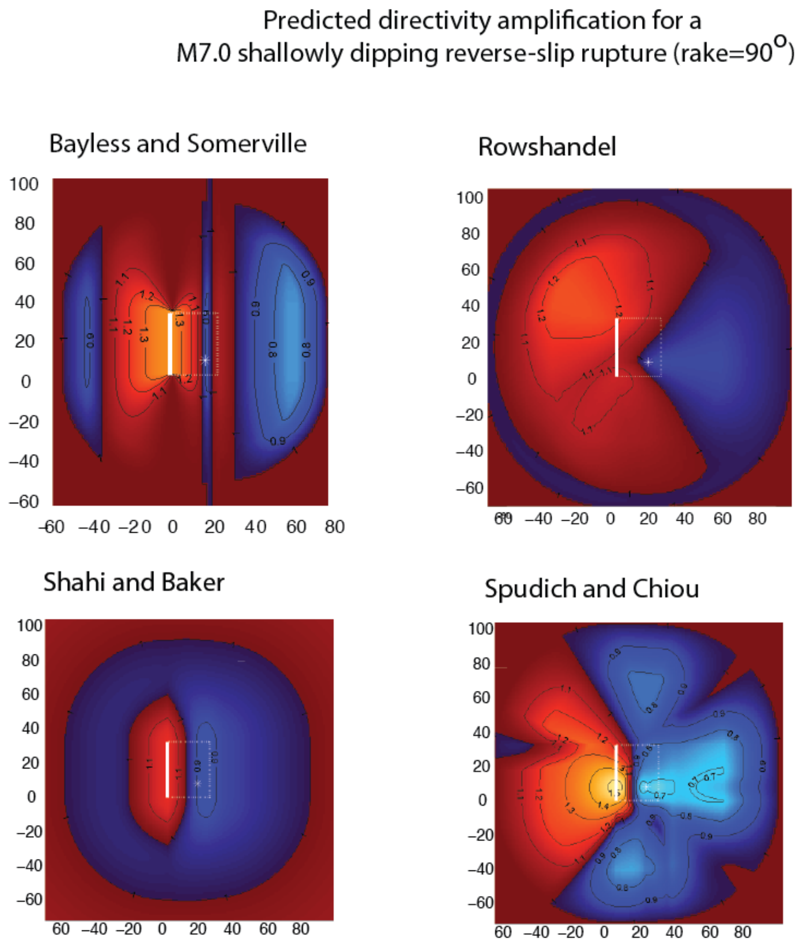

Figure 1.9 **Comparison of predicted directivity from models bay12, sha12, sc3b, and rowv4 for M7.0 shallowly-dipping reverse fault test model rv4 at 5 sec period.**

The most problematic comparison is for model rv7 (Figure 1.10), a reverse fault with a strong bend. Included in this comparison is a result from Bayless and Somerville. This model makes clear that at least for reverse faults, the assumptions of the directivity models have a stronger effect on the predictions than do the data. All models except sha12 predict higher motions on the footwall than on the hanging wall. However, at certain points near the fault trace, the models give quite different predictions. At point A updip from the hypocenter, sc3b has its maximum directive amplification whereas rowv4 is rather low. Similarly, bay12 is highest at the bend in the fault (point B) but rowv4 and sha12 show little amplification. Directivity is high in rowv4 at places where the rupture length is long (e.g., C, D) but these points are barely amplified in bs12 and sc3b. Also, at E on the hanging wall above the junction of the two bottom edges of the segments, bs12 predict amplification whereas rowv4 and sc3b predict deamplification.

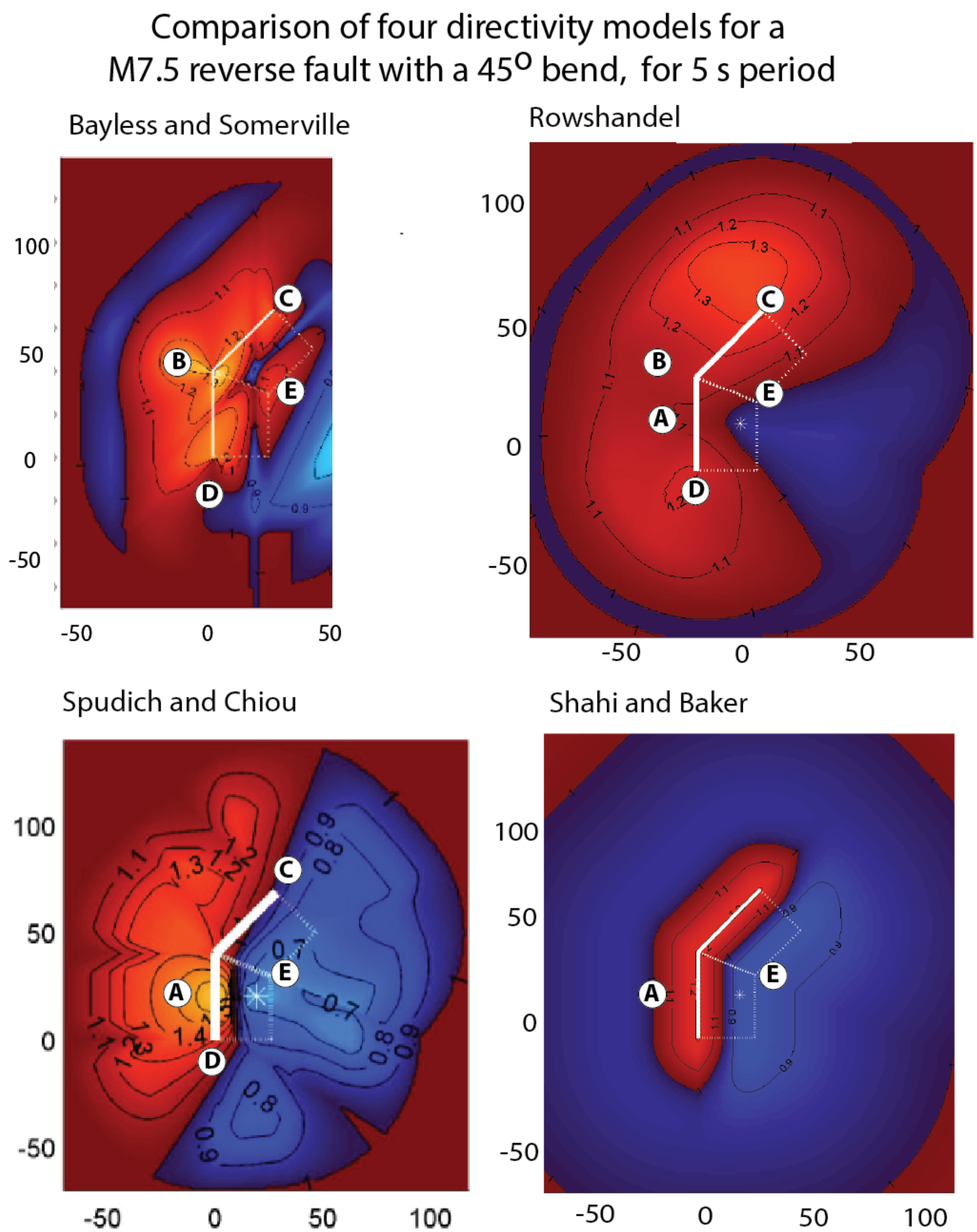

Figure 1.10 **Comparison of directivity models sha12, bs12, sc3b, and rowv4 for rv7, a reverse fault having a 45° bend.**

1.3.5.5 Fault Normal, Fault Parallel, and Non-polarized Motions

Only bay12 explicitly developed directivity models for specific polarizations, with coefficients determined by regression of data, although a polarization model for sha12 appears in the NGA West2 Directionality Final Report [Shahi and Baker 2012b]. In addition, expressions for the polarization direction of ground motions appear in sc3b, but they have not yet been thoroughly compared with data. Figure 1.11 shows an example of the polarization predicted by bay12. Like sc3b, the use of a $\cos(2\theta)$ term in bay12 produces a radiation pattern of a point source at the hypocenter.

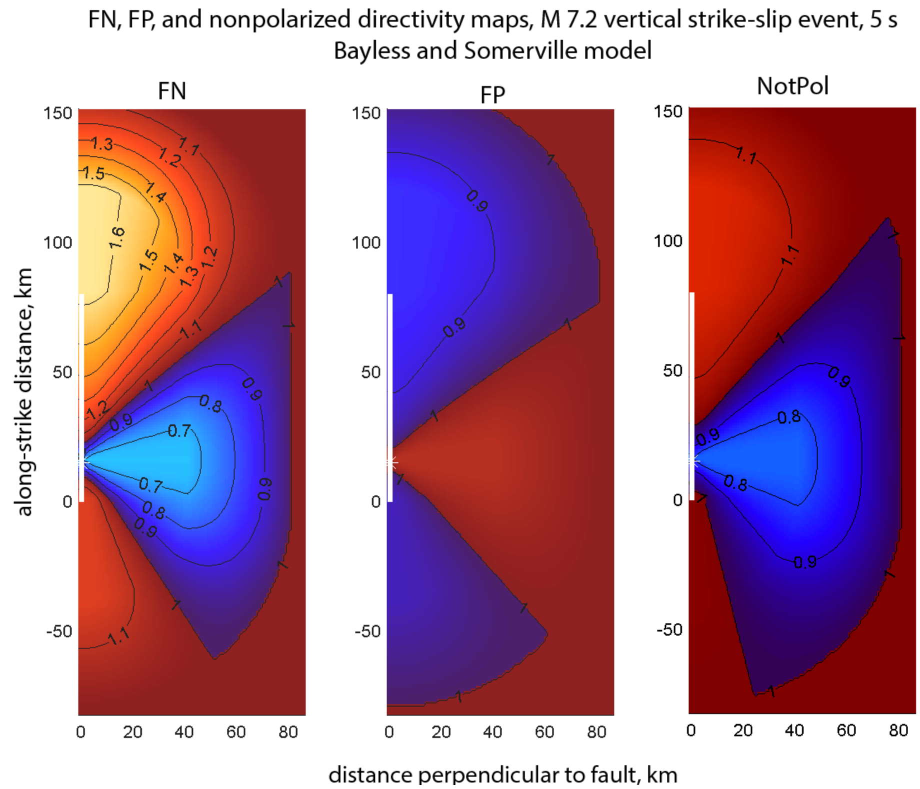

Figure 1.11 Directivity amplification in the FN, FP, and nonpolarized components for test model ss3 for bay12.

This can be seen most clearly in the FP component, where it might be expected for a long fault with relatively uniform slip that the FP motion would be approximately constant along a line parallel to the fault trace.

1.3.5.6 Broad-band, Narrow-band, and All That

Three of the directivity models, sha12, sc3b, and rowv4 claim to be narrow-band, but sha12 is much narrower than the other two models. Figure 1.12 shows that for rv2, sha12 predicts high directivity at 1 s period that disappears entirely by 10 sec. On the other hand, sc3b predicts a directivity amplification that is fairly flat between 3 and 10 sec, and so can be called "narrow-band" only in the sense that it does not rise inexorably as period increases, unlike Somerville et al. [1997] or Spudich and Chiou [2008]. This is not entirely surprising. Model sha12 is explicitly a model of the response spectrum of an impulsive ground motion, i.e., it is a pulse model, and the pseudo-spectral velocity is known to peak at the pulse period while the pseudospectral acceleration has a corner near the pulse period. Models sc3b and row12, on the other hand, included both impulsive and non-impulsive motions in their development, and thus are an average of the two.

The "strength" of "narrow-bandness" in these models directly depends on the size (or the choice) of the bandwidth (sigma) in the Magnitude-Pulse Period relation. In Rowshandel and Spudich and Chiou models, for instance, the bandwidth for individual earthquakes was found to be rather small (e.g., < 0.1–0.4), which would render the model(s) "very narrow band" if applied to individual earthquakes, same as (or even narrower than) the sha12 model. However, moving from individual earthquakes to the entire residual data in NGA-West2, this bandwidth will have to increase to 0.6 or 0.8 (or perhaps even more) in order to preserve the correlations (or linear fits) between directivity parameter(s) and ground motion residuals. It should also be noted that, in reality, a similar transition from "earthquakes-with-pulse" narrow bandwidth to overall (pulse and non-pulse earthquakes) larger bandwidth will have to take place in sha12 model, when the probability of pulse (with a relatively flat pdf) is superimposed on the "conditional" pulse-based narrow-band model.

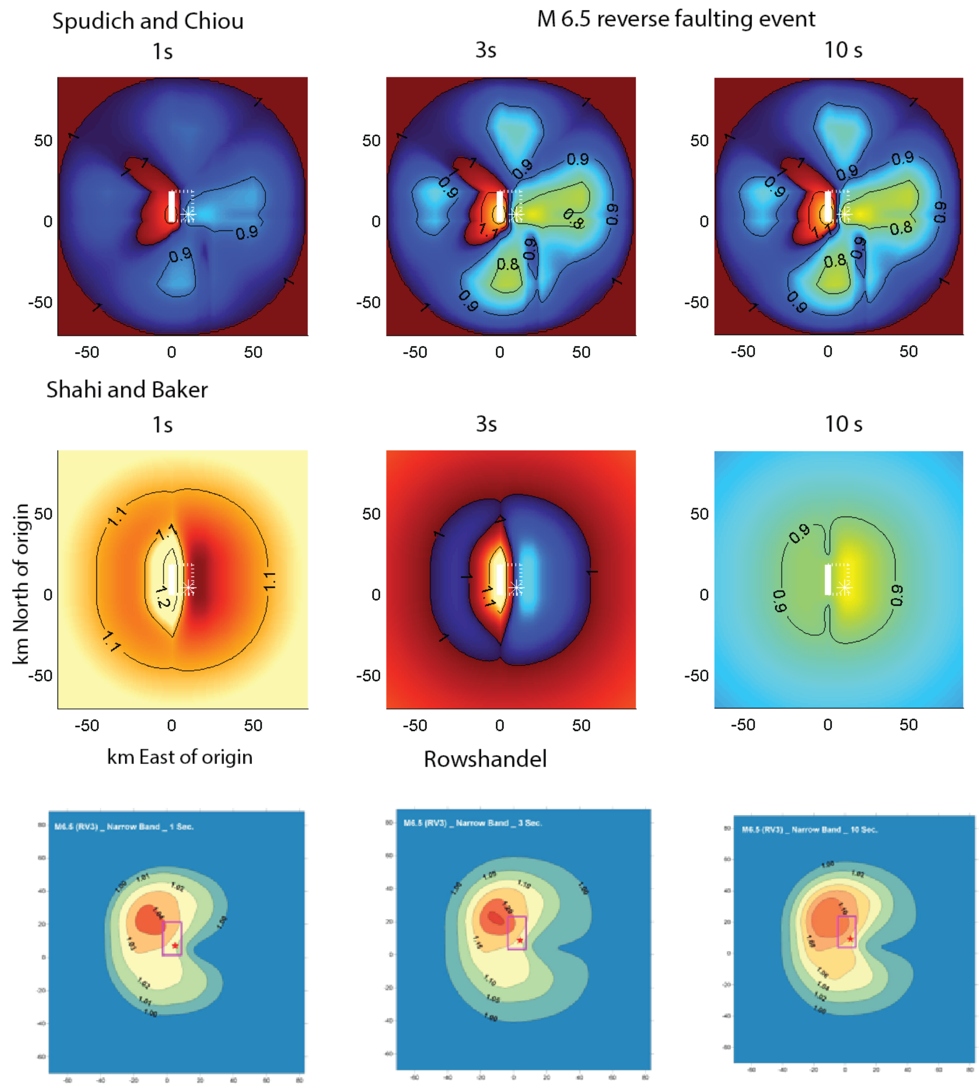

Figure 1.12 Example of three "narrow-band" directivity models, sc3b (top row), sha12 (middle) and rowv4 (bottom row). Predictions are shown for 1, 3, and 10 s for rupture model rv2. Note that the sha12 model is much more sharply peaked in period than the others, in which the peak directivity value varies rather slowly between periods.

1.3.6 Comparison of Directivity Models for Chi-Chi and Denali

Comparisons of the directivity model rowv4, sha12, and sc3b predictions for the 1999 M7.6 Chi-Chi, Taiwan and the 2002 M7.9 Denali, Alaska, earthquakes show some flaws in the directivity models caused by complicated source geometry. (No result was available for bay12.)

In Figure 1.13 for the Chi-Chi quake, the jagged westward protrusions from the Spudich and Chiou IDP model are caused by discontinuous motion of the "closest point" as the site is moved incrementally. See the Spudich and Chiou chapter in this report for more information. All directivity models that depend on the closest point to a site will give spatially discontinuous predictions. Subtle discontinuities can be seen in the sha12 map, perhaps subtle because this directivity pulse model does not predict substantial enhancement more than about 10 km from the fault. The rowv4 predicted amplification is much smoother than those in the other models because the rowv4 prediction is an integral over the entire rupture area. The general locations of directivity maxima agree between rowv4 and sc3b. However, because sha12 predicts ground motion pulses, its maximum in confined near the fault trace.

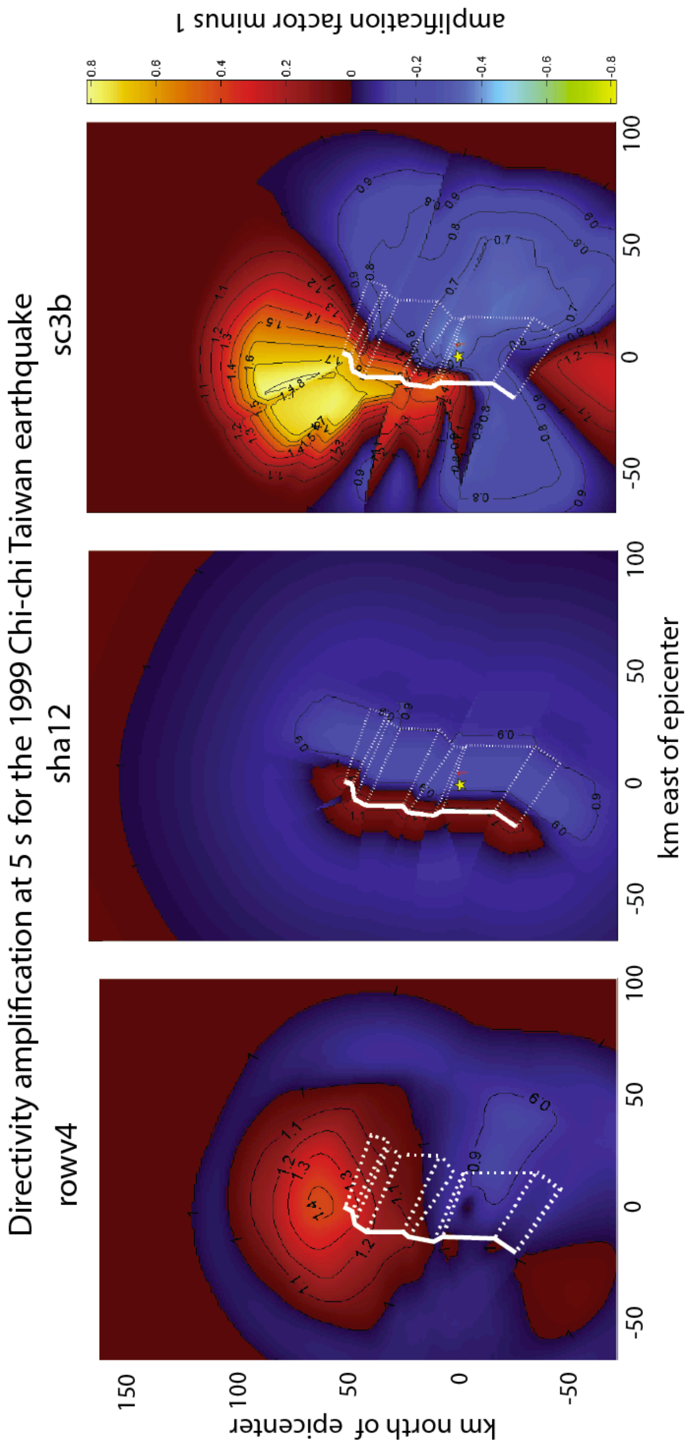

Figure 1.13 **Directivity amplification at 5s for the 1999 Chi-Chi, Taiwan, earthquake. sc3b (right), sha12 (middle) and rowv4 (left). Note the spatial smoothness of rowv4 compared to sc3b. rowv4 and sc3b amplitude footprints agree fairly well, but sha12 has a rather different zone of amplification.**

The three directivity models give similar maps of amplification for the Denali earthquake (Figure 1.14). This raises the question, however, of whether the assumed distance tapers in the directivity models are exerting excessive control. The width of the high-amplitude "tongue" in the sc3b result is certainly controlled by the distance taper from 40 - 70 km (Table 1.3). The factor controlling the width of the directivity tongue is not so clear in rowv4 and sha12. The sha12 map predicts a roughly uniform pulse amplitude within 25 km of the fault at its southeast end. Of course, there are no strong motion data taken 25 km from a M7.9 event, so for this event the sha12 model assumptions control the width of the distribution. (In fact, there are no data in this distance range from the M7.5 Kocaeli, Turkey, earthquake, which is the second largest strike-slip event in the data set.) Ironically, rowv4, which does not bill itself as a pulse model, has the directivity amplification most strongly peaked at the fault. By contrast, bay12, which uses a distance taper extending to half the fault length, would have a much wider directivity tongue, as can be seen in Figure 1.6 for test model ss7.

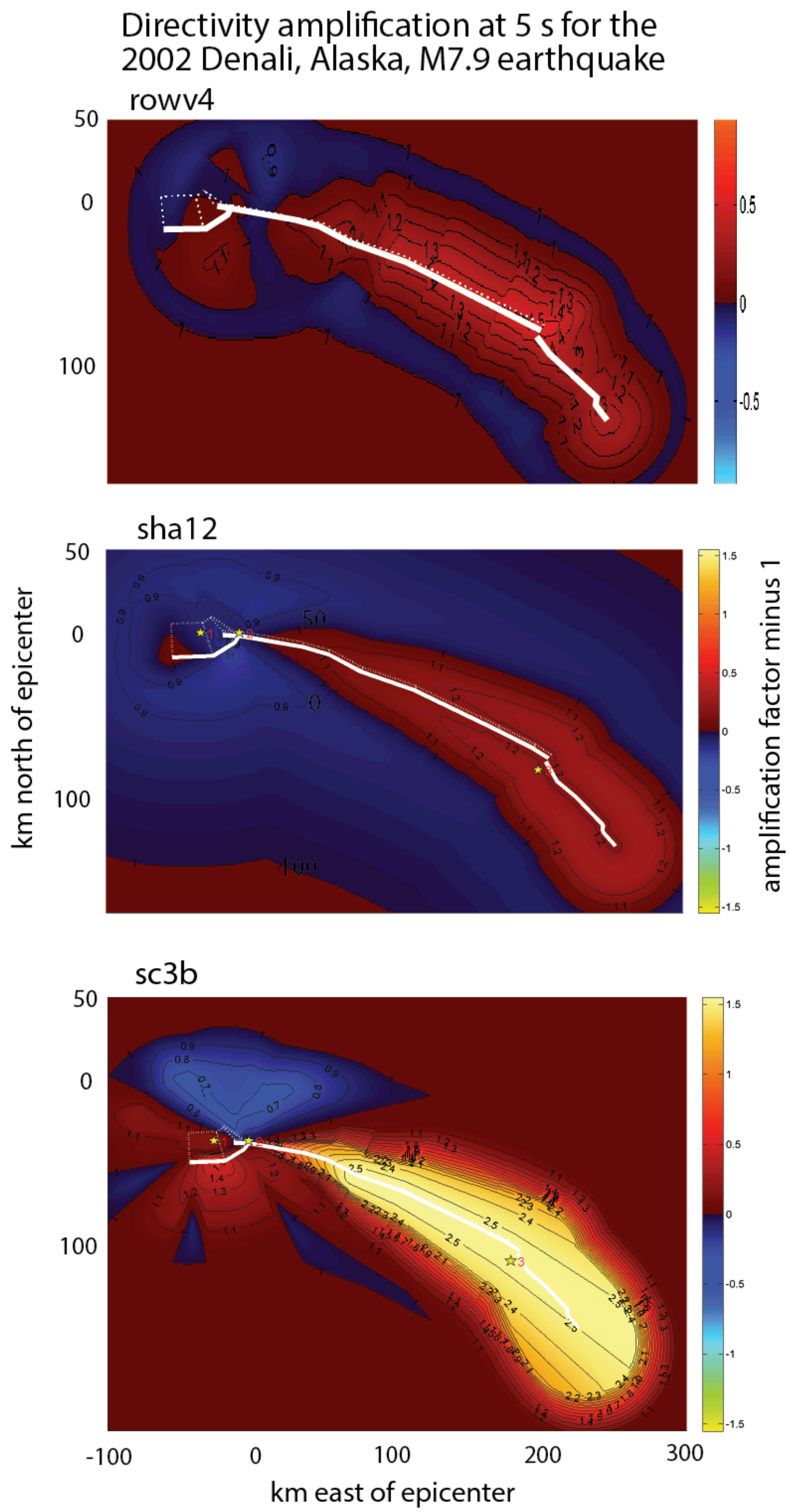

Figure 1.14 **Directivity amplification at 5s for the 2002 Denali, Alaska, earthquake. sc3b (bottom), sha12 (middle) and rowv4 (top). Note widths of high amplification "tongues."**

1.4 SUMMARY AND CONCLUSIONS

Four teams of directivity modelers derived improved directivity models by making conceptual advances as well as through empirical study of the expanded NGA-West2 data set. Among the conceptual advances was the adoption by some modelers of "narrow-band" directivity models. In addition, all models chose to eschew normalized fault dimensions, because normalized fault dimensions caused nonphysical scaling of directivity for large magnitude events.

Comparisons show that the vertical strike-slip rupture geometries are modeled similarly by each directivity model, and there are many areas of agreement, although the predicted amplitudes can be quite different, an observation that is tentative until the directivity models are implemented *ab initio* in a GMPE. However, for reverse faults the predicted motions differ from each other so much that it would be unwise to use just one directivity model to simulate motions at a specific site.

After ten years of directivity model development associated with NGA-West and NGA-West2, these directivity models are certainly better than no directivity model, but they are still rather unsatisfying. Directivity can be clearly seen in PGA and PGV of earthquakes in the M 3 - M 5 range [Boatwright 2007; Seekins and Boatwright 2010], but none of these models has a functional form that transitions smoothly from large to small magnitude and describes the small magnitude or short period directivity. Of course, this may be of little engineering concern, but it indicates an unsatisfying omission of some important physical principle. Possibly the Shahi and Baker model is closest to being able to address this issue. It is troubling that the width of high directivity zones is controlled by rather poorly determined distance tapers. This taper should be a function of period, but only the Rowshandel model addresses this issue. The comparison of the reverse-faulting predictions gives pause because of the previously mentioned sensitivity of the results to the assumptions of the model. For example, the use of a point source radiation pattern in the Spudich and Chiou model has clear effects that would probably not result from an extended finite source. It would be an advance to be able to approximate a finite-source radiation pattern, on which Chiou and Spudich [2013], following Watson-Lamprey [unpublished notes 2012], have taken some steps, rather than having to calculate it directly by integrating over the fault surface, as in Rowshandel [2013].

It is also troubling that the big ground motion records that excited interest in directivity, like the Lucerne recording of the Landers earthquake, occur at short rupture distances and within the ends of the causative fault. Numerical simulations of ground motions on long strike-slip faults, as noted in Spudich and Chiou [2008], also show that the maximum motions occur within the ends of the faults, but our directivity models for strike-slip events tend to predict the biggest motions in a broad zone off the "shotgun" end of the fault, probably because they developed as corrections to GMPEs that already modeled much of the near-fault directivity with some other functions of M and R. It is possible that when directivity models are included *ab initio* in the development of a GMPE, the developers will be shocked by the amount that their M- and R-dependent terms change. The Chi-Chi, Taiwan, main shock and aftershocks seem to ooze directivity, but very recent unpublished work [Brian Chiou, personal communication] suggests that associated with the seismic stations there are site amplifications that might mimic directivity, meaning that the preliminary directivity models presented here are biased high. San Andreas system earthquakes often have classic directivity pulses (e.g., 1979 Coyote Lake, 1984 Morgan Hill), but finding directivity in these earthquakes is difficult. Finding directivity in Japanese crustal earthquakes is even more of a challenge. It might be that the physical wear process associated with cumulative offset of San Andreas system events may be greater than the same for Japanese earthquakes, and such wear has created low velocity zones or other physical changes that enhance ground motions (e.g., Spudich and Olsen [2001]).

2 Bayless and Somerville Model

Jeffrey R. Bayless and Paul Somerville

The following report summarizes the Bayless and Somerville 2013 directivity model, designed to modify ground-motion model predictions to account for directivity amplification. This model is an update to the 1997 Somerville model [Somerville et al. 1997].

2.1 MODEL APPLICATION

The median spectral acceleration from an empirical attenuation relation without directivity effect (Sa) can be modified to obtain the spectral acceleration with directivity effects (Sa_{dir}) by the following Equation (2.1):

$$\ln(Sa_{dir}) = \ln(Sa) + f_D \tag{2.1}$$

where f_D is the directivity effect. The directivity effect is quantified as the product of the period and fault-type-dependent constant coefficient, the distance, magnitude, and azimuth tapers, and the geometric directivity predictor (f_{geom}), which correlates the directivity effects with the spatial variation of near-fault ground motions. f_{geom} is a function of the fraction of the fault rupture surface that lies between the hypocenter and the site (parameter X or Y) multiplied by the length or width of the fault (parameter L or W), and the angle between the direction of rupture propagation and the direction of waves travelling from the fault to the site (parameter θ or R_x/W). The directivity effect is expressed as in Equation (2.2):

$$f_D = f_D(s, \theta, d, R_x, M_w, R_{rup}, L, W, Az, T) = (C_0 + C_1 * f_{geom}) * T_{CD} * T_{M_w} * T_{Az} \tag{2.2}$$

In this model, faults having rakes in the range $0° < |rake| < 30°$ or $150° < |rake| < 180°$ are considered strike-slip, and rakes in the range $60° < |rake| < 120°$ are considered dip-slip. Rakes outside those limits (and ultimately, any arbitrary rake angle) can be handled using the oblique slip recipe given in Section 2.1.8.2.

2.2 STRIKE-SLIP: [$0° < |rake| < 30°$ OR $150° < |rake| < 180°$]

Geometric Directivity Predictor:

$$f_{geom}(s, \theta) = \log_e(s) * (0.5\cos(2\theta) + 0.5) \tag{2.3}$$

Distance Taper:

$$T_{CD}(R_{rup}, L) = 1 \qquad for\ \frac{R_{rup}}{L} < 0.5$$

$$= 1 - (R_{rup}/L - 0.5)\ /0.5 \qquad for\ 0.5 < R_{rup}/\ L < 1 \qquad (2.4)$$

$$= 0 \qquad for\ R_{rup}/L > 1.0$$

Magnitude Taper:

$$\begin{aligned} T_{M_w}(M_w) &= 1 && for\ M_w > 6.5 \\ &= 0 && for\ M_w < 5.0 \qquad (2.5) \\ &= 1 - (6.5 - M_w)\ /1.5 && for\ 5.0 < M_w < 6.5 \end{aligned}$$

Azimuth Taper:

$$T_{Az}(Az) = 1 \qquad (2.6)$$

2.3 DIP-SLIP: [$60° < |\boldsymbol{rake}| < \mathbf{120}°$]

Geometric Directivity Predictor:

$$f_{geom}(d, R_X) = \log_e(d) * \cos\ (R_x/W) \qquad (2.7)$$

Distance Taper:

$$\begin{aligned} T_{CD}(R_{rup}, W) &= 1 && for\ R_{rup}/W < 1.5 \\ &= 1 - (R_{rup}/W - 1.5)/0.5 && for\ 1.5 < R_{rup}/\ W < 2.0 \qquad (2.8) \\ &= 0 && for\ R_{rup}/W\ > 2.0 \end{aligned}$$

Magnitude Taper:

$$\begin{aligned} T_{M_w}(M_w) &= 1 && for\ M_w > 6.5 \\ &= 1 - (6.5 - M_w)\ /1.5 && for\ 5.0 < M_w < 6.5 \qquad (2.9) \\ &= 0 && for\ M_w < 5.0 \end{aligned}$$

Azimuth Taper:

$$T_{Az}(Az) = \sin(|Az|)^2 \qquad (2.10)$$

where:

$C_{s0}, C_{s1}, C_{d0}, C_{d1} = Period\ dependent\ coefficients\ (C_s\ for\ strike\ slip, C_d\ for\ dip\ slip)$

$s = the\ length\ of striking\ fault\ rupturing\ towards\ site$; $\max[(X * L), \exp(1)]$

$\theta = SSGA97\ parameter\ (0° \leq \theta_1 \leq 90°)$

$d =\ the\ length\ of dipping\ fault\ rupturing\ towards\ site$; $\max[(Y * W), \exp\ (0)]$

$R_x = Horizontal\ distance\ (km) from\ top\ edge\ of\ rupture.$

$W = fault\ width\ (km), \qquad note\colon \left(-\pi/2 \le \frac{R_x}{W} \le 2\pi/3\right)$

$M_w = moment\ magnitude$
$R_{rup} = closest\ distance\ to\ fault\ rupture\ plane\ (km)$
$L = fault\ length\ (km)$

$Az = NGA\ source\ to\ site\ azimuth$

$T = period\ (sec)$

2.4 GEOMETRIC DIRECTIVITY PREDICTOR

The new functional form of the geometric directivity predictor (f_{geom}) increases with increasing length of the fault rupturing towards a site, instead of utilizing a proportion of the fault. By removing the normalization to fault length, there is potential for larger directivity effects along larger faults. Figure 2.1 shows the behavior of the directivity predictor for a strike-slip fault and a dip slip fault as a function of the components of f_{geom}.

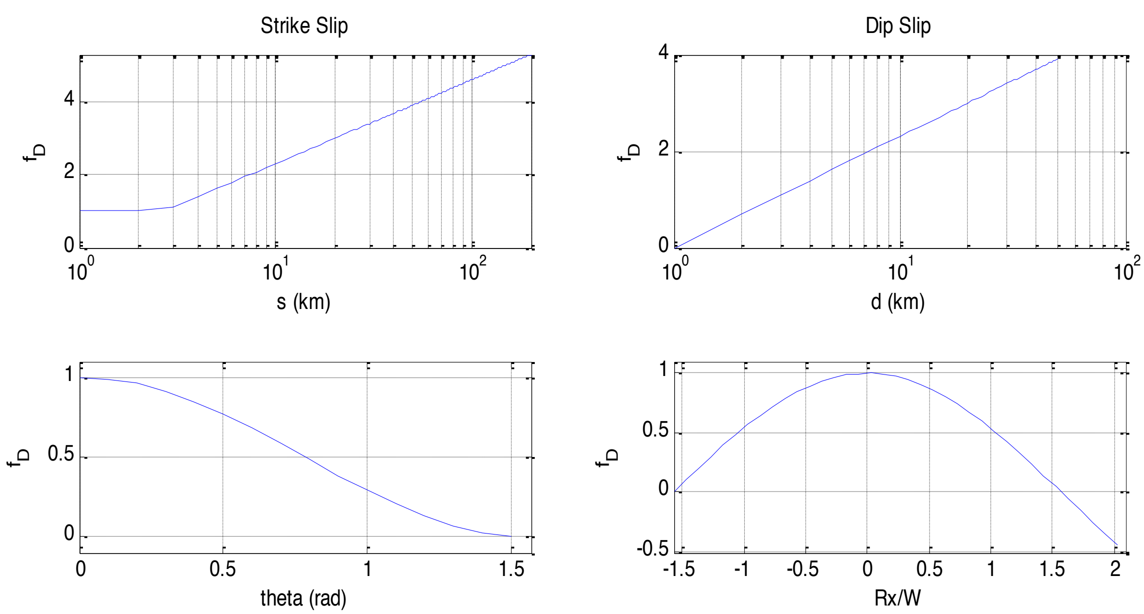

Figure 2.1 Behavior of Bayless and Somerville directivity as a function of site location parameters.

2.5 TAPERS

Directivity effects are usually significant for moderate to large events and within a certain rupture distance. Tapers applied to the directivity predictor scale the directivity effect (f_D), and reduce it to zero outside these predefined ranges. With this formulation, the directivity correction can be applied to any record set.

2.5.1 Distance

The distance taper function is dependent on R_{rup}/L for strike-slip faults and R_{rup}/W for dip-slip faults. There is no reduction inside of 0.5 fault length or 1.5 fault widths, and f_D is reduced to zero at $R_{rup}/L = 1$ and $R_{rup}/W = 2$ for strike-slip and dip-slip faults, respectively. The transition is linear between these extremes, as shown in Figure 2.2.

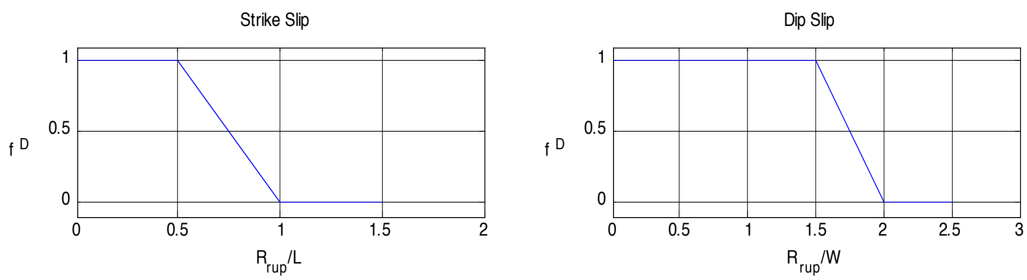

Figure 2.2 Illustration of distance tapers in Bayless and Somerville model.

While the Bayless and Somerville model is applicable for all distance ranges (tapers are dependent on fault length or width, not an absolute distance), the authors recommend incorporating the directivity effect for ground motions where $R_{rup} \leq 200$ km; the distance range from which recorded motions were used to develop the model.

2.5.2 Magnitude

The magnitude taper function is identical for strike-slip and dip-slip faults. Below $M_w = 5.0$ the directivity effect is reduced to zero, and above $M_w = 6.5$ there is no reduction (Figure 2.3).

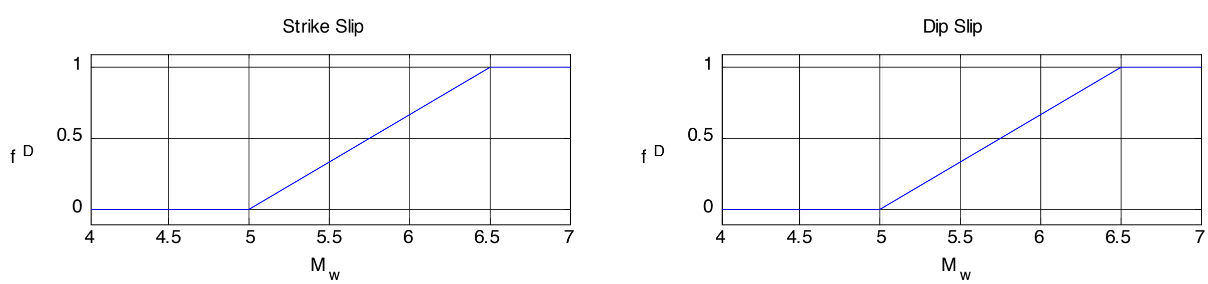

Figure 2.3 Magnitude tapers in Bayless and Somerville model for strike-slip and dip-slip ruptures.

2.5.3 Azimuth

The azimuth taper is unity for strike-slip faults. For dipping faults, this taper replaces the "excluded zone" from SSGA97 by reducing the directivity effect for small and large azimuth angles; or in other words reducing the effect at locations off the ends of the fault along strike (Figure 2.4).

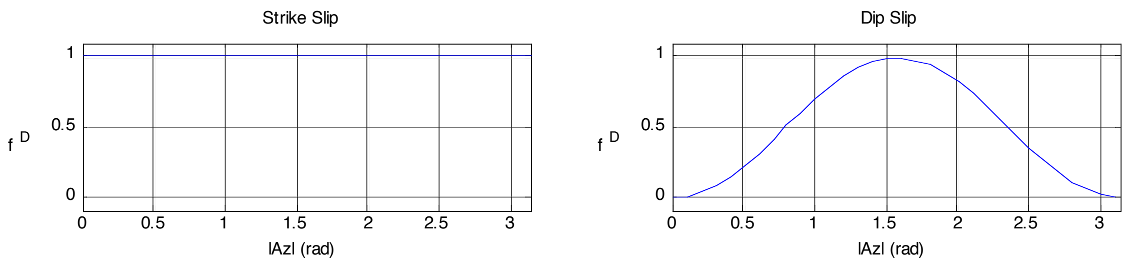

Figure 2.4 Azimuth tapers for Bayless and Somerville model.

2.6 COEFFICIENTS

Coefficients are period dependent, fault type dependent, and horizontal component dependent. Those shown in Table 2.1 and Table 2.2 are the smoothed average coefficients derived from fitting residuals from the four 2008 NGA GMPEs:

Table 2.1 Coefficients of the Bayless and Somerville model for strike-slip ruptures.

Period (sec)	Strike-Slip					
	RotD50		FN		FP	
	C0	C1	C0	C1	C0	C1
0.5	0.000	0.000	0.000	0.000	0.000	0.000
0.75	0.000	0.000	-0.080	0.055	0.000	0.000
1	-0.120	0.075	-0.225	0.110	0.015	0.000
1.5	-0.175	0.090	-0.300	0.135	0.030	-0.025
2	-0.210	0.095	-0.325	0.160	0.050	-0.040
3	-0.235	0.099	-0.365	0.185	0.070	-0.045
4	-0.255	0.103	-0.390	0.205	0.080	-0.050
5	-0.275	0.108	-0.410	0.215	0.090	-0.060
7.5	-0.290	0.112	-0.420	0.220	0.100	-0.070
10	-0.300	0.115	-0.425	0.225	0.108	-0.071

Table 2.2 Coefficients of the Bayless and Somerville model for dip-slip ruptures.

Period (sec)	Dip-Slip					
	RotD50		FN		FP	
	C0	C1	C0	C1	C0	C1
0.5	0.000	0.000	0.000	0.000	0.000	0.000
0.75	0.000	0.000	0.000	0.000	0.000	0.000
1	0.000	0.000	0.000	0.000	0.000	0.000
1.5	0.000	0.000	0.000	0.000	0.000	0.000
2	0.000	0.034	0.000	0.056	0.000	0.030
3	-0.033	0.093	-0.034	0.120	-0.034	0.080
4	-0.089	0.128	-0.092	0.142	-0.110	0.120
5	-0.133	0.150	-0.115	0.160	-0.175	0.150
7.5	-0.160	0.165	-0.122	0.165	-0.195	0.170
10	-0.176	0.179	-0.125	0.170	-0.200	0.175

2.7 EXTENSION TO GEOMETRICALLY COMPLICATED FAULTS

2.7.1 Approach to Multi-Segment and Multi-Strand Faults

For each strand:

- The hypocenter of the segment is defined in a past event and specified in a future scenario event.
- Define the pseudo-hypocenter for rupture of successive segments as the point on the side edge of the fault segment that is closest to the side edge of the previous segment, and that lies half way between the top and bottom of the fault. We assume that the fault is segmented along strike, not updip. All geometric parameters are computed relative to the pseudo-hypocenter.
- Calculate the directivity adjustment term f_D for each segment.

Calculate the weighted average of the directivity adjustment terms f_D for each segment using the seismic moments of the individual segments as the weights. The direction of rupture propagation is assumed to be the same on sub parallel strands, and hypocenters are set accordingly. Calculate the weighted average of the directivity adjustment terms f_D for each strand using the seismic moments of the individual strands as the weights. An example of a multiple-segment dip-slip fault is shown in Figure 2.5.

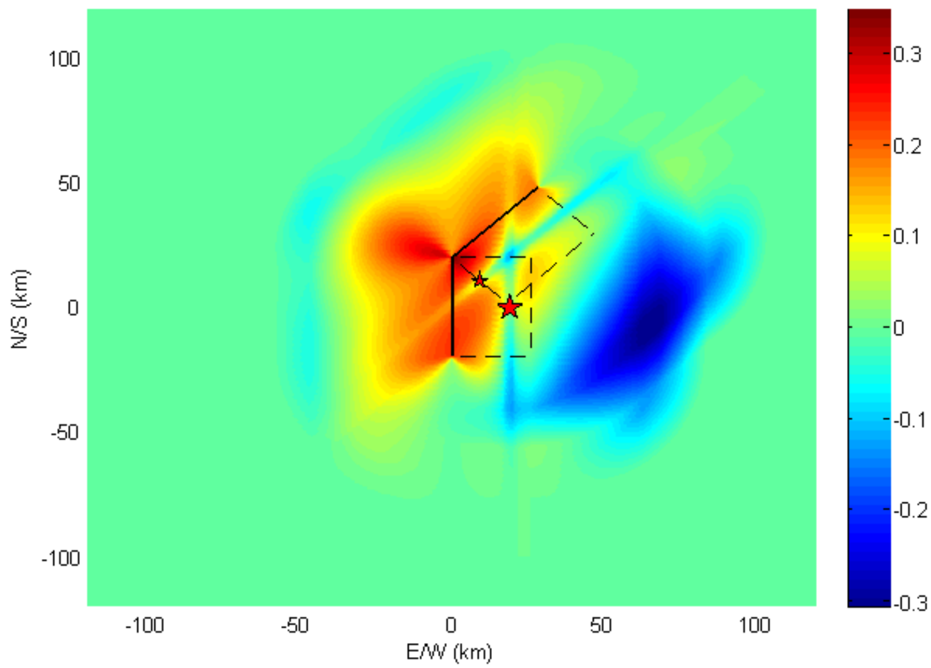

Figure 2.5 **Illustration of the calculation of Bayless and Somerville directivity for a multi-segment dip-slip fault, FN component, T=5s. Large red star is the real hypocenter; smaller red star is the pseudo-hypocenter. Each segment is assumed to have equal seismic moment in this example.**

2.7.2 Optional Approach for Oblique Faults

For oblique faults, calculate both the purely strike and dip-slip directivity corrections for the fault, and then take a weighted average based on rake angle:

1. Normalize rake to first-quadrant angle ($0 \leq$ Q1Rake ≤ 90)
2. Compute DipWeight = Q1Rake/90
3. Compute StrikeWeight = 1 – DipWeight
4. Compute f_D = StrikeWeight*(f_{D_strike}) + DipWeight*(f_{D_dip})

This combination of pure strike-slip and pure-dip slip directivity patterns for oblique faults causes ruptures with rake in quadrants 1-4 to all have the same directivity pattern as their normalized first-quadrant rake angle (i.e. a rupture with rake of 120 degrees has the same pattern as a rake of 60 degrees for identical rupture geometry.) This simplification is a result of incorporating bilateral rupture into all fault scenarios, with the directivity pattern being controlled by the length (or width) of the fault between the hypocenter and the site. This approach may be applied to faults with any arbitrary rake, which will combine the radiation patterns of the two mechanism distinctions.

An example of this approach applied on a hypothetical fault with rake=120 deg is shown in Figure 2.6.

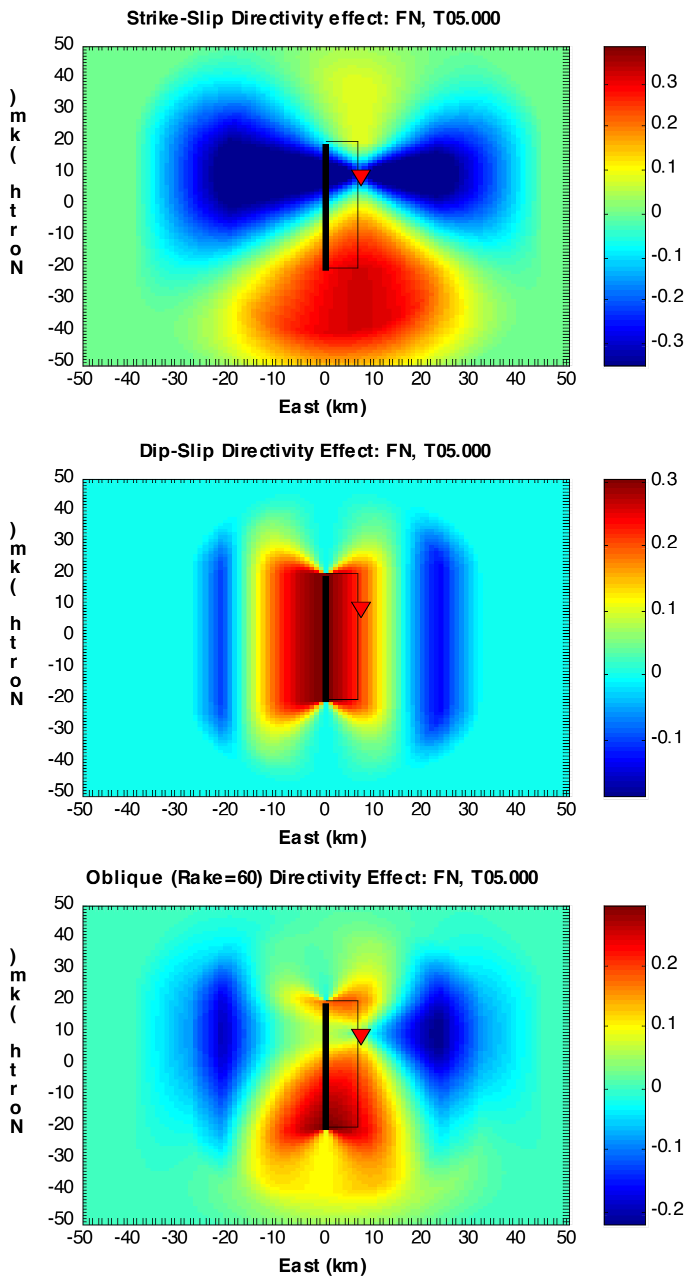

Figure 2.6 Illustration of the calculation of Bayless and Somerville directivity for a fault with oblique slip. Top pane: purely strike-slip directivity effect. Middle pane: purely dip-slip directivity effect. Bottom pane: combined (oblique) effect.

2.8 TEST CASE/SCENARIO RESULTS

The following section presents maps of the directivity effect, f_D, for a series of hypothetical faults. Therefor to calculate the increase in predicted ground motions for a GMPE without directivity (Sa_{nodir}) one would apply the following equation:

$$Sa_{dir} = e^{f_D} * Sa_{nodir} \tag{2.11}$$

In this section the maps are shown at period T=5.0 seconds, the RotD50 component of ground motion, and with the oblique fault approach from Section 2.1.8.2 applied. Note that the directivity effects are calculated at very large distances in the larger fault scenarios.

2.8.1 Strike-Slip Test Cases

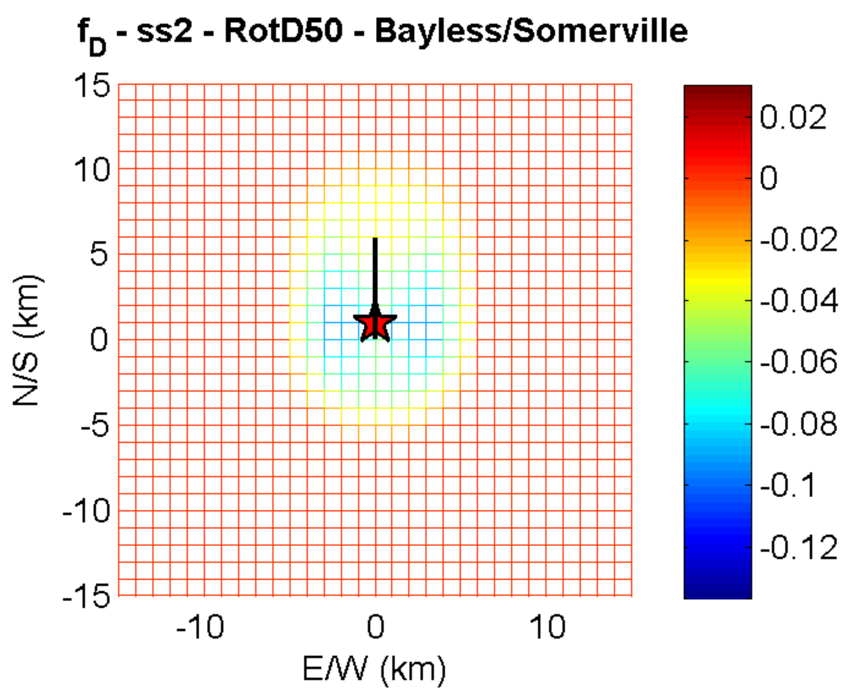

Figure 2.7 Distribution of directivity effect for test case ss2: A strike-slip fault with L=25 km, Rake=180°, Dip=90°, Mw=6.5. Hypocenter location represented by red star. Note: Apparent asymmetry of the directivity effect is a product of the large grid spacing for this test case, and is not actually present.

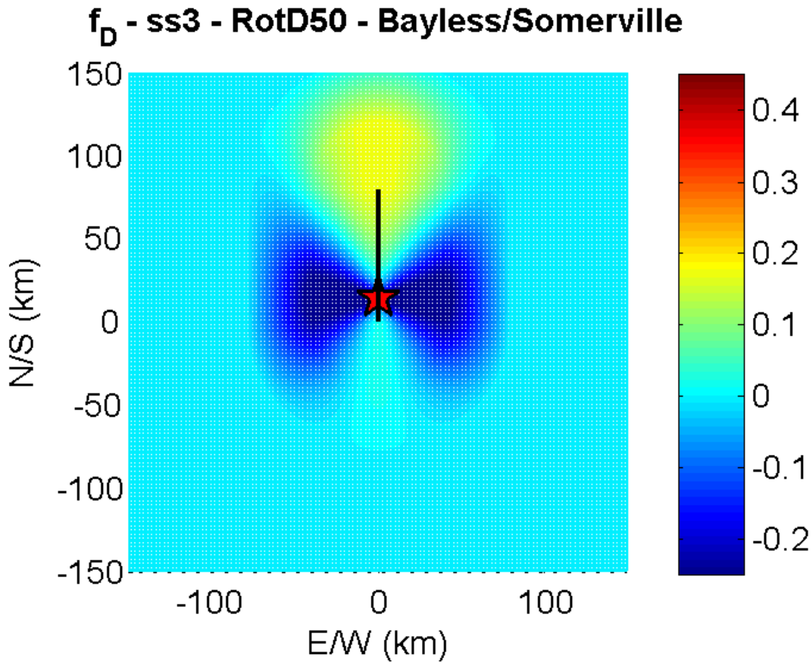

Figure 2.8 **Distribution of directivity effect for test case ss3: A strike-slip fault with L=80 km, Rake=180°, Dip=90°, Mw=7.2. Hypocenter location represented by red star.**

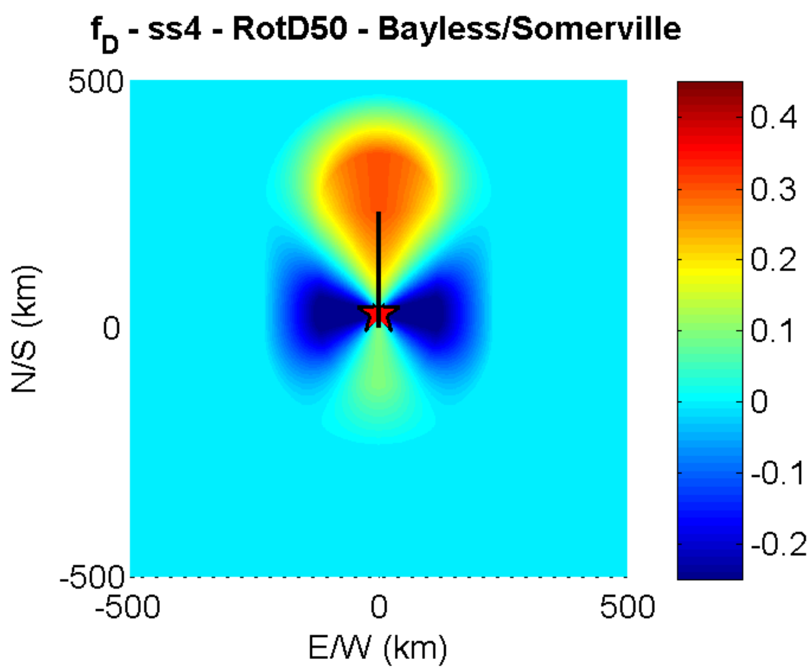

Figure 2.9 **Distribution of directivity effect for test case ss4: A strike-slip fault with L=235 km, Rake=180°, Dip=90°, Mw=7.8. Hypocenter location represented by red star.**

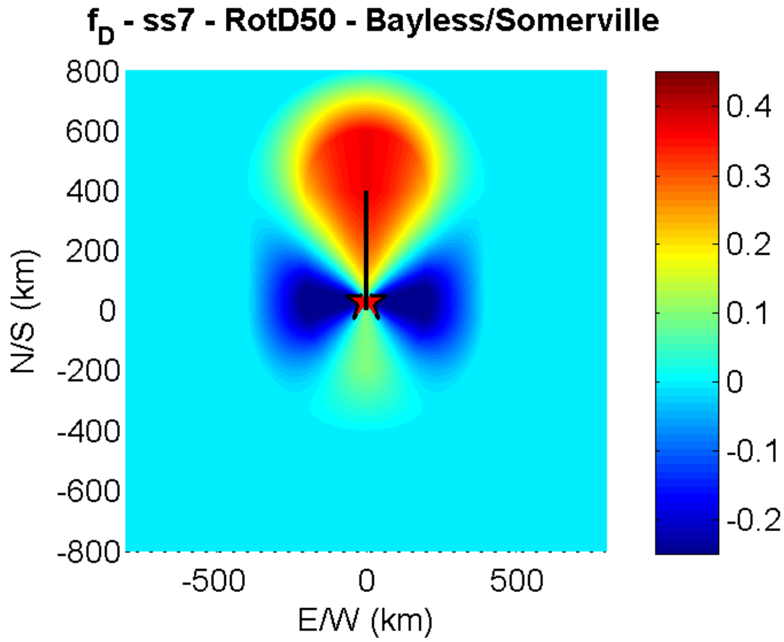

Figure 2.10 **Distribution of directivity effect for test case ss7: A strike-slip fault with L=400 km, Rake=180°, Dip=90°, Mw=8.1. Hypocenter location represented by red star.**

2.8.2 Dip-Slip Test Cases

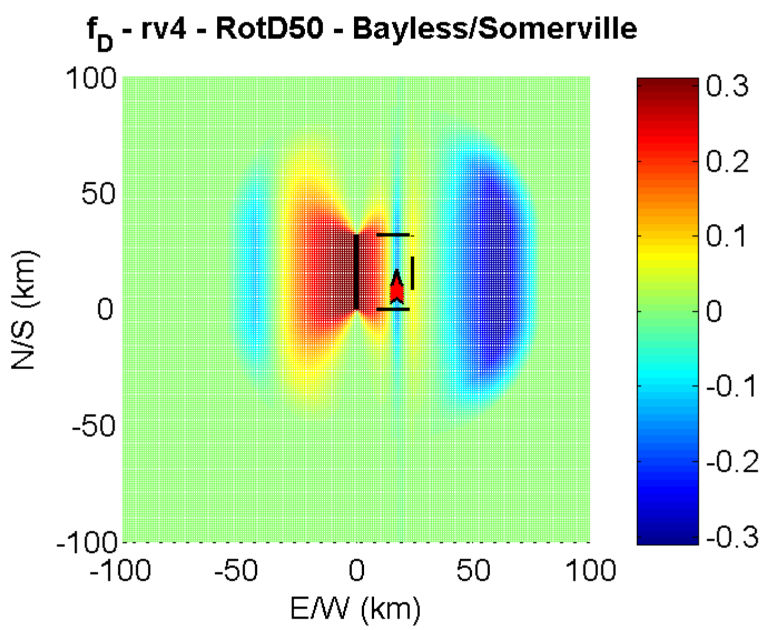

Figure 2.11 **Distribution of directivity effect for test case rv4: A reverse fault with L=32 km, W=28 km, Rake=90°, Dip=30°, Mw=7.0. Hypocenter location represented by red star, and solid black line represents surface edge of fault.**

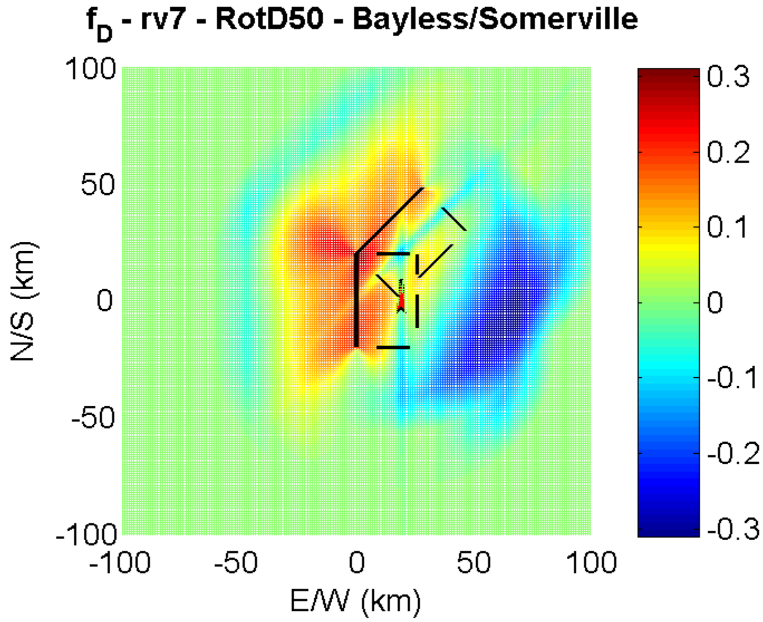

Figure 2.12 **Distribution of directivity effect for test case rv7: A two-segment reverse fault with W=30 km, Rake=90°, Dip=30°, Mw=7.5. First hypocenter location represented by red star, and solid black line represents surface edge of faults.**

2.8.3 Oblique Test Cases

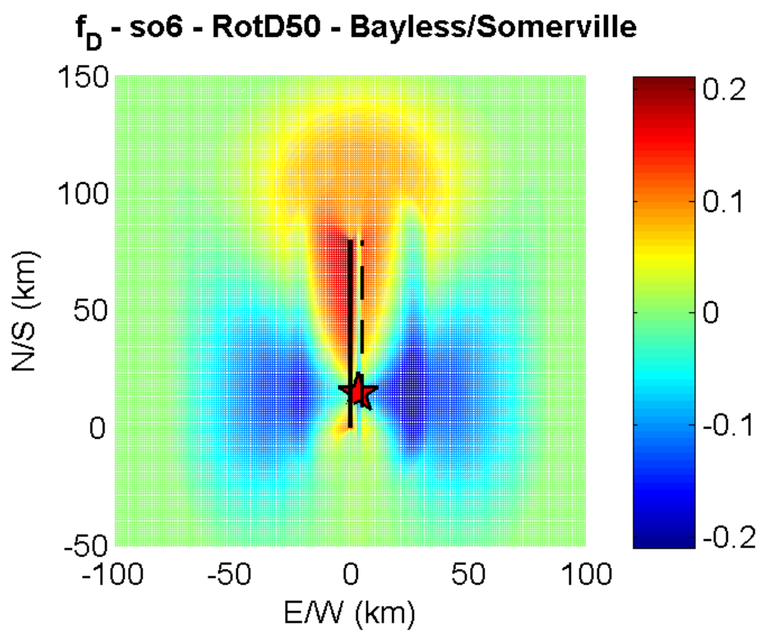

Figure 2.13 **Distribution of directivity effect for test case so6: A strike-slip oblique fault with L=80 km, W=15 km, Rake=135°, Dip=70°, Mw=7.2. Hypocenter location represented by red star, and solid black line represents surface edge of fault.**

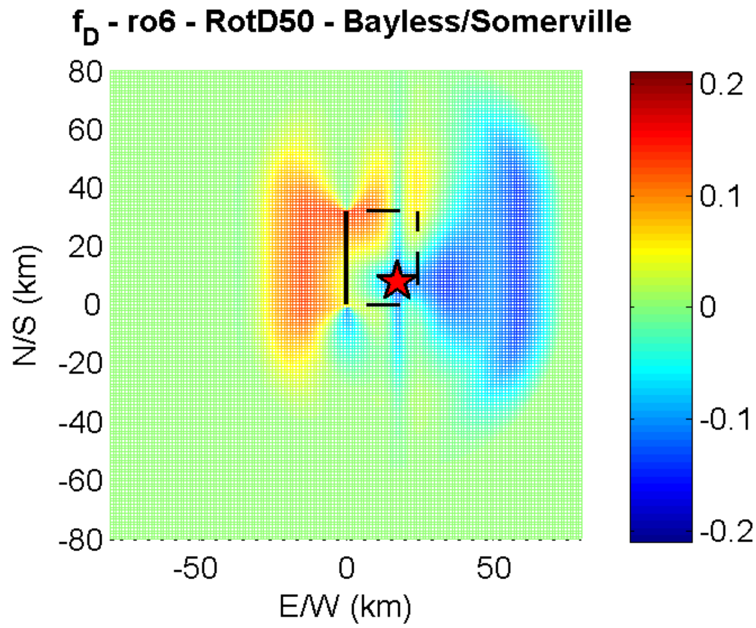

Figure 2.14 Distribution of directivity effect for test case ro6: A reverse oblique fault with L=32 km, W=28 km, Rake=135°, Dip=30°, Mw=7.0. Hypocenter location represented by red star, and solid black line represents surface edge of fault.

2.9 RESIDUALS

The following section presents the impacts of including the directivity terms in the 2008 NGA GMPEs [Abrahamson and Silva 2008, Boore and Atkinson 2008, Campbell and Bozorgnia 2008, Chiou and Youngs 2008] on reducing the prediction uncertainty. The impact of the directivity correction is evaluated on the change in intra-event sigma of each 2008 GMPE developer's residuals. These relations are summarized in Abrahamson et al. [2008].

2.9.1 Abrahamson and Silva 2008 (AS08)

Table 2.3 Sigma reductions for AS08 GMPE, Rotd50 component.

GMPE: AS08, Rotd50 Component			
T (sec)	Original σ (ln)	Directivity Corrected σ (ln)	Difference (ln)
0.1	0.551	0.551	0.000
0.15	0.539	0.539	0.000
0.2	0.543	0.543	0.000
0.25	0.534	0.534	0.000
0.3	0.550	0.550	0.000
0.4	0.569	0.569	0.000
0.5	0.583	0.583	0.000
0.75	0.608	0.608	0.000
1	0.617	0.616	0.001
1.5	0.600	0.599	0.001
2	0.618	0.615	0.003
3	0.622	0.613	0.009
4	0.618	0.605	0.012
5	0.628	0.611	0.017
7.5	0.627	0.614	0.013
10	0.635	0.621	0.014

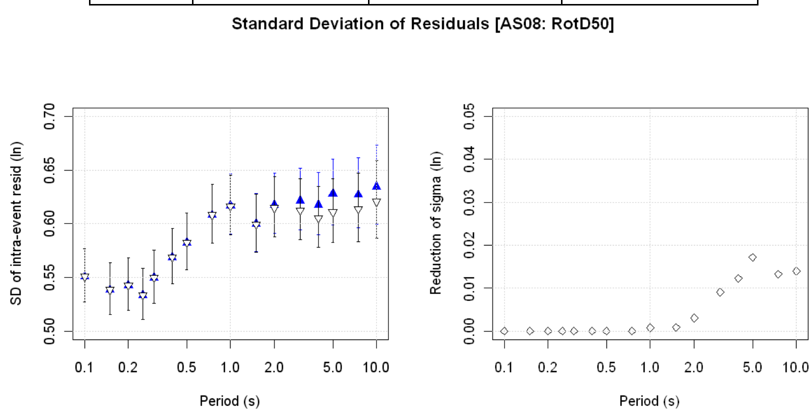

Figure 2.15 Plot of AS08 sigma reductions after application of the directivity effect. Error bars represent 95% confidence intervals.

2.9.2 Boore and Atkinson 2008 (BA08)

Table 2.4 Sigma reductions for BA08 GMPE, Rotd50 component.

GMPE: BA08, Rotd50 Component			
T (sec)	Original σ (ln)	Directivity Corrected σ (ln)	Difference (ln)
0.1	0.573	0.573	0.000
0.15	0.558	0.558	0.000
0.2	0.565	0.565	0.000
0.25	0.562	0.562	0.000
0.3	0.581	0.581	0.000
0.4	0.597	0.597	0.000
0.5	0.615	0.615	0.000
0.75	0.652	0.652	0.000
1	0.666	0.668	-0.001
1.5	0.646	0.646	0.000
2	0.662	0.658	0.004
3	0.664	0.654	0.010
4	0.657	0.644	0.013
5	0.662	0.643	0.019
7.5	0.651	0.633	0.018
10	0.660	0.636	0.023

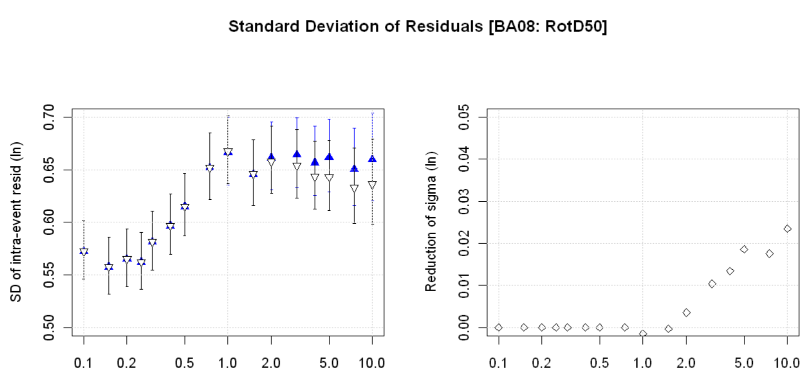

Figure 2.16 Plot of BA08 sigma reductions after application of the directivity effect.

2.9.3 Campbell and Bozorgnia 2008 (CB08)

Table 2.5 Sigma reductions for CB08 GMPE, Rotd50 component.

GMPE: CB08, Rotd50 Component			
T (sec)	Original σ (ln)	Directivity Corrected σ (ln)	Difference (ln)
0.1	0.512	0.512	0.000
0.15	0.508	0.508	0.000
0.2	0.516	0.516	0.000
0.25	0.506	0.506	0.000
0.3	0.524	0.524	0.000
0.4	0.548	0.548	0.000
0.5	0.559	0.559	0.000
0.75	0.588	0.588	0.000
1	0.593	0.592	0.001
1.5	0.560	0.560	0.000
2	0.563	0.563	0.000
3	0.555	0.551	0.004
4	0.555	0.548	0.008
5	0.559	0.546	0.014
7.5	0.557	0.540	0.017
10	0.557	0.540	0.017

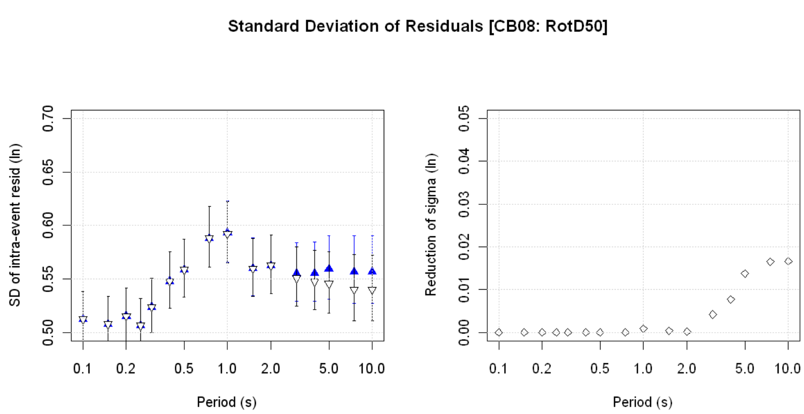

Figure 2.17 Plot of CB08 sigma reductions after application of the directivity effect.

2.9.4 Chiou and Youngs 2008 (CY08)

Table 2.6 Sigma reductions for CY08 GMPE, Rotd50 component.

GMPE: CY08, Rotd50 Component			
T (sec)	Original σ (ln)	Directivity Corrected σ (ln)	Difference (ln)
0.1	0.537	0.537	0.000
0.15	0.526	0.526	0.000
0.2	0.527	0.527	0.000
0.25	0.512	0.512	0.000
0.3	0.525	0.525	0.000
0.4	0.550	0.550	0.000
0.5	0.563	0.563	0.000
0.75	0.594	0.594	0.000
1	0.592	0.593	-0.001
1.5	0.567	0.568	-0.001
2	0.584	0.584	0.000
3	0.588	0.583	0.004
4	0.584	0.577	0.007
5	0.603	0.590	0.013
7.5	0.603	0.591	0.011
10	0.574	0.557	0.017

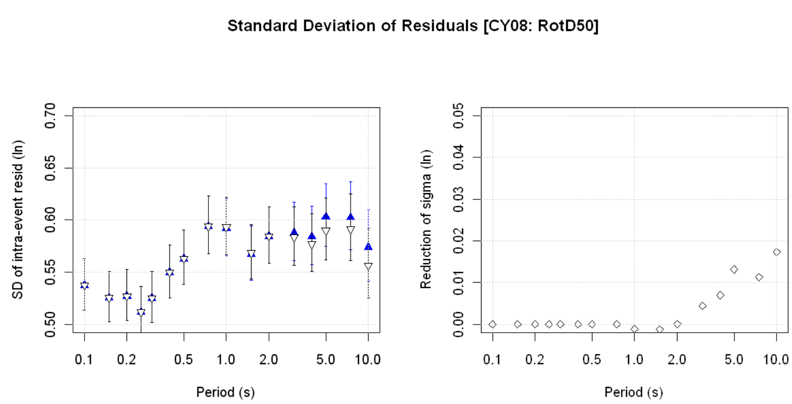

Figure 2.18 Plot of CY08 sigma reductions after application of the directivity effect.

3 Rowshandel's NGA-West2 Directivity Model

Badie Rowshandel

3.1 BACKGROUND AND METHODOLOGY

The directivity model presented in this chapter is developed based on the concept that "in order to attain maximum directivity effect at a site the direction of rupture and the direction of slip should both be toward the site." In reality during an earthquake both the direction of rupture and the direction of slip vary from location to location on the surface of a fault. This is due to the more realistic heterogeneous ruptures of faults during earthquakes. For the purpose of the present study rupture on faults is assumed to be homogeneous. However, the model presented here, after minor revisions, can be easily used to study source rupture effects due to heterogeneous rupture. But this is beyond the scope of the present work, and hence is left for future work.

3.2 FORMULATION

The directivity parameter ξ in its final form combines five pieces of information as expressed in the following relation:

$$\xi = (\xi' - \xi_c')*LD*DT*WP \tag{3.1}$$

Where:

ξ' is the traditional wide-band directivity parameter before applying any corrections,

LD is the rupture length de-normalization factor,

ξ_c' is the directivity-centering parameter,

DT is the distance-taper, and

WP is the narrow-band multiplier.

In the following sections expressions for the above parameters are obtained.

3.2.1 ξ' for Single-Segment Faults

The methodology for calculating ξ' has been presented in various documentations on previous version of the model (i.e., Rowshandel [2006] and [2010]). In the present study, the previous version has been improved so that directivity parameter ξ' can be computed based on the direction of rupture or the direction of slip, or the combination (Figure 3.1).

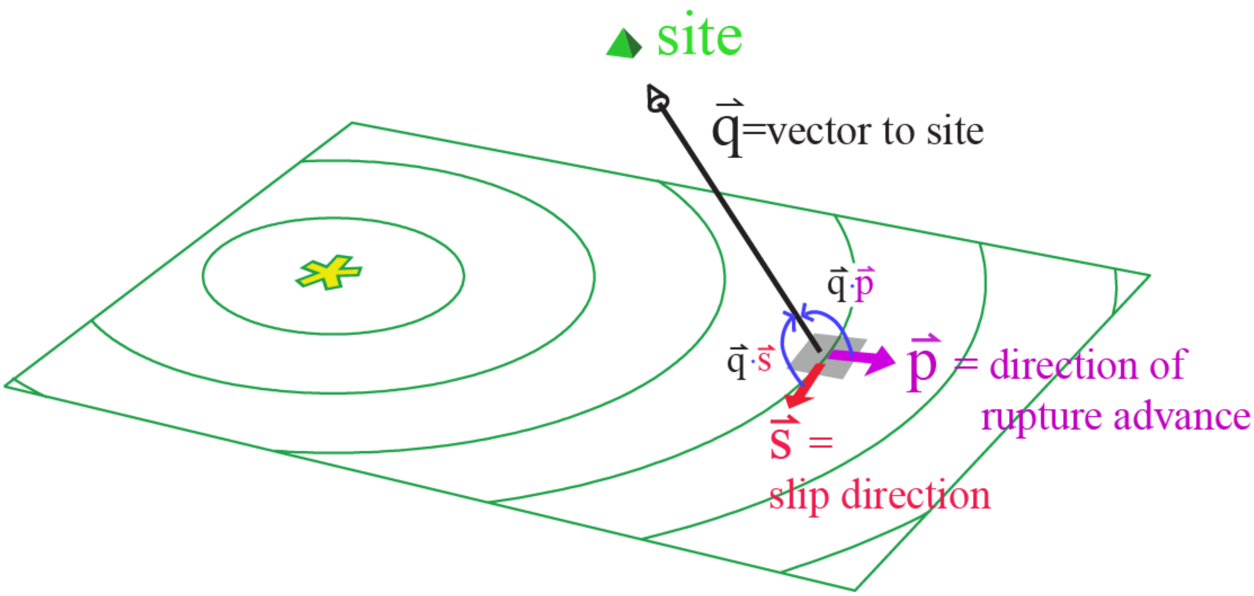

Figure 3.1 Graphical representation of the model.

The procedure to compute *ξ'* is as follows:

- Specify the rectangular-shaped planar fault by the coordinates of its beginning point A (X_A=Longitude, Y_A=Latitude, Z_A=Depth) and its Length (***L***), Width (***W***), Strike (***θ***), Dip(***C***), Rake Angle (*γ*). (Note: 0<***θ***<360, 0<***ϕ***<90, -180<***γ***<180).
- Compute the coordinates of the remaining three corners B, C, and D (AB=***L***, CD=***L***, BC=***W***, and CD=***W***). If the coordinates are expressed in degree, then degree-to-length conversion is used; if expressed in km, then there is no conversion.
- The coordinates of the hypocenter (rupture initiation point) are: ***X*, Y*, Z**** (***X**** and ***Y**** are in degrees or in km and ***Z**** is in km).
- Digitize the rectangular (or quadrilateral) -shape fault plane ABCD into ***N*** number of 1km by 1km sub-faults. The coordinates of the centers of the sub-fault ***i*** are X_i, Y_i, Z_i. Alternatively a sufficient (***N'***) number of randomly picked sub-faults can be used by drawing two random numbers between 0 and 1 (one random number determines the location of the sub-fault ***i*** along the strike (length) and the other random number determines the location of the sub-fault across the dip (width).
- Use the coordinates of the hypocenter (***X*, Y*, Z****) and the coordinates of the rupturing sub-fault ***i*** (X_i, Y_i, Z_i) to compute the "rupture unit vector" vector, ***p*** (along the vector connecting hypocenter and sub-fault ***i***).
- Use the coordinates of the rupturing sub-fault ***i*** (X_i, Y_i, Z_i) and the coordinates of the site (X_s, Y_s) to compute the "rupture to site unit vector" vector, ***q*** (along the vector connecting the sub-fault ***i*** and site).
- Using the unit vectors ***p*** and ***q***, compute the rupture-based directivity parameter ξ_p ("excluding the rupture length effect" at this stage) as:

$$\xi_p' = (\Sigma p.q)/N \tag{3.2}$$

- Compute the "unit slip vector", ***s***, for the sub-fault ***i*** using rake angle (γ) and the information on the geometry of the fault (item1 above). When the rake angle is assumed the same for the entire fault, ***s*** would not depend on the (location of the) sub-fault. The relation for the slip unit vector ***s***, as a function of the rake angle and the geometric parameters of the fault is given by Aki and Richards [1980]. In general (when $\gamma \neq 0, 90, 180, 270$), the slip unit vector ***s*** can be decomposed into a strike-slip part (with components along ***X, Y, Z*** coordinates) and a dip-slip part (with components along ***X, Y, Z*** coordinates). The components of the slip unit vector ***s*** in the ***X, Y, Z*** (*Long, Lat, Depth*) coordinates are:

$$s_x = \pm\{+\sin(|\gamma|)*\cos(\phi)*\cos(\theta)-\cos(|\gamma|)*\sin(\theta)\} \quad (3.3a)$$

$$s_y = \pm\{-\sin(|\gamma|)*\cos(\phi)*\cos(\theta)-\cos(|\gamma|)*\cos(\theta)\} \quad (3.3b)$$

$$s_z = \pm\{-\sin(|\gamma|)*\sin(\phi)\} \quad (3.3c)$$

- The choice of the +/- sign in the above equations depends on the (along-the-strike and across-the-dip) location of the rupturing sub-fault relative to the location of the hypocenter. In particular, the proper choices of the signs would allow different characterization for directivity effects of reverse faults and normal faults.

- Using the unit vectors ***s*** and ***q***, compute the slip-based directivity parameter ξ_s' ("excluding the rupture length effect" at this stage) as:

$$\xi_s' = (\Sigma s.q)/N \quad (3.4)$$

- The directivity parameter for the site is taken as either ξ_p' or ξ_s' or a weighted average of the two. Assigning relative weights *a* and *1-a* to contributions from the direction of slip and the direction of rupture respectively, the total directivity parameter is written as:

$$\xi' = a*\xi_s' + (1-a)*\xi_p' \quad (3.5)$$

- In the absence of information on the rake angle, ξ_p' can be used and when information on the rake is available and information on the location of the hypocenter is not available or is unreliable, ξ_s' can be used (Analyses results and a summary discussion of this subject is presented in Section 3.6). When both sets of information are available, the weighted combination found to be most effective in capturing directivity gives equal weights to the two:

$$\xi' = 0.5*\xi_s' + 0.5*\xi_p' \quad (3.6)$$

- Based on two alternative definitions for the directivity parameter ξ two models for directivity are constructed: The summations in Equations (3.2) and (3.4) can be taken over *(i)* the sub-faults with positive directivity effect (positive ξ'), or *(ii)* all sub-faults (considering both positive ξ' and negative ξ' on each sub-fault). These two alternative ways of treating ξ' will ultimately result in *Model-I* and *Model-II*. The theoretical range for ξ' is (0, +1) in *Model-I* while it is (-1, +1) in *Model-II*. For

Model-II one can use the transformation $\xi' \Rightarrow 0.5*(\xi'+1)$ to change the range to (0, +1).

Values of ξ' for *Model-I* and *Model-II* for the sites in the NGA-W2 (large magnitude database with finite fault information) have been computed and placed in the NGA-W2 flatfile.

3.2.2 Rupture Length De-Normalization Term, *LD*

ξ' should be "un-normalized" with respect to the extent of fault rupture (expressed in km). This, which ensures that same directivity effect is obtained for the same length of rupture, is accomplished by using the following expression for *LD*, the rupture Length De-Normalization factor:

$$LD = \ln(L_{rup})/\ln(L_{rup\text{-}max}) \tag{3.7}$$

where $L_{rup\text{-}max}$ is the "effective rupture length" corresponding to M_{max} for the NGA-W2 GMPEs (specifically $L_{rup\text{-}max}$=*400 km* is chosen, which roughly corresponds to the rupture length of an ~***M8.5*** strike-slip earthquake, the M_{max} based on which the NGA-W2 GMPEs are developed.)

The parameter L_{rup} is defined as:

$$L_{rup} = \sqrt{(L_s*L_s+W_{rup}*W_{rup})} \tag{3.8}$$

where for a single-segment fault L_s is the (horizontal) projection of rupture (in km) between the epicenter and the site on a line connecting the epicenter and the site and W_{rup} is the portion (in km) of the width of the fault which ruptures up-dip from the hypocenter to the top of the fault. The above expression for L_{rup} should be used for all fault types (strike-slip, reverse, and normal).

3.2.3 ξ' and *LD* for Multi-Segment Faults

The steps for computing ξ_p', ξ_s', and ξ' at a site for a multi-segment fault are generally similar to the ones for single-segment faults, described above. Specifically, the followings should also be noted:

- For a multi-segment fault the sub-fault summations are on the surface area of the entire fault (all segments). Therefore, each (rectangular/quadrilateral plane) segment, with the coordinates of the four corners known, should be first digitized into 1km by 1km sub-faults (or alternatively, a sufficiently large number of randomly picked sub-faults over each segment be used). Then, a "rupture unit vector, ***p***", a "slip unit vector, ***s***", and a "sub-fault to site unit vector ***q***" should be computed for each sub-fault. The expressions for ξ_p', ξ_s', and ξ' are the same as for the case of single-segment fault, except that ***N*** now represents the combined number of sub-faults for all fault segments.
- The rupture unit vector ***p*** for a sub-fault on a segment which does not contain the hypocenter is computed based on the "shortest traveled hypocenter to sub-fault distance" or the "rupture path closest to straight line". Theoretically, all possible paths that begin from the hypocenter and pass through various sub-faults located at the edges of all segments between the hypocenter and the targeted sub-fault should be tested to determine the shortest path and the unit vector ***p***. This would result in $W^{(Nseg-}$

[1)] different rupture paths, of which the shortest one needs to be determined (where ***W*** is the fault width and ***NSEG*** is the number of segments); a computationally tedious task! With a slight and negligible error of approximation, only the sub-faults located at the edge of the fault segment containing the targeted sub-fault need to be considered. In other words, to find ***p*** on a sub-fault located on fault segment ***j***, the hypocenter should be connected to every sub-fault element at the edge of fault segment ***j***, and from there to the sub-fault and the shortest of these ***W*** alternative travel paths be identified and based on that the unit vector ***p*** for the sub-fault be determined.

- There is no difference in the computed directivity parameters for the cases of (100%) right-lateral and left-lateral strike-slips. Furthermore, the rupture-based ξ_p' and the slip-based ξ_s' are identical for purely strike-slip faults.
- To "un-normalize" ξ', the same expression for *LD* which was used for single-segment faults will be used, with the exception that L_s is replaced with L_i , the (horizontal) sum projection of ruptures (in km) on all segments of the fault between the epicenter and the site on a line connecting the epicenter and the site, but W_{rup} is the same as before.

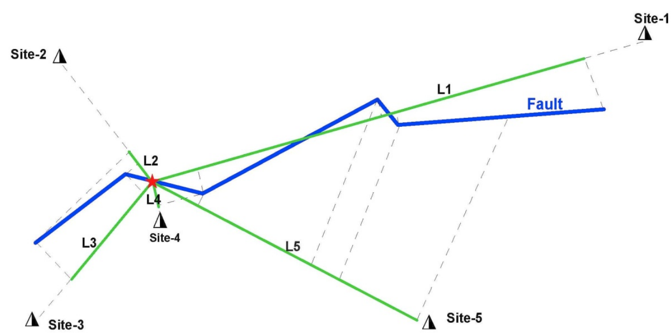

Figure 3.2 Illustration of the equivalent horizontal rupture length L_s in Equation (3.8) (L_1, L_2, etc. here).

3.2.4 Distance Taper Term, *DT*

The directivity term, with the directivity parameter ξ' should also be multiplied by a Directivity-Distance taper, *DT*. Including the distance-taper would ensure that the directivity effects become smaller with distance from the source and diminish to zero beyond a certain distance. This "taper distance" could be taken to be independent of any parameter, such as earthquake magnitude, fault dimensions, or ground motion period or it could be dependent on any of these (or any other) parameters. The Directivity-Distance Taper term proposed for this model is dependent on the period of ground motion. In the previous version of the model, which was developed mainly based on the NGA-W1 database [Rowshandel 2010] it was learned that directivity effect is distance-dependent; that it has its largest value in a region close to the source and diminishes with distance from the source. It was further observed that this distance range of strong directivity is period-dependent. Based on these, and similar observations made from analyses of the NGA-W2 data (e.g., comparing directivity effect using the 0-50km residuals and 0-200km residuals), a period-dependent Directivity-Distance taper correction term for the directivity model in study seems to be appropriate. Therefore, directivity effect is assumed to remain constant within a period-dependent distance, R_1, decrease with distance to zero at a period-dependent distance, R_2, and be non-existent beyond R_2. Specifically,

$$DT = 1 \text{ for } R_{cls} < R_1$$

$$DT = DT(R,T) = 2 - R_{cls} / \{20+10Ln(T)\} \quad \text{for } R_1 < R_{cls} < R_2, \tag{3.9}$$

$$DT = 0 \quad \text{for } R_{cls} > R_2$$

where

R_1=20+10Ln(T)), R_2=2*(20+10Ln(T)), $T \geq 1$ sec

R_1=20, R_2=40, $T<1$ sec

R_{cls} is the closest rupture distance in km and T is the ground motion period.

A simpler, period-independent DT term, which may be used instead of the above relation is the following:

$$DT = 0$$

$$DT = 1 \text{ for } R_{cls} < R_1$$

$$DT = DT(R) = 2 - R_{cls}/35 \text{ for } R_1 < R_{cls} < R_2, \tag{3.10}$$

$$DT = 0 \quad \text{for } R_{cls} > R_2$$

with

R_1 = 35 km

R_2 = 70 km

The relation used for the results presented in this report is the period-dependent relation of Equation (3.9).

3.2.5 Narrow-Band Multiplier, *WP*

In this section the "narrow-band" effect in the model is investigated. The methodology used to study the narrow-band effect and to quantify and include this effect into the model is as follows:

1. For periods in the range of 0.3 sec to 10 sec (specifically, 0.3, 0.5, 1, 2, 3, 4, 5, 7.5, and 10 sec) the directivity coefficients C_1 and C_2 and the directivity correlation coefficient, R^2 (the linear correlation between the rupture-length de-normalized directivity parameter and the intra-event residuals) were computed. These three coefficients were obtained for all earthquakes with finite fault data, using the intra-event ground motion residuals within the 50 km of the faults, of all five NGA-W2 GMPEs. The big majority of the directivity computations (for the majority of the earthquakes in the database and most of the periods) resulted in positive directivity (i.e., $C_1>0$), although there were few earthquakes within the

database that exhibited negative directivity at all periods listed above. The results for positive directivity (specifically, C_1 and R^2) corresponding to the five GMPEs, for directivity *Model-I*, are listed in Tables B.1 through B.5 in Appendix B.

2. Variations of the directivity coefficient C_1 (which determines the level of directivity) and of R^2 were plotted as functions of the ground motion period T. Graphs of R^2-vs.-T for a number of earthquakes are shown in Figure B.1 (Appendix B). Based on these plots of C_1-vs.-T and R^2-vs.-T, the period (or periods) corresponding to maximum directivity for each earthquake was (were) identified. In the big majority of the cases, these "directivity-dominant" periods, when identified based on the maximum C_1 and maximum R^2 were the identical. When this was not the case, the "directivity-dominant period" (labeled as T_p, and hereafter referred to as "pulse period") was identified based on the maximum of R^2. In other word, the "Directivity Pulse Period", T_p, for an earthquake is defined as the period at which the ground motion residuals of that earthquake attains its maximum correlation with the directivity parameter.

   An examination of Figure B.1 (Appendix B) indicates that, based on the approach explained above, while most of the earthquakes with finite-fault data within the NGA-W2 database have one clear pulse period, some have more than one; a number of them have two and few have three. This feature very likely is due to the heterogeneity in the source rupture, such as the existence of several significant asperities distributed over the fault surface area. The directivity model presented here has the capability to easily address issues related to directivity pulse and source rupture characteristics, but the study of such issues is beyond the scope of the present work.

3. Directivity pulse periods are identified for each earthquake with finite fault data used in each of the five GMPEs. The pulse periods corresponding to most earthquakes commonly used in multiple GMPEs turn out to be the same or close. Using the pairs of pulse period and earthquake magnitude data, Magnitude-Pulse Period relations corresponding to all GMPEs were obtained. The following approximate T_p-M relation based on the combined results of the five GMPEs is also obtained which is shown in Figure 3.3 and will be used for narrow-band analyses of the model.

$$T_p=exp(1.27M-7.28) \tag{3.11}$$

   Table 3.1 shows the set of earthquakes with their pulse periods used to obtain this relation. Since different sets of earthquakes have been used for the five GMPEs the T_p-M relation based on individual GMPEs will be different than what is presented here in Equation (3.11) and in Figure 3.3. This approximate relation should therefore be considered a "weighted average" based on five sets of ground motion residual data. Another important point concerning the T_p-M relation is the fact that the information used to develop it is especially inadequate for lower magnitude earthquakes (e.g., below *M6*). Therefore, constraining the relation at lower magnitude and shorter pulse periods can be significantly improved with additional data for the lower end of the relation.

4. Observing the variation of directivity in the vicinity of the "pulse periods", a normal distribution, centered at T_p, with a standard deviation, represented as *Sig* was seen to be satisfactory fit. The following expression was therefore used for the "Narrow-Band Multiplier, *WP*":

$$WP=exp\{-[log_{10}(T/Tp)*log10(T/Tp)]/(2*Sig*Sig)\} \tag{3.12}$$

The value assigned to *Sig*, the narrow-band directivity bandwidth, is 0.6. This is based on the values obtained for this parameter for individual NGA-W2 earthquakes with finite fault data (which as can be seen from Figure B.1 mostly fall in the range 0.1 to 0.6) and other considerations as discussed in Appendix B.

Table 3.1 Dominant directivity pulse periods (in sec) for some of the earthquakes with finite fault data in the NGA-W2 database.

EQID	**Earthquake Name**	***M***	T_p	***EQID***	**Earthquake Name**	***M***	T_p
30	San Fernando	6.61	5	136	Kocaeli, Turkey	7.51	8
48	Coyote Lake	5.74	0.5	137	Chi-Chi, Taiwan	7.62	10
50	Imperial Valley-06	6.53	4	172	Chi-Chi, Taiwan-03	6.2	2
64	Victoria, Mexico	6.33	1	173	Chi-Chi, Taiwan-04	6.2	2
68	Irpinia, Italy-01	6.9	4	174	Chi-Chi, Taiwan-05	6.2	3
69	Irpinia, Italy-02	6.2	2	175	Chi-Chi, Taiwan-06	6.3	2
90	Morgan Hill	6.19	4	176	Tottori, Japan	6.61	1
91	Lazio-Abruzzo, Italy	5.8	1	177	San Simeon, CA	6.5	2
101	N. Palm Springs	6.06	2	179	Parkfield-02, CA	6	2.5
102	Chalfant Valley-01	5.77	0.5	180	Niigata, Japan	6.6	0.5
103	Chalfant Valley-02	6.19	1	274	L'Aquila, Italy	6.3	5
116	Superstition Hills-02	6.54	5	277	Wenchuan, China	7.9	10
118	Loma Prieta	6.93	3	278	Chuetsu-oki, Japan	6.8	7.5
123	Cape Mendocino	7.01	4	279	Iwate, Japan	6.9	7
125	Landers	7.28	10	280	El Mayor-Cucapah	7.2	7.5
127	Northridge-01	6.69	7	281	Darfield, New Zealand	7	7.5

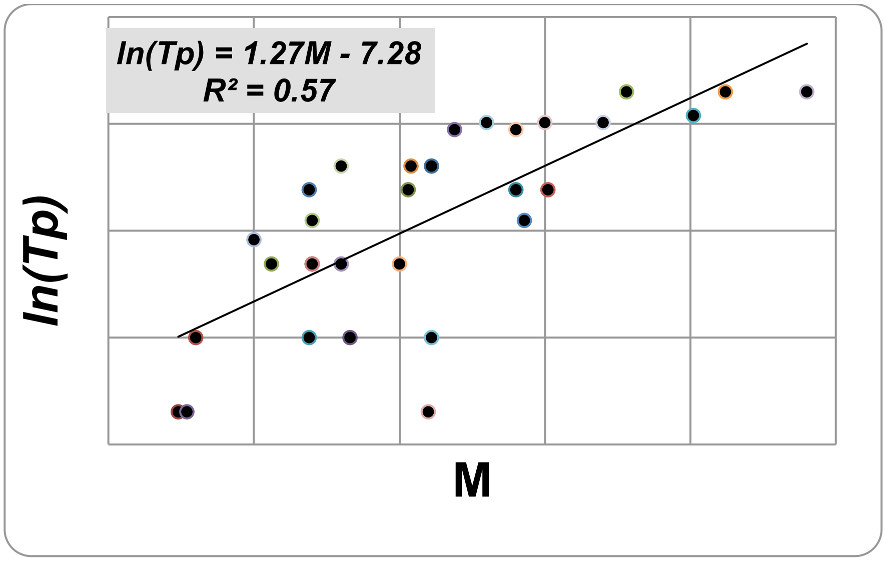

Figure 3.3 **Approximate Pulse Period – Magnitude (T_p-M) relation for NGA-W2 earthquakes with finite fault data, based on five GMPE residuals.**

3.3 IMPACTS ON SIGMA

Including a directivity term into a GMPE obviously has the effect of changing the variability in the predicted ground motions. With directivity models developed with the purpose of capturing contributions to the ground motions due to azimuthal effects, to include a directivity term in a GMPE is expected to have the effect of reducing the overall variability of the predicted ground motions. In other words, addition of a directivity term, while at the same time alters the level and distribution of ground motions around a source it should bring down the value of sigma in the GMPE. A conventional (no-directivity) GMPE implicitly and in an average sense include some contributions to ground motions due to source rupture characteristics, including the direction of rupture or slip (as these effects are already present in the ground motion records used in the development of GMPEs). Depending on the seismological parameters that exist in a GMPE, a portion of directivity effects, or the directivity at certain regions around the fault, can also be picked up by certain parameters. These potentially include terms representing hanging wall effects, the effects of top-of-rupture location, and even the "distance" metric. In view of these, a simple analysis of the change in sigma based on adding a directivity term to an existing GMPE (which explicitly lacks directivity features) is not sufficient for assessing the impact of the model on sigma. Nonetheless, this can serve as a simple way to evaluate a directivity model and at least it brings into light some features and capabilities of directivity models and also some of the implications of the using such models in practice.

In this section a series of analyses have been performed to explore and roughly quantify the impacts of including the directivity model developed in this chapter into the NGA-W2 GMPEs. In particular, the following tests have been performed:

- The effects of the directivity model with GMPE-specific coefficients on the intra-event sigmas of the five GMPEs were calculated. This is performed using two versions of the model, referred to as *Model-I*, and *Model-II*. Recall that *Model-I* was developed based on the assumption that subfaults which rupture or slip away from the site have no contribution to the directivity parameter ξ, whereas in *Model-II* contributions from all subfaults are accounted for. Results for a number of ground motion periods between 1 and 10 seconds are shown in Figure 3.4.

- The effects of the directivity model with GMPE-specific coefficients on the intra-event sigma of individual earthquakes "within" the GMPE database were studied. This was performed for a number of earthquakes, specifically: Imperial Valley, Landers, Northridge, Chi-Chi, Wenchuan, and Darfield. Results for A&S and B&A GMPEs and *Model-I* are presented in Figure 3.5.
- The effects of the directivity model with earthquake-specific coefficients on the intra-event sigmas of individual earthquakes in the GMPE database were also studied. Results, using A&S and B&A intra-event residuals for Imperial Valley, Landers, Northridge, Chi-Chi, Wenchuan, and Darfield earthquakes and *Model-I* are presented in Figure 3.6.
- The effects of the directivity model with GMPE-specific coefficients on the intra-event sigma of individual earthquakes "outside" the GMPE database were studied. This was performed on intra-event residuals of earthquakes that are not a part of the database of the GMPEs. For this purpose, the ground motion residuals of Chi-Chi aftershocks by A&S and C&Y (EQIDs: 172, 173, 174, and 175) were used with directivity coefficients of C&B and B&A. These latter two GMPE models do not include Chi-Chi aftershocks in their database. Results of this part of the study based on *Model-I* are summarized in Figure 3.7.

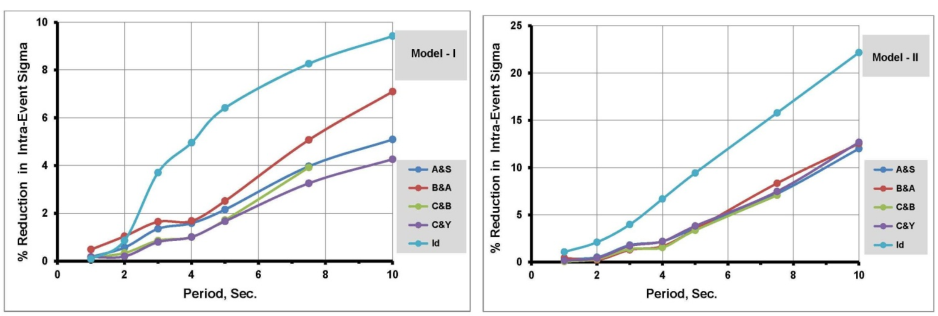

Figure 3.4 **Percentage reduction in the intra-event sigmas of the five sets of ground motion residuals.**

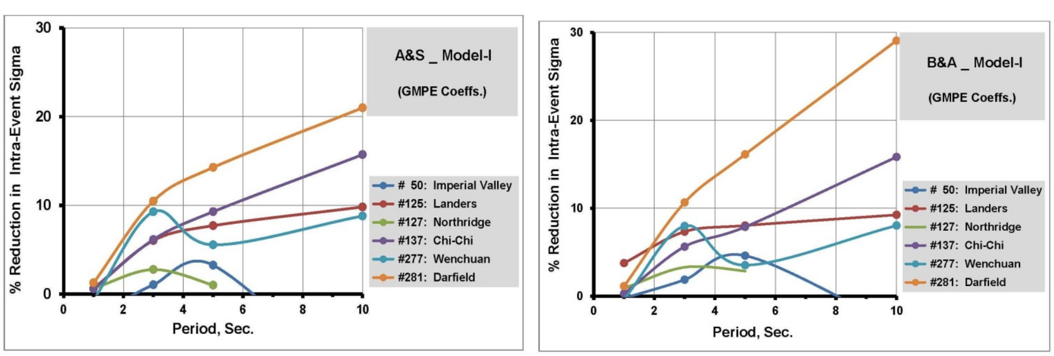

Figure 3.5. **Percentage reduction in the sigma of some individual earthquakes based on GMPE-specific directivity coefficients in A&S model (left) B&A model (right).**

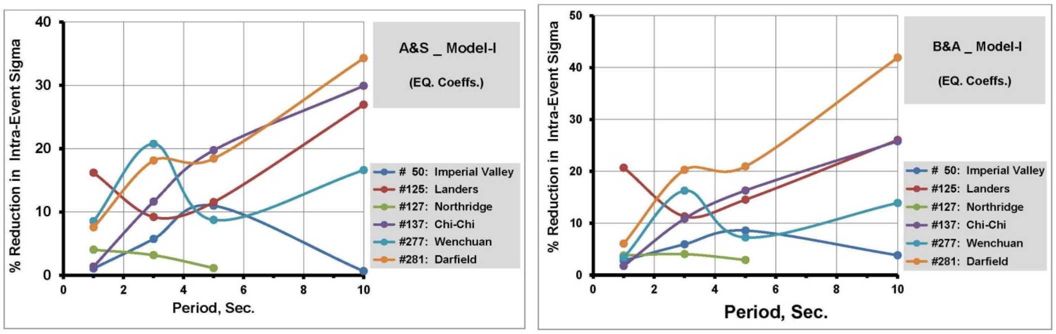

Figure 3.6 Percentage reduction in the sigma of some individual earthquakes based on the earthquake-specific directivity coefficients in A&S model (left) B&A model (right).

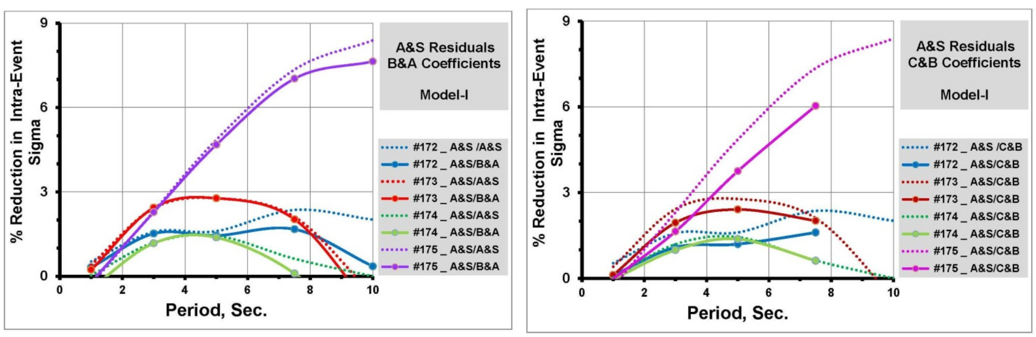

Figure 3.7 Percentage sigma-reductions for some individual earthquakes outside the database using which the GMPE-specific directivity coefficients are obtained. The A&S (intra-event) sigma reductions in Chi-Chi aftershocks using the directivity coefficients of B&A model (left) and C&B model (right). Chi-Chi aftershocks are not used in either of the two (B&A or C&B) models. The dotted curves show the sigma reductions using A&S GMPE-specific directivity coefficients.

Based on the results depicted in Figures 3.4 through 3.7, the following statements regarding the impact on the intra-event sigma, of the directivity model presented in this chapter can be made:

- Depending on the specific GMPE model used, reductions of intra-event sigma, of roughly up to 5-10% at the ground motion period of 10 second are expected based on directivity Model-I. The reductions are significantly larger for directivity Model-II, roughly from 10-20%, depending on the GMPE used. From Figure 3.4, it is also clear that the directivity-caused sigma reductions are relatively larger for simpler GMPE models - that is models that use a smaller number of "seismological parameters". These include ID-GMPE and B&A GMPE. ID-GMPE, in addition to having a small number of such parameters, uses a much smaller subset of the NGA-W2 ground motions. The other three GMPEs have parameters that could potentially capture some of the directivity effects in the ground motions records, parameters such as hanging-wall, depth to the top-of-rupture, and hypocentral depth. Simultaneous regressions on these parameters, with the directivity parameter also present, could resolve this issue.

- From Figure 3.5 it is observed that use of this directivity model in a GMPE, while in total reduces the intra-event sigma, would have different (levels of) effects on different earthquakes. In general, larger reductions in sigma for larger (especially strike-slip) earthquakes, larger reductions of sigma at longer periods in larger earthquakes and larger reductions at shorter periods for smaller earthquakes (narrow-band effect) are to be expected. Reduction in intra-event sigma of as much as 20-30% at long periods, and as much as 10-20% at intermediate periods for large strike-slip earthquakes could also occur. It should also be noted that not every earthquake within a GMPE database undergoes a sigma-reduction upon the application of the model. And in fact, not every period for the directivity-positive earthquakes exhibit sigma reduction.

- When the directivity model is applied directly to individual earthquakes; that is, when earthquake-specific directivity coefficients are used, relatively large reductions in sigma could result. This is illustrated in Figure 3.6 where the application of the directivity Model-I to Darfield ground motions would result in reductions in sigma of as much as 35-40% at 10 seconds and of ~20% at 3 seconds, according to A&S and B&A GMPE models.

- The real test and often the intended application of any model (or of any theory in general) is to predict what is beyond and outside the realm of information used to build the model. To that end, the model needs to be tested using new data. Ground motions from crustal California-type earthquakes (non-NGA-W2) would be ideal for such tests of the present model. In the absence of such data, some of the information in the NGA-W2 can serve that purpose. Specifically, since Chi-Chi aftershocks, which has been determined to be crustal California-type earthquakes, have not been used in B&A and C&B GMPEs, they can be used to test the directivity model for "new data", if the directivity model coefficients of B&A and C&B are applied to ground motion residuals of Chi-Chi aftershocks in A&S and C&Y GMPEs. Or, similarly, if directivity model coefficients using ID-GMPE are used on ground motion residuals of the other four GMPEs for earthquakes not used in ID-GMPE. Figure 3.7 illustrates the sigma-reducing capability of the directivity Model-I for new earthquakes, when used in combination with the B&A and C&B GMPEs. In this figure, the dotted curves are the reductions in (A&S) sigma in individual aftershocks based on A&S-own directivity coefficients and the solid curves indicate the reductions in (A&S) sigma based on B&A (left) and C&B (right) directivity coefficients). Therefore, the degree that the solid curves are close to the dotted curves is an indication of how reliably the directivity model can be used to predict the effects in future earthquakes.

- Another observation from all results presented in Figures 3.4 through 3.7 is the very small and in some cases negligible effects at periods below 1 second. Strong directivity may or may not be present at short periods (e.g., below 0.5 seconds). This effect at very short periods has been reported in the literature. The effect cannot be reliably accounted for in models such as the one presented in this report, in part because the big majority, or perhaps all, records in the NGA-W2 database of finite fault data, represent "moderate-to-large magnitude" events. Directivity at very short periods seems to be caused by earthquakes of small magnitudes (M≤5), which is lacking in the database. The narrow-band feature of the model, presented in a previous section, could to some extent improve the behavior at short periods. But the narrow-band analyses of the data, using the directivity features of smaller magnitude earthquakes (5.5<M<6) did not provide sufficient reliable information to constrain the model. Slightly larger directivity effects were observed in earlier (wide-band) versions of the model. Therefore, it could also be concluded that, even a relatively large bandwidth (Sig=0.8) if used for this model is not large enough to capture the effects of large magnitude earthquakes at very short period. In order to improve the model capabilities at very short periods, further testing of the model against ground motions and reliable finite-fault data (fault geometry, hypocenter location, and mechanism-rake angle) of smaller magnitude earthquakes (M<6) are needed.

3.4 DIRECTIVITY CENTERING

A summary of the results of the analyses and computations performed to determine the directivity centering constant (ξ'_c and ξ_c) is presented in this section.

As briefly explained earlier, conventional GMPEs (ground motion models which do not explicitly include a directivity term) still take some account of rupture directivity effects in the average sense. In such models, while there is no azimuth-dependency in the predicted ground motions, a portion of the ground motions predicted is the captured effects of directivity which are present in the recorded ground motions based on which these models are developed. One consequence of the presence of this averaged directivity in conventional GMPEs is that the directivity models, such as the one being addressed in this chapter, cannot be simply used as an add-on directivity correction term to GMPEs lacking directivity features. In order to correct for this potential double counting of directivity in directivity-corrected GMPEs, and for other potential uses, a "centering value" for any directivity model is needed.

To find a directivity centering constant to be used in Rowshandel Directivity Model, analyses based on two approaches were performed. In the first approach, the finite fault data of the NGA-W2 flatfile was used to compute the "azimuthal average" of the model directivity parameter ξ (using the so-called "race-track" approach). As a result, the azimuthal averages of the directivity parameter before "rupture length" de-normalization as well as after "rupture-length" de-normalization were obtained. These directivity centering values are called ξ'_c and ξ_c respectively. In view of the distance-dependency of the directivity effect, the azimuthal-averaging was performed over different distance bins around the rupturing faults used in the analyses. The distance metric used was R_{cls} (the closest distance to rupture) and the distance increment was 5 km, with first bin between 2.5 and 7.5 km (centered at 5 km) and the last one between 47.5 and 52.5 km (centered at 50 km). All faults with finite fault information were used in the analyses. The results are presented in Figures 3.8(a) and 3.9(a). The analyses were then repeated for the strike-slip events and the reverse-and-normal events. The results for these two faulting mechanisms are shown in Figures 3.8(b), 3.8(c), 3.9(b) and 3.9(c). The criterion used to separate the faults into strike-slip category and reverse-and-normal category was based on the rake angle. Specifically, for the purpose of creating results in 3.8 and 3.9, (b) and (c), ruptures with rake angles larger than 45 degree and smaller than 135 degree were counted as reverse, ruptures with rake angles larger than -135 and smaller than -45 degrees were counted as normal, and the remaining ruptures (with rake angles between -180±45 and +180±45) were assumed strike-slip.

The changes in the centering terms (ξ'_c and ξ_c) with distance for each rupturing source can also be seen in Figures 3.8 and 3.9. The details of the changes of these parameters with distance cannot be seen for individual faults, as these are somewhere between 30 to 80 faults contributing to the information presented in these figures! However, for all three faulting mechanisms the (azimuthal) average directivity is seen to generally decrease with distance, albeit mildly. The manner of the change in ξ'_c and ξ_c with distance depends on the geometry of fault, and particularly the number of fault segments and changes in the segment strikes, among other factors. The "average" values of ξ'_c and ξ_c are shown by black curves in these figures. Except for very near-source, where there are large variations in the distributions of the "average" directivity, the changes with distance are relatively small and gradual. The approximate distance-independent average values of the centering terms ξ'_c and ξ_c are indicated by the black broken lines. The data on the distribution of ξ'_c and ξ_c over the approximately 80 faults with finite-fault data used in the study, when fit to a "normal distribution" resulted in the "means" and "standard deviations" shown in Figures 3.8 and 3.9. The black dotted curves correspond to mean ±1 standard deviation.

Another approach to estimate the centering terms is to use the range of the directivity parameter at a site based on random hypocenters of uniform distribution over the fault surface area of many earthquakes. This was done using the Directivity Test Cases (SS1-SS7 and RV1-RV7).

For the users of the model, the recommended values of the centering term, in the absence of any information on the effective rupture length, the hypocenter location, and the rupture mechanism are those shown in Figure 3.9(a) (the generic rupture length de-normalized values). When only the mechanism is known the information given in Figures 3.9(b) and 3.9(c) should be used, and when the hypocenter location and/or the effective rupture length are known, or can be estimated, results presented in Figure 3.8 are more appropriate. When the length and the width of the fault are known but the location of the hypocenter is not, placing the hypocenter at ¾ of fault-length from the fault end closer to the site and at a location on the fault ¾ of fault-width from the top of the fault is recommended. This would result in an "effective rupture length" for de-normalization, of $L_{rup}=0.75\sqrt{(L^2+W^2)}$, where L is the total length of the fault and W is the width of the fault. It should also be noted that, if the rupture-length de-normalized values of the centering term (i.e. ξ_c from Figure 3.9) are used, de-normalization of the centering term, as a part of the directivity term is not needed, whereas ξ'_c from Figure 3.8 should be used in conjunction with the rupture length de-normalization term, *LD,* in Equation (3.7).

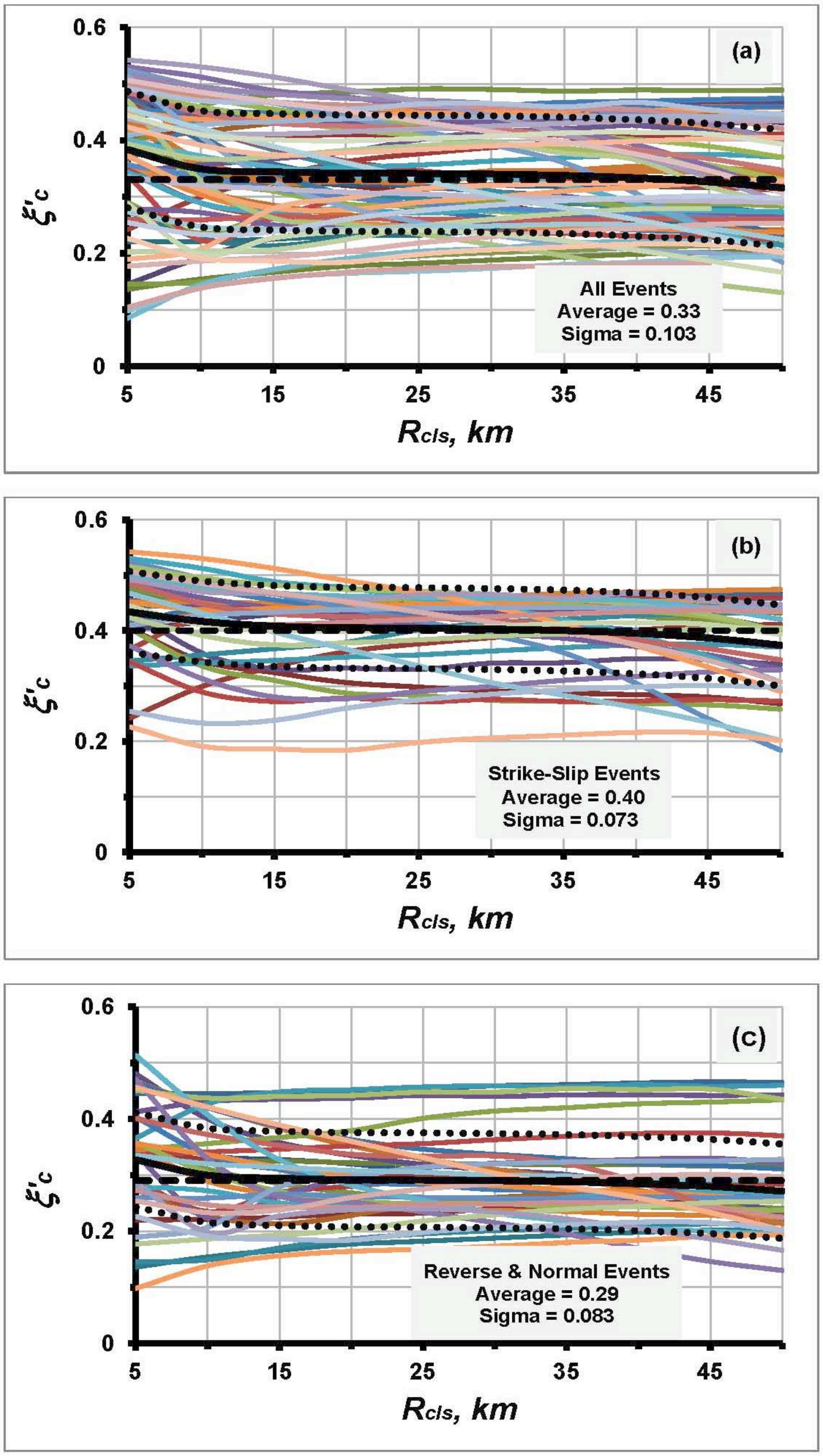

Figure 3.8 **Distributions of the rupture length normalized centering parameter ξ'_c based on the NGA-W2 finite fault data.**

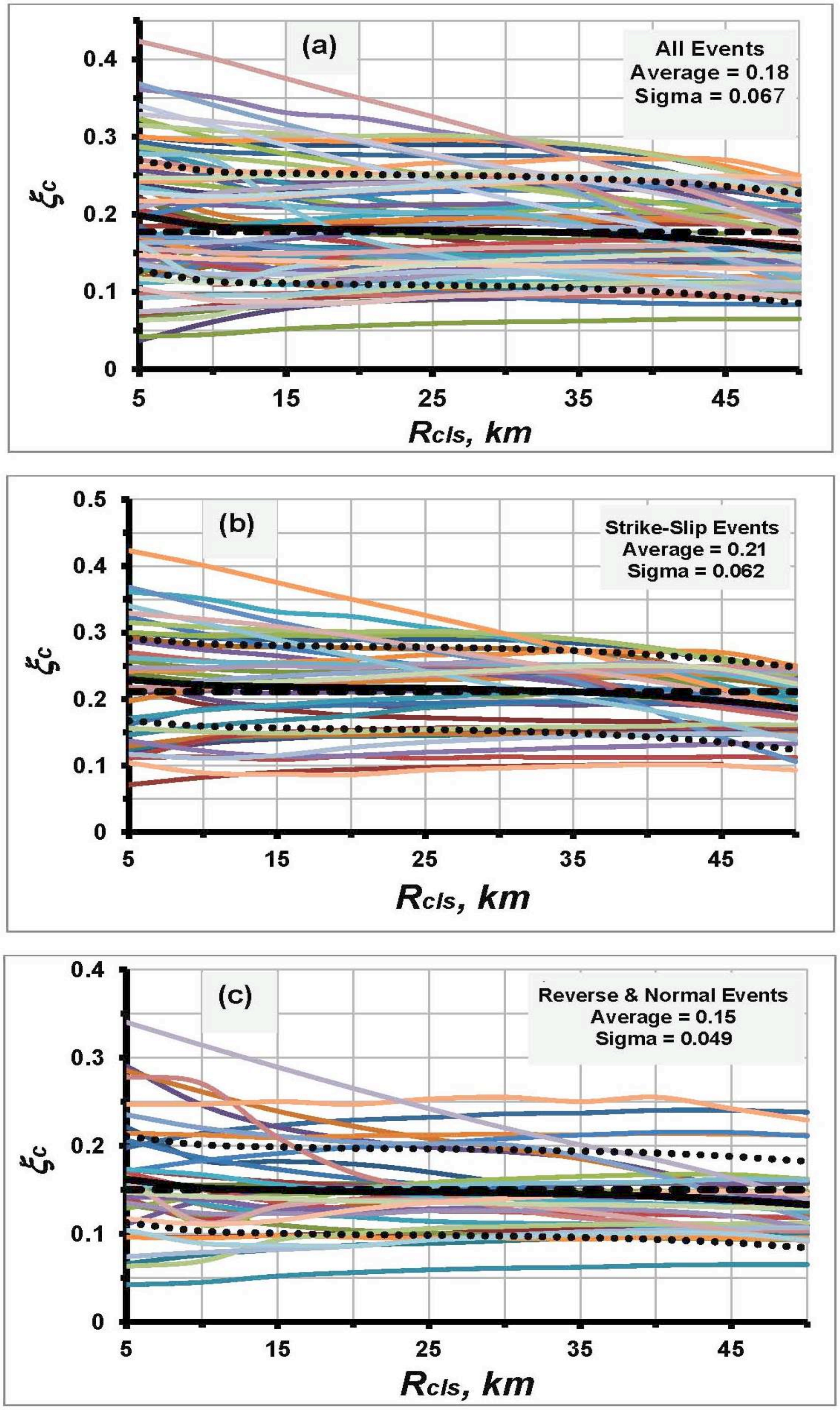

Figure 3.9. **Distributions of the rupture length de-normalized centering parameter ξ_c based on the NGA-W2 finite fault data.**

3.5 IMPLEMENTATION IN GMPES

The expression for the directivity function, or directivity term, f_D is:

$$f_D=(C_1\xi'+C_2)*LD*DT*WP \tag{3.13}$$

where ξ' is the directivity parameter before rupture length de-normalization is applied, LD is the rupture length de-normalization factor, DT is the (period-dependent) distance taper, WP is the narrow-band multiplier, and C_1 and C_2 are period-dependent directivity coefficients. C_2 does not play any role in determining the distribution of directivity or have any impact on sigma and it turns out to be zero if the sum of the intra-event residuals based on which ξ is calculated is zero (in other words, as a free parameter it reflects the data-set to data-set bias). Only when comparing the size (not the distribution) of directivity among various directivity models its value might become relevant. In any case, C_2will be absorbed in the "directivity centering term" when that term is added to the model. Therefore, dropping C_2 and replacing $\xi'*LD$, the rupture length de-normalized directivity parameter with ξ, and also including the (rupture length de-normalized) directivity centering term ξ_c, the expression for f_D becomes:

$$f_D=C_1(T)*(\xi-\xi_c)*DT(T)*WP(T) \tag{3.14}$$

where T represents ground motion period and the coefficient C_1, the distance tapering term, DT, and the narrow-band multiplier, WP are all period-dependent. The directivity term f_D is then added to a (conventional, non-directivity) GMPE:

$$ln(Y) = f(M,R,...,\varepsilon) + f_D \tag{3.15}$$

The following expression was derived for WP earlier. As stated earlier, this expression, the Earthquake Magnitude-Directivity Pulse Period (T_p) relation, and the approximate values of their coefficients are based on the intra-event residuals of four GMPEs (Figure 3.10 for a graphical representation of WP). The coefficients in WP are therefore GMPE-dependent, and hence they should be computed based on regressions for individual GMPEs. To be used in the regressions WP is therefore first written in the following form:

$$WP=exp\{-[log_{10}(T)-log_{10}(T_p))*(log_{10}(T)-log_{10}(T_p)]/(2*Sig^2)\} \tag{3.16}$$

Using the M-T_p relation, the above expression becomes

$$WP = exp\{-[a'/(Sig\sqrt{2})+b'M/(Sig\sqrt{2})]*[a'/(Sig\sqrt{2})+b'M/(Sig\sqrt{2})]\} \tag{3.17}$$

which further simplifies to:

$$WP = exp\{-(a_1+b_1M)^2\} \tag{3.18}$$

In equations (3.17) a' is a period-dependent coefficient and b' is a period-independent coefficient. If a value for the bandwidth (Sig) is assumed, and "Sig" is combined with a' and b', the narrow-band coefficients will be called a_1 and b_1, where a_1 depends on the ground motion period T and b_1 is period-independent. The final expression for the GMPE with the directivity term f_D included becomes:

$$ln(Y) = f(M,R,...,e) + f_D = f(M,R,...,e) + C_1(T)\,(\xi - \xi_c)*DT(R,T)*\,exp\{-(a_1(T)+b_1M)^2\} \quad (3.19)$$

Based on the intra-event residuals of the GMPEs, a set of values for the coefficient C_1 were obtained, which are presented in the next section. Assuming three different values for the bandwidth (*Sig* = 0.4, 0.6, and 0.8) and using the approximate relation between T_p and M, , the following values for the narrow-band coefficients a_1 and b_1 are obtained. These values can be used as initial values for regressions with the directivity model added to GMPEs (It should also be noted that upon further simplification of the last equation, the coefficient C_1 may be combined with the other two).

$$Sig = 0.4:\ \ a_1(T) = 1.768log_{10}(T) + 5.589;\ \ b_1 = -0.98$$

$$Sig = 0.6:\ \ a_1(T) = 1.179log_{10}(T) + 3.726;\ \ b_1 = -0.65 \quad (3.20)$$

$$Sig = 0.8:\ \ a_1(T) = 0.884log_{10}(T) + 2.795;\ \ b_1 = -0.49$$

The recommended bandwidth, based on the analyses of the interim versions of the intra-event residuals, is 0.6. Recommendations regarding the directivity centering term (ξ'_c, rupture-length normalized and ξ_c, rupture-length de-normalized) are presented in Section 3.4.

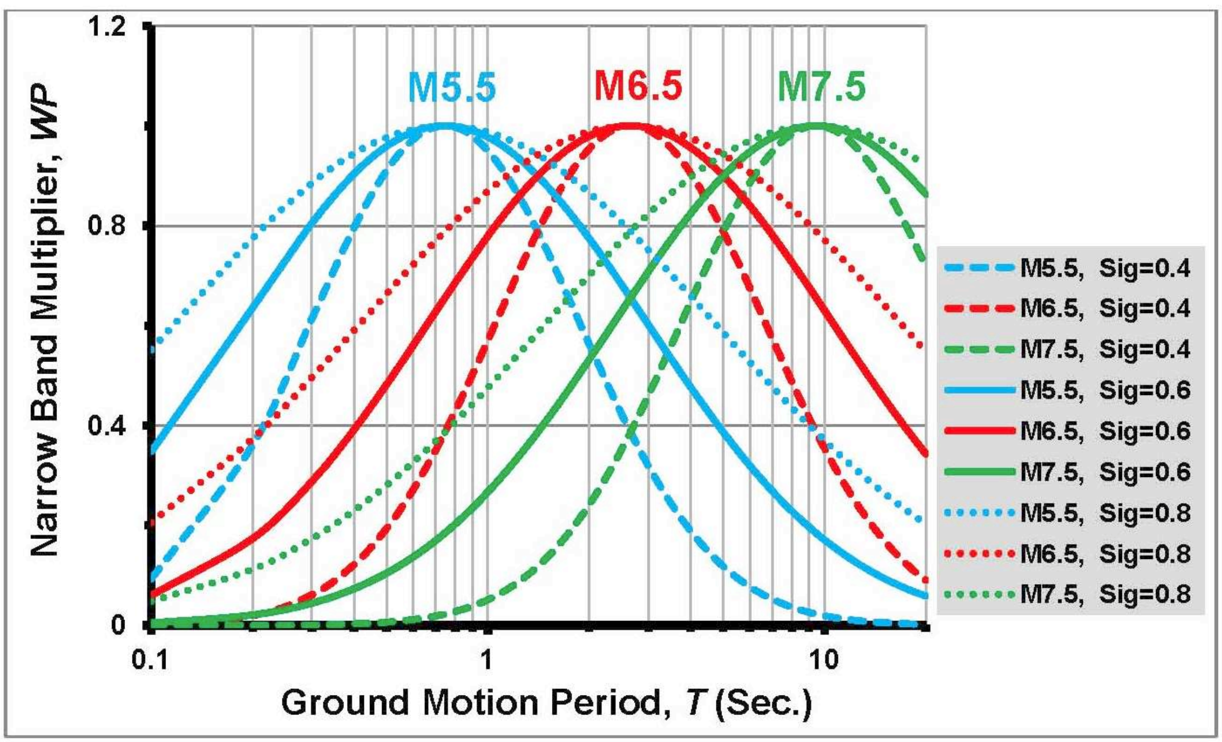

Figure 3.10 Graphical representation of the narrow-band multiplier *WP* for three magnitudes (5.5, 6.5, and 7.5) and three directivity pulse bandwidth (*Sig* = (0.4, 0.6, and 0.8) over the ground motion period range *T* = 0.1 to 20 seconds, based on the intra-event residuals of four NGA-W2 GMPEs and Directivity Model-I.

3.5.1 Model-I Preliminary Coefficients

Using the expression for the directivity term f_D, setting ξ'_c=0, and using NGA-W2 finite fault data and preliminary intra-event ground motion residuals at periods 1, 2, 3, 4, 5, 7.5, and 10 seconds from the five NGA-W2 GMPEs, model coefficients are computed. Table 3.2 presents these coefficients, consisting of C_1 and C_2 and the directivity-residual correlation coefficient R^2 for *Model-I*.

Table 3.2 Directivity coefficients based on five sets of ground motion residuals based on Model-I.

T	A&S			B&A			C&B			C&Y			Id		
(sec)	C_1	C_2	R^2	C_1	C2	R2	C1	C2	R2	C1	C2	R2	C1	C2	R2
1	0.375	0.028	0.004	0.257	0.024	0.002	0.149	-0.007	0.000	0.079	-0.003	0.001	0.325	-0.019	0.002
2	0.561	-0.071	0.011	0.699	-0.097	0.021	0.377	-0.057	0.007	0.321	-0.404	0.004	0.803	-0.082	0.017
3	0.833	-0.130	0.027	0.824	-0.133	0.033	0.570	-0.095	0.017	0.629	-0.098	0.016	1.544	-0.228	0.073
4	0.873	-0.146	0.031	0.834	-0.145	0.036	0.596	-0.106	0.020	0.693	-0.115	0.020	1.576	-0.255	0.097
5	1.019	-0.178	0.043	0.986	-0.182	0.050	0.772	-0.144	0.034	0.898	-0.156	0.033	1.823	-0.312	0.124
7.5	1.387	-0.250	0.078	1.378	-0.273	0.099	1.152	-0.230	0.077	1.258	-0.224	0.064	2.089	-0.358	0.158
10	1.551	-0.268	0.099	1.588	-0.319	0.137				1.369	-0.235	0.083	2.250	-0.369	0.180

3.6 VARIATIONS AND APPROXIMATIONS OF THE MODEL

A major revision from the Directivity Model presented in Section 3.5 and the previous versions of this model [Rowshandel 2006 and 2010] is the inclusion of the direction of slip (i.e., rake angle) as a contributor to the directivity effect. It has long been known (or at least asserted) that having the directions of rupture and the direction of slip *both* toward a site would result in increased directivity at the site. Analyses of the five NGA-W2 GMPE intra-event residuals, using the methodology presented in Section 3.2, confirmed this. Details on the correlation of directivity effects with the direction of rupture and the direction of slip (i.e., correlation of the intra-event residuals with the two separate measures ***p.q*** and ***s.q***) are not presented in this chapter. A short summary of analyses results on the correlation and dependence of directivity to the direction of rupture and to the direction of slip is presented in this section. Implications of the results for the use of the model, in particular simplifications of the model for different applications, are also briefly discussed.

As a part of the analyses which resulted in assigning equal weights to the direction of rupture and the direction of slip (***p.q*** and ***s.q***), i.e., selecting $a=0.5$ in Equation (3.5) the correlations of the five sets of intra-event residuals at periods between 0.3 seconds to 10 seconds with rupture-based directivity parameter (corresponding to $a=0$), with slip-based directivity parameter ($a=1$) and with combinations based on different relative weights of the two (i.e., varying a from 0 to 1) were investigated. The results indicated that, considering all periods and all five GMPE residuals, the highest correlations resulted from the choice of $a=0.5$, that is equal weighting of the roles of the direction of rupture and the direction of slip in defining directivity.

However, depending on the ground motion period and the GMPE, there were cases where *a=0.5* did not result in the maximum correlation between ground motion residuals and the directivity parameter. Approximate results based on the residuals of four GMPEs are presented in Figure 3.11. In this figure *C(0.5)* represents the directivity coefficient corresponding to *a=0.5* whereas *C(0)* and *C(1)* are respectively the coefficients corresponding to *a=0* and *a=1*, and *C(a)* is the coefficient for an arbitrary value of *a* between *0* and *1*. The ordinate of Figure 3.11 therefore shows the normalized directivity coefficients, and the abscissa is the rupture-and-slip weighting parameter. The results for *a=0* (all rupture), *a=1* (all slip) and *a=0.5* (rupture and slip weighted equally) in Figure 3.11 are from the analyses. However, the second order polynomial curves which pass through these three points are approximate interpolations, but they closely resemble results which would be obtained from analyses of the residuals for various values of *a* between *0* and *1* (not shown in this figure!). It should also be pointed out that nearly the same variations in the normalized linear correlation coefficient (R^2) would be obtained if the residual-directivity parameter correlation R^2 is used in place of *C* (i.e., one can approximately replace *C(a)/C(0.5)* by $R^2(a)/R^2(0.5)$ in Figure 3.11).

Even though in general setting *a*=0.5 would result in the optimum model, in practice this would require knowledge of the direction of rupture and the direction of slip over the fault. In other words, the hypocenter location and the rake angle, both, need to be known in advance, or be estimated reliably. For future earthquakes (earthquake scenario studies), depending on the information available, only one of the above two parameters may be reliably estimated. More often, the rake angle of future earthquakes might be more reliably estimated compared to the hypocenter location, for example, by using correlations between rake angle and the dip angle or from the general state of crustal stress around faults. In the early stages of an earthquake, when information on the mechanism of the event (e.g., rake angle) is not yet available and developing preliminary shake-maps with directivity effects could serve as a useful tool for early response activities, one can use a preliminary hypocenter location to use the present model. The model can therefore be used with a rupture-based parameter only (that is, setting *a=0* and disregarding the impact of slip vector) or with a slip-based parameter only (setting *a=1* and disregarding the impact of the direction of rupture), either with the original coefficients derived for *a=0.5* (such as those listed in listed in Table 3.2) or with coefficients multiplied by the *C(a)/C(0.5)* ratios shown in Figure 3.11, to get approximate results.

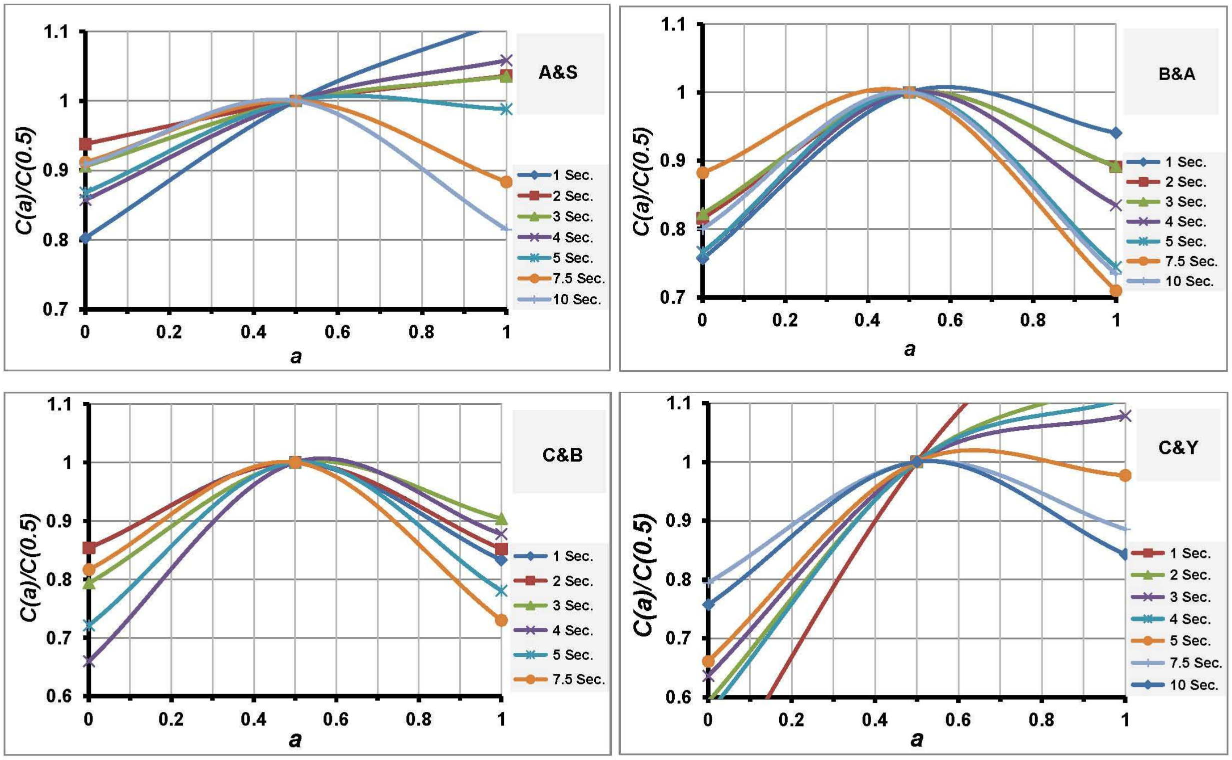

Figure 3.11. **Directivity coefficients for different weightings of the effects of rupture direction (*p.q*) and slip direction (*s.q*), normalized to the equal weighting of the two.**

3.7 CONCLUDING REMARKS

The directivity model presented in this Chapter is an improvement over the previous version of the model [Rowshandel 2010], which was developed based on the NGA-W1 data. In particular, the new model is superior in three respects, as explained below:

(i) It is "rupture length" de-normalized (details are in Sections 1.1.3 and 1.3.5.2).

(ii) The information on the effect of the direction of slip is taken into consideration, making the model capable of better capturing the directivity effects in earthquake ground motion records. As a result, the model can be used when either the location of the hypocenter or the direction of slip is known or can be inferred.

(iii) Due to the variations of the level of directivity with ground motion period and earthquake magnitude, which was revealed from the analyses of the data, the pulse-like feature of directivity was taken into account by making the model narrow-band.

Despite these general improvements, some features of this model (and likely the other models presented in this report) can still be further refined and improved. Specifically:

1. *"Distance Tapering":* The distance tapering (used in all models presented) has significant effects on the model predictions, both on the level of directivity-induced ground motion changes and on the distribution of such changes. In particular, the location of maximum directivity effect along the strike in strike-slip faults (whether it occurs within the fault ends or beyond, what is in Chapter 1 referred to as the "shotgun" end of the fault), which could depend on distance tapering, needs to be further investigated. Specifically, the period-dependency of the distance tapering is important. This issue was addressed to some extent in the present model, but it requires further study. Distance tapering for the present model can be performed on a sub-fault basis. The distance from a rupturing sub-fault to a site might be a better metric for distance tapering, and in fact if used properly in the present model, the "shotgun" effect, if unjustified, can be removed. This should be fully investigated.
2. *"Directivity at Short Periods":* This is another issue that should be further studied. The data for small magnitude events (e.g., M<6) used to develop the model, in particular records of small magnitude events with finite fault information, were not sufficient in number, and perhaps not of high enough quality, to constrain the model behavior at short periods. Existence of directivity at short periods, and the lack of capability of existing directivity models in capturing such effects, is an issue common to all models presented in this report. Directivity at very short period may be mostly confined within the very near source region (e.g., Rowshandel [2010]). If additional studies confirm this, the existing models with some minor refinements may be able to better capture such effects.
3. *"Directivity Pulse Characterization":* The narrow-band aspect of the model needs further refinement. The analyses of the directivity, which were aimed at identification and characterization of directivity pulses, indicted or implied the existence of multiple directivity pulses for some of the earthquakes in the database. For a number of the earthquakes in the database pulses with different periods and of comparable intensity were identified. Simply defining a single magnitude-dependent pulse for every earthquake, regardless of other potentially contributing factors, might be non-realistic. The existence of multiple pulses, each occurring at a different period, is consistent with multiple asperity characteristics of many past earthquakes. The performance of the present model in its narrow-band form was found to be relatively sensitive to the approximate Pulse Period versus Magnitude relation on which it was based. Better constraining of the Pulse Period-Magnitude relation at short periods and for small magnitude earthquakes is expected to result in significant improvements in the model.
4. "*Behind the Rupture Effects":* Analyses and the results presented in this chapter were mainly for the directivity *Model-I* (which excludes the directivity effects of sub-faults rupturing or slipping away from the site). Limited analysis of *Model-II*, which does include such effects, resulted in larger sigma-reduction capability of this latter model (Figure 3.4).

However, analyses of *Model-II* (such as applying the model on the test models for directivity comparison presented in Table 1.2) had not been completed at the time of writing this report. As a result, future research on the model presented in this chapter should include further development and evaluation of directivity *Model-II*.

5. *"Heterogeneity of Rupture":* The directivity model presented in this chapter (and in fact all models presented in this report) is based on the assumption of "homogenous rupture." While some characteristics of near-source earthquake ground motions can be addressed using such models, many near-source features are the consequences of heterogeneity of rupture and hence cannot be examined using the models presented in this report. Large variations in the directions of rupture and slip, in the sizes of slip and stress-drop, etc., over the surface area of rupturing faults, which are reported in many recent earthquakes, could affect near-source ground motions drastically. Upon further development, the model presented in this chapter can easily make use of such information to more realistically characterize the variability of near-source ground motions in future earthquakes.

4 Shahi and Baker Directivity Model

Shrey Shahi and Jack W. Baker

4.1 INTRODUCTION

This chapter provides a brief overview of the Shahi and Baker directivity model. For more details the reader is advised to see Shahi [2013]. The Shahi and Baker directivity model extends the approach of Shahi and Baker [2011] to explicitly account for directivity pulse effects in a ground-motion model. The model to predict $lnSa$ is divided into a base ground-motion model that predicts the intensity of records without any directivity pulse, and a pulse amplification model that predicts the amplification in intensity from a directivity pulse. The model can be represented by Equation (4.1) below:

$$lnSa_{ij} = f\left(M_i, R_j, T, Vs30_j, \theta, \dots\right) + I_{directivity} \cdot lnAmp\left(T, T_p\right) + \eta_i + \epsilon_{ij}. \quad (4.1)$$

The $f(M_i, R_j, T, Vs30_j, \theta, \dots)$ is the base ground-motion model that predicts the $lnSa$ at the spectral acceleration period of T seconds, from an earthquake of magnitude M_i at distance R_j and site with average shear wave velocity of $Vs30_j$. θ represents the model coefficients fitted using mixed effects regression. $I_{directivity}$ is an indicator variable that takes the value of 1 when the ground-motion contains a directivity pulse and takes the value 0 otherwise. $lnAmp(T, T_p)$ represents the amplification of $lnSa$ due to presence of a pulse. This is a narrow-band amplification function and amplifies the Sa at periods close to the period of the directivity pulse (T_p). The amplification function is modeled by Equation (4.2) below:

$$lnAmp\left(T, T_p\right) = b_0 \exp\left(b_1 \left(\ln\left(\frac{T}{T_p}\right) - b_2\right)^2\right) \quad (4.2)$$

where b_0, b_1 and b_2 are period-independent coefficients found using mixed effects regression. Fitting the Campbell and Bozorgnia [2008] functional form, with this directivity model to NGA-West2 data gives $b_0 = 0.72$, $b_1 = -1.10$, $b_2 = -0.19$. These values are anticipated to be similar to coefficients if fitting another functional form. Finally, η_i represents the between-event error and ϵ_{ij} represents the within-event error. The functional form used by Campbell and Bozorgnia [2008] is used as the base ground-motion model for this study.

4.2 PULSE CLASSIFICATION ALGORITHM

To fit the ground-motion model described in Equation (4.1) we need to classify each record in the NGA-West2 database as having a directivity pulse or not having a directivity pulse. We also need to compute the period of each identified pulse to fit the narrow-band amplification model described in Equation (4.2). A quantitative algorithm to identify ground-motions with directivity pulses is described in Chapter 4 of Shahi [2013]. The proposed algorithm can identify pulses at arbitrary orientations in multi-component ground motions, with little computational overhead relative to a single-orientation calculation. We use continuous wavelet transforms of two orthogonal components of the ground motion to identify the orientations most likely to contain a pulse. The wavelet transform results are then used to extract pulses from the selected orientations and a classification criterion is proposed, which uses the size of the pulse relative to the original ground motion and the peak ground velocity (PGV) of the original ground motion, to classify the ground motion as pulse-like or non-pulse-like. Since directivity pulses are found early in the time history, a criterion to reject pulses arriving late in the time-history is also proposed. The list of pulse-like ground motions was manually filtered using source-to-site geometry and site conditions to find pulses most likely caused by directivity effects. A list of ground motions with directivity pulses is provided in Shahi [2013], along with the periods of the pulses, the orientations in which the pulse was strongest and new models to predict probability of observing a directivity pulse and the pulse period for a given future earthquake scenario.

4.3 GROUND-MOTION MODEL PREDICTION

In this study we fit two ground-motion models: with and without directivity effects. The ground-motion model without any directivity terms used the functional form of Campbell and Bozorgnia [2008] but was refitted using the NGA-West2 database and without any smoothing of coefficients across periods. This model is called the CBR model (Campbell and Bozorgnia Refitted to NGA-West2). The ground-motion model with directivity effects is called the CBSB model (Campbell and Bozorgnia with Shahi and Baker directivity model). Details about fitting the ground-motion models are provided in Chapter 5 of Shahi [2013]. Here we present some comparison between the predictions from the two models.

4.3.1 Directivity Amplification

Presence of a directivity pulse amplifies Sa in a narrow band of periods close to the period of the pulse (e.g., Somerville [2003]). Thus, we expect a ground-motion model accounting for directivity effects to predict a different spectral shape than that predicted by a ground-motion model without any explicit directivity terms. Figure 4.1 shows the median response spectra predicted by the CBR and the CBSB models from a strike-slip earthquake of M 6.5 at a distance of 10 km ($R_{jb} = R_{rup}$ for vertical strike-slip fault). For this comparison the $I_{directivity}$ is set to 1 and T_p is set to 2.2 sec (the median T_p for $M = 6.5$). Note that specifying values of $I_{directivity}$ and T_p assumes occurrence of a particular pulse. One can assume occurrence of a particular pulse when computing ground-motion intensity from a specified scenario. However, when predicting ground motions from a future earthquake, one does not know the value of $I_{directivity}$ and T_p. In this case $I_{directivity}$ and T_p can be treated as random variables, $I_{directivity}$ can be modeled by a Bernoulli distribution and T_p can be described by a log-normal distribution. For more details about models to predict the parameters of the $I_{directivity}$ and T_p distributions see Chapter 4 of Shahi [2013].

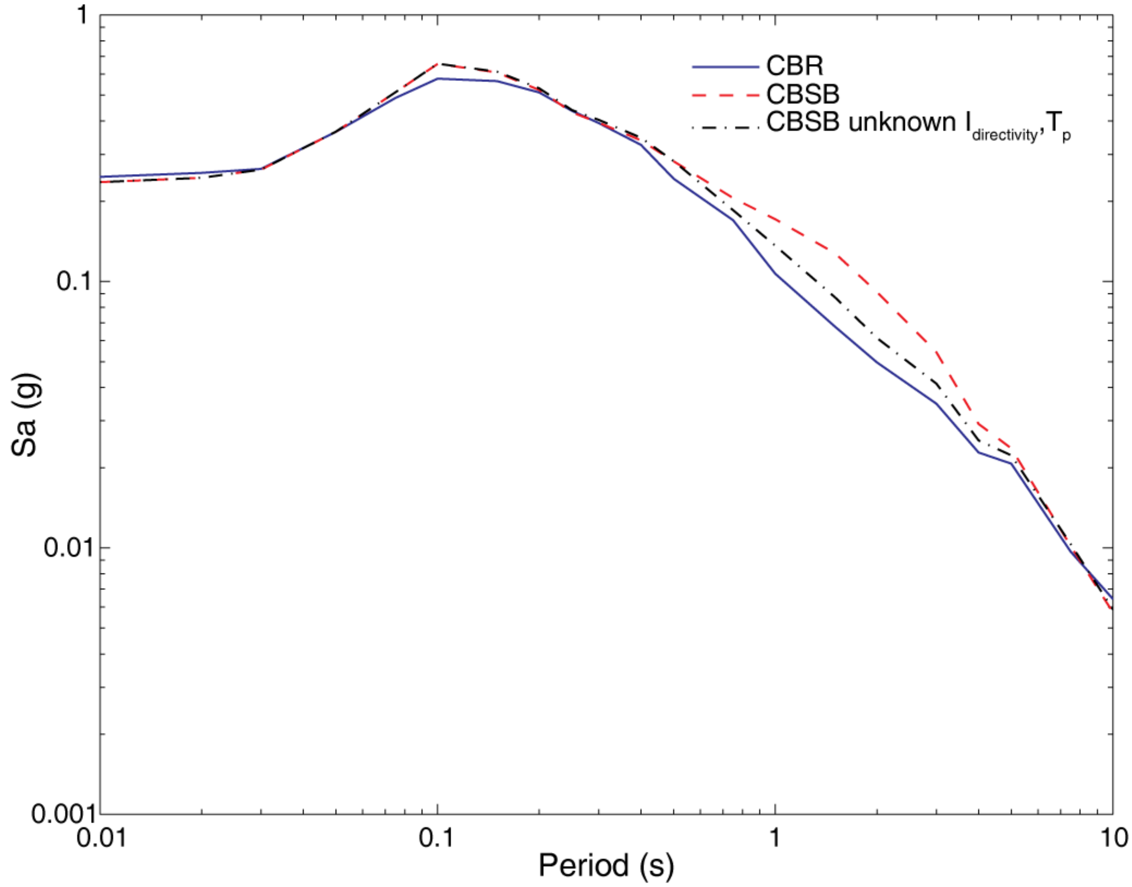

Figure 4.1 **Comparison of the median response spectra predicted by CBR model and the CBSB model for $M = 6.5$ and $R = 10km$ earthquake, when a directivity pulse of period 2.2 sec is assumed to have occurred and when pulse occurrence is considered uncertain. For the uncertain pulse case P(directivity) is picked to be 0.6 for the purpose of illustration, and the T_p follows the log-normal distribution.**

4.3.2 Deamplification

The CBR ground-motion model was fitted to provide prediction of ground motion under the absence of any information about directivity pulses (information like occurrence of a directivity pulse, period of the pulse, etc.). On the other hand, the CBSB model is fitted to provide prediction of ground-motion intensity when some information related to directivity pulses is known. Thus, if the CBSB model shows amplification with respect to the CBR model when a directivity pulse is observed (i.e., $I_{directivity} = 1$), it should predict deamplification with respect to the CBR model given the information that pulse is not observed. Figure 4.2 compares the median spectra predicted by CBSB with CBR for a strike-slip earthquake with magnitude 7.5 and distances or 1km or 20 km. The $I_{directivity}$ parameter in CBSB is set to 0, to get the prediction for the case when a directivity pulse is not observed at the site. As expected, the CBSB model predicts lower ground-motion intensities than the CBR model but the deamplification is stronger at 1 km than at 20 km. This result is expected as according to the model, the probability of observing directivity pulses is very low at 20 km. So, in the absence of any information about directivity pulses the CBR model predicts the intensity that is closer to the no-pulse prediction of CBSB model.

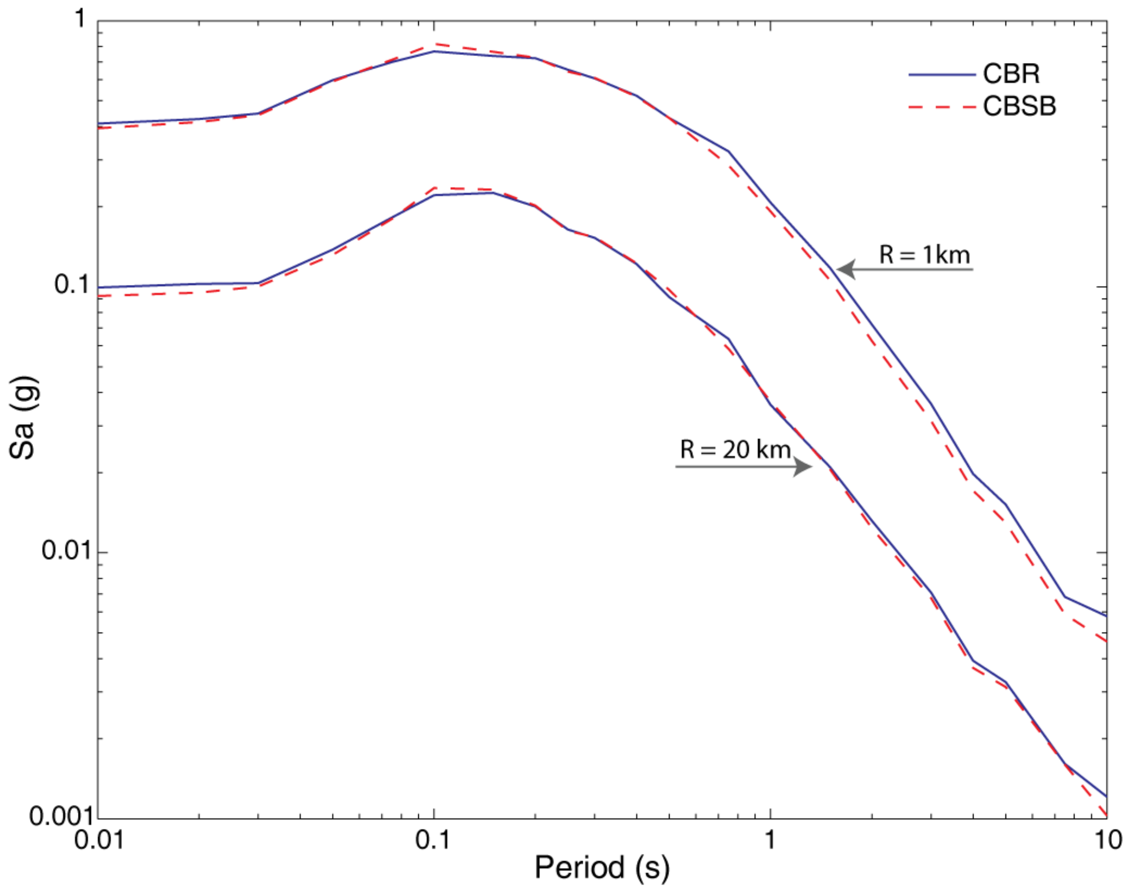

Figure 4.2 Comparison of the median response spectra predicted by CBR model and the CBSB model when $I_{directivity}$ is set to 0. The comparisons are for R_{rup} = 1 km and R_{rup} = 20 km. Comparison is shown for an earthquake with $M = 7.5$.

4.4 AVERAGE DIRECTIVITY AMPLIFICATION

The CBSB ground-motion model as presented in Equation (4.1) assumes the knowledge of directivity pulse occurrence (i.e., the value of $I_{directivity}$) and its period (T_p). When predicting the ground motion from a future earthquake, one does not know the value of these parameters. Though the values of $I_{directivity}$ and T_p are unknown, it is reasonable to assume some knowledge about the scenario of interest (e.g., M, R, and possibly hypocenter location). In this case, the expected value of $lnSa$ conditioned on available information can be used as a prediction for ground-motion intensity from a future earthquake. When location of the rupture and the hypocenter is known, taking expectation over $I_{directivity}$ and T_p gives the mean $lnSa$ given that information. Rupture location and hypocenter location are not known from future earthquake, so further expectation over possible rupture and hypocenter location may be needed. It is common in PSHA computations to take expectation over possible future fault rupture locations, however taking expectation over possible hypocenter locations is not as common. Taking expectation over possible hypocenter locations has been recommended in literature (e.g., Abrahamson [2000]), but it adds considerable computational overhead and is only required when accounting for directivity effects. Significant computational savings can be achieved by pre-computing the average directivity amplification ($lnAmp$) over possible source-to-site geometries. A model to predict average directivity amplification from random rupture and epicenter location is developed and proposed in Chapter 5 of Shahi [2013].

4.5 COMPARISON OF MODEL STANDARD DEVIATION

The standard deviation of total residuals (σ) of both CBSB and CBR models are similar to each other at low periods and there is a modest decrease in σ at high periods, when information about observation of pulse and its period is known. When the $I_{directivity}$ and T_p are unknown the CBSB model and CBR models have similar σ. The reduction in σ shows improvement in model prediction from incorporating new parameters. Directivity effects are most prominent at sites near the fault and at larger spectral acceleration periods. Thus, if the model improvement is a result of better accounting of directivity effects, the sigma reduction should be higher at sites close to the fault and at larger periods. This is confirmed by Figure 4.3, which shows model standard deviation as the function of R_{rup} at 0.2 and 2.0 second spectral acceleration periods.

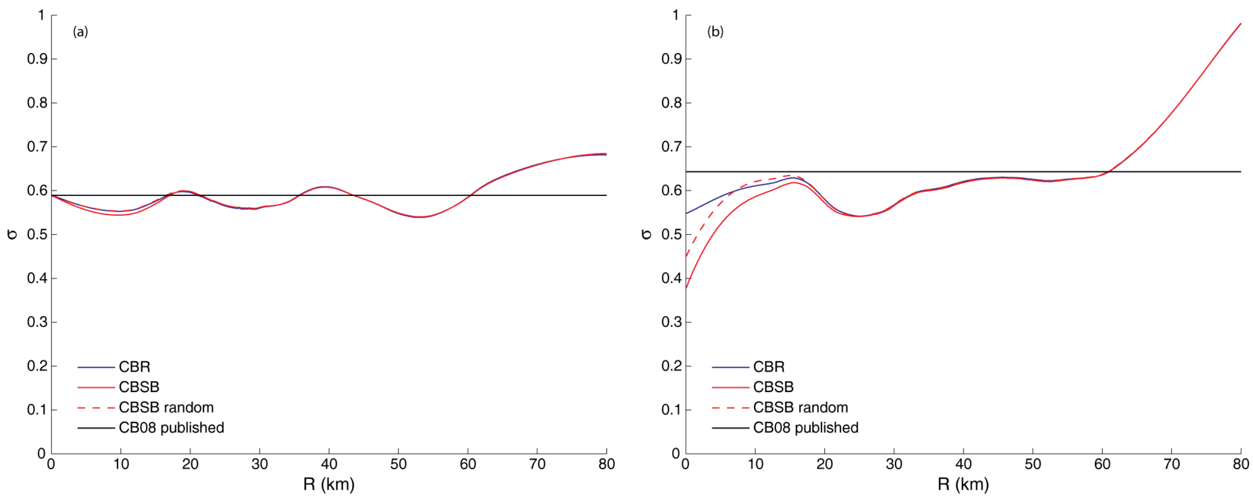

Figure 4.3 Comparison of σ of the residuals from CBR, CBSB, and CBSB with random/ unknown T_p and $I_{directivity}$ as a function of R_{rup} for a) T = 0.2sec and b) T = 2sec. Published value of σ from Campbell and Bozorgnia [2008] are also shown for comparison.

5 Spudich and Chiou Model

Paul Spudich and Brian S.J. Chiou

The directivity model discussed in this document was developed as part of the NGA-West2 project managed by the Pacific Earthquake Engineering Research Center (PEER) of the University of California, Berkeley. This model is an improvement over the Spudich and Chiou [2008] directivity model. It should not be confused with another directivity model developed by Chiou and Spudich [2012], which uses the IEP parameter.

5.1 MODEL FUNCTIONAL FORM

Our functional form for directivity effect is

$$\hat{f}_D(\mathbf{x}) = f_r(R, R_1, R_2\,)\; b(\boldsymbol{M}, T)\, \big(IDP(\mathbf{x})\; - \;\overline{IDP}(R)\big) \tag{5.1a}$$

where

$$b(\boldsymbol{M}, T) = \big(c_2 + c_3\; max(\boldsymbol{M} - c_1\,, 0)\big)\; exp[q(\boldsymbol{M}, T)] \tag{5.1b}$$

$$q(\boldsymbol{M}, T) \;=\; -[log_{10}T \;-\; (c_4 + c_5\boldsymbol{M})]^2/2g^2 \tag{5.1c}$$

M and *T* are moment-magnitude and oscillator period, respectively. *IDP* is the isochrone directivity parameter defined in Spudich and Chiou [2008]. Coefficients c_1, c_2, c_3, c_4, c_5, and g are period-independent constants to be determined from ground-motion data. f_r is a distance taper that linearly tapers to zero from rupture distance R_1 to R_2. **x** is the site location of interest on the Earth's surface. Scaling with *IDP* is modeled as a function of both period and magnitude. $\overline{IDP}(R)$ is the average value of the *IDP* over the footprint of constant R, and R could be R_{rup} or R_{jb} These terms are described in more detail below.

5.2 CALCULATION OF THE IDP

IDP is the isochrone directivity parameter, calculated as described in Spudich and Chiou [2008] (with the modified calculation described in Appendix D, Section D.1 of this report), which includes the application to multi-segment ruptures (where by "multi-segment" we mean a rupture surface consisting of two or more contiguous planar quadrilaterals joined along their down-dip edges, sharing a single hypocenter). Two aspects of the calculation of the *IDP* not described explicitly in SC2008 are:

5.2.1 Multi-Fault Ruptures

Selection of *IDP* for the case of multi-strand (or multi-fault) ruptures, by which we mean ruptures that occur on two or more non-contiguous surfaces (which might each be multi-segment), with each surface having its own hypocenter: If there are $i = 1, \ldots, n$ multi-segment ruptures, each having at a specific site the value *IDP* of isochrone directivity parameter, the chosen *IDP* is the maximum over all strands, i.e.,

$$IDP = \max_i(IDP_i), \ i = 1, \ldots, n \tag{5.4}$$

5.2.2 Calculation of D

Calculation of the distance D along the fault surface from the hypocenter to the closest point. SC2008 say that any reasonable algorithm is acceptable, but in Appendix D, Section D.1, we specifically present the algorithm that we use.

5.3 NARROW-BAND ISOCHRONE DIRECTIVITY EFFECT

Equation (5.1) is a "narrow-band" model in which the period-dependent directivity effect peaks at a period that increases with earthquake magnitude. Motivation and justifications of this narrow-band model are described in Appendix F.

5.4 AVERAGE IDP AND USE WITH GMPES

To properly use our directivity model with GMPEs, it is crucial to understand this section. Formally, the average *IDP* is defined by

$$\overline{IDP_q}(R) = \oint_{\Gamma_q(R)} IDP_q(\mathbf{x}) dl / L(R) \tag{5.5}$$

where

- **x** is a point on the Earth's surface within the "footprint" of the directivity function (i.e., within the 70-km R_{rup} contour) around the *q-th* earthquake,
- $IDP_q(\mathbf{x})$ is the IDP at **x** for the *q-th* earthquake,
- $\Gamma_q(R)$ is the contour ("racetrack") of constant R around the *q-th* earthquake (i.e., it could be the 30-km R_{rup} contour around the Chi-Chi earthquake),

- $L(R)$ $(= \oint_{\Gamma_q(R)} dl)$ is the length of $\Gamma_q(R)$.

When R is R_{jb} and $R_{jb} = 0$, the above definition is slightly modified to take into account the finite areas where $R_{jb} = 0$

$$\overline{IDP_q}\left(R_{jb} = 0\right) = \iint_{a_q} IDP_q(\mathbf{x})\ dA \Big/ \iint_{a_q} \quad dA \tag{5.6}$$

where a_q is the finite area where $R_{jb} = 0$.

For practical calculation, we use a simpler algorithm. We sample $IDP_q(\mathbf{x})$ over points having distance within some interval $\pm dR$ around the target distance and we take the average of sampled values as $\overline{IDP_q}(R)$.

In common parlance, $\overline{IDP_q}(R)$ is the average value of *IDP* on the contour ("racetrack") of constant R around the *q-th* earthquake. It should be noted that $\overline{IDP_q}(R)$ contains the general trend of *IDP* with *R*. We call $\left(IDP(\mathbf{x}) - \overline{IDP}(R)\right)$ a "centered" *IDP* and Equation (5.1) a "centered" model.

Equation (5.1) models how ground motions along the racetrack deviate from their median value (achieved at **x** where $IDP(\mathbf{x}) = \overline{IDP}(R)$). One practical advantage of a "centered" model is that the user can easily deactivate directivity scaling by setting $IDP_q(\mathbf{x}) = \overline{IDP_q}(R)$, and the resulting GMPE still has the useful interpretation of being the median motion over the racetrack. It is important to realize that GMPEs lacking a specific directivity term still fit directivity amplification in the data, but only the part of the directivity amplification that is a function of R.

GMPE developers using the NGA-West 2 database need not use the equations above to calculate $\overline{IDP_q}(R)$; instead they may use the simple parametric equation given in Appendix E to obtain $\overline{IDP_q}(R)$, which we developed to simplify the calculation.

5.5 DISTANCE TAPER

$f_r(R, R_1, R_2)$ is a distance taper. $f_r = 1$ for $R_{rup} \leq R_1 =$ 40 km, f_r tapers linearly from a value of unity at $R_1 = 40$ km to zero at $R_2 = 70$ km, and $f_r = 0$ for $R_{rup} > 70$ km. This functional form is taken from SC2008. In reality, directivity is observed in long-period ground-motions at teleseismic distances, so it is clear that the taper distances should be a function of period, i.e., they should extend farther from the causative fault at longer periods. Our choice of taper distances is very simplistic. We have evidence that the directivity effect can be seen at different distances for steeply and shallowly dipping faults, and there is some directivity in the NGA-West 2 data set at distances about 100 km. For very large earthquakes the distance taper truncates the distance at which directivity has an effect. Users should bear in mind that directivity can be seen in some cases beyond 70 km.

5.6 SUMMARY OF EMPIRICAL COEFFICIENTS

Constants c_1, c_2, c_3, c_4, c_5, and g are period-independent constants, to be derived by the GMPE developers. NGA developers requested that we provide some estimates of these constants as guides to starting values that can be further refined by GMPE developers. In this document we present these constants from two analyses of within-event residuals: (1) Model 3: a model we derived from a formal regression of the residual data, and (2) the *ad hoc* model, which we derived from inspection of the residuals. We computed residuals with respect to an interim model received from Abrahamson and Silva [personal communication 2011] for the Nov-2011 NGA-2 data at distances less than 50 km for T=0.5, 0.75, 1.0, 1.5, 2.0, 3.0, 4.0, 5.0, 7.5, 10.0 sec.

Thirty-six earthquakes in NGA-2 database have a finite fault model and produce at least 5 recordings. Among them, 21 earthquakes exhibit good azimuthal coverage and apparent directivity; this subset of 21 good earthquakes is used in this analysis. See Appendix C for more details. Table 5.1 shows the obtained coefficients and Table 5.2 shows the sigma reduction.

Table 5.1 Preliminary coefficients of Spudich and Chiou directivity models.

Param.	Comments	*Ad hoc* Model	Model 3 (Preferred)
a	Reference *IDP*; to be modified in NGA models by developers	-	1.4996
c_1	Transition **M** from a constant b to a **M**-dependent b	6.2	5.7
c_2	b_{max} of small **M** (**M** < c_1))	0.2785	0.0823
c_3	**M**-scaling of b_{max}	0.1655	0.1665
c_4	Intercept of $\log_{10}(T_{max})$	-3.1884	-1.1736
c_5	M-scaling of $\log_{10}(T_{max})$	0.5479	0.2971
g	Bandwidth	0.4	0.6132
LL	Log likelihood	-	-6600

Table 5.2 Sigma reduction of Model 3.

T(sec)	Data (Residual) σ_o	Residual of Model 3, σ_1	Sigma Reduction, $\sqrt{\sigma_o^2 - \sigma_1^2}$
0.5	0.5540	0.5533	0.0278
0.75	0.5713	0.5670	0.0700
1	0.5666	0.5557	0.1103
1.5	0.5529	0.5374	0.1298
2	0.5824	0.5590	0.1634
3	0.6074	0.5721	0.2038
4	0.6129	0.5787	0.2019
5	0.6307	0.5903	0.2220
7.5	0.6594	0.6050	0.2623
10	0.6615	0.5800	0.3182

5.7 COMMENTS ON THE USE OF THIS DIRECTIVITY MODEL

Subject to all the uncertainties in Section 5.7.1, our directivity model is appropriate for earthquakes in the magnitude range 5.75 – 7.9, for periods from 0.5 to 10 sec, and for rupture distances out to 70 km. It may be applied to earthquakes rupturing complicated fault geometries with bends up to about 90°. It may be used for quakes having any dip and rake, although it works best for vertical strike-slip faults. Dip may vary over the rupture surfaces, but the rake is assumed to be constant. Embedded in the method is the assumption that the ratio of rupture speed to shear wave speed is 0.8. The theory easily allows other ratios to be used, and the method probably gives reasonable results for ratios less than 0.95, but Spudich and Chiou [2008] found that the results were insensitive to the range of rupture speed ratios in the NGA data set at the time and recommended that 0.8 be used.

5.7.1 Limitations of the Model

Our directivity model has several weaknesses.

While it predicts identical directivity from a normal faulting rupture (rake = -90) and a reverse rupture (rake=90), both having the same hypocenter and rupture speed, there is considerable theoretical evidence that reverse ruptures breaking the surface have greater ground motions than normal ruptures [Oglesby et al. 2000]. It is not clear whether this difference varies with distance and azimuth and should be modeled in the directivity model or is already accounted for in the underlying GMPE as the style of faulting effects.

Because of our use of the closest point, which can change discontinuously as the site is moved, maps of predicted directivity show step discontinuities (see maps of Chi-Chi directivity in Figure 1.13). If a multi-segment or multi-fault rupture is being simulated, the user should make a map of the directivity in some sufficiently large area around the target site in order to determine whether the target site is near a discontinuity of predicted directivity. As these discontinuities in directivity are not expected in reality, the user should enlarge (in some sensible way) the predicted sigma with the additional variation in directivity experience in the near-site area.

The user should check that his or her target site is not near a negative singularity in IDP. The S factor of IDP is $S = ln\left(min\big(75, max(s,h)\big)\right)$. For any site on a vertical plane containing the hypocenter ($s = 0$) when the hypocenter is very close to the upper edge of the fault ($h = 0$), S can have a negative singularity. Such a problem occurs for the Whittier Narrows earthquake (see Figure 5.1). We tentatively recommend requiring $s \geq 1\ and\ h \geq 1$, although we have not checked all the consequences of this recommendation.

Our directivity model is still somewhat unsatisfying for magnitudes less than about 5.75. First, as mentioned in Appendix F, Section F.5, coefficients c_1 and c_2 are subject to large epistemic uncertainty. In order to reduce epistemic uncertainty, directivity data from earthquakes as small as M 4.5 are needed. Our directivity model has not been calibrated for earthquakes with magnitudes less than 5.75. The NGA-West2 dataset has data from earthquakes having magnitudes of 5.61 and 5.74, but they do not conform well to our model. Our model is clearly incomplete for earthquakes below M 5 because, in addition to having no data, our functional form omits some observations. We know from Seekins and Boatwright [2010] that clear directivity in PGA can be seen for some small earthquakes, but our model does not predict this. We do not yet know, if directivity effect in small earthquakes is pervasive, how to modify our functional form to solve this problem.

Our taper of the directivity from 40 to 70 km is a considerable simplification of the data. It is taken unchanged from Spudich and Chiou [2008], who in unpublished notes found that their predicted directivity for vertical faults provided the best data fit in the 0-40 km distance range, whereas for dipping faults the best data fit was in the 40-60 km distance range. Because the data beyond 70 km were very incomplete, it was decided to taper from 40 to 70 km. However, we know that at long periods directivity can be seen at teleseismic distance, so the taper distance should be a function of period, but our model does not include this behavior.

Users should read Spudich and Chiou [2008] to learn about limitations to the complexity of fault geometry caused by the behavior of their generalized coordinate system, which we call GC1. A new generalized coordinate system, GC2, is being developed [Spudich and Chiou 2013, in preparation] which may be substituted for GC1.

5.7.2 Use of a Narrow-Band Model for Non-Pulse Motions

It might seem strange that our model uses a narrow-band functional form, originally developed to model the amplification of response spectra by a pulse in the velocity time series. Any model that uses a Gaussian function of period has the potential to suppress directivity effects from small quakes at long periods and from big quakes at short periods, if the Gaussian is narrow enough. We believe that our use of a narrow-band model is reasonable for several reasons. First, looking at the data in Figure E.5 in Appendix E, few earthquakes have a significant $b(T)$ over a broad range of T, so there is not a compelling reason to use a broad-band model. Second, as the dataset contains a mixture of impulsive and non-impulsive ground motions, it should be expected that the data set on the whole would have some narrow-band characteristics, but the bandwidth would be larger than for a pure pulse model. And, in fact, our ad hoc model has a rather narrow bandwidth, 0.4, but when the larger data set is fitted, the resulting bandwidth is 0.61. If such a Gaussian is peaked at 3 s, its amplitude at 1 and 10 s is about 70% of its peak amplitude, and its amplitude at 0.3 and 30 s is about 25% of its peak amplitude, so our narrow-band model is not very narrow-band. However, it is not a monotonically increasing function of period.

We have not compared the reduction in data residual between our narrow band Model 3 and a broad-band model. The project plan calls for the GMPE developers to select a directivity predictor and include a directivity term in their equation. When this is done, it is likely that the coefficients of magnitude-dependent and distance-dependent terms in the GMPE will change considerably. Consequently, the "residuals" to be fit by directivity at that stage will be rather different from the preliminary residuals available to us now. For this reason it is more appropriate to compare the residual reduction of the competing models when the perturbation to the GMPEs is also being included.

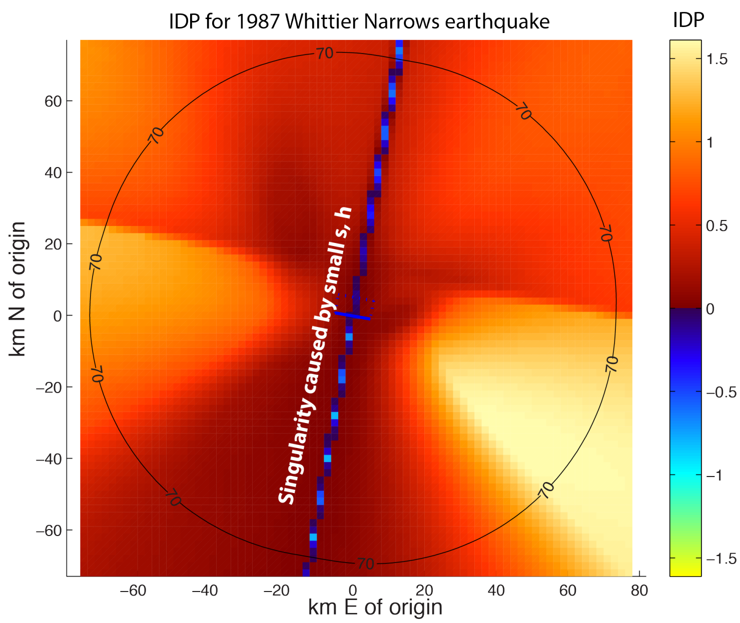

Figure 5.1 **Example of negative singularity of *IDP* for the 1987 Whittier Narrows, California, earthquake.**

6 The Chiou and Spudich NGA-West2 Directivity Predictor DPP

Brian S.J. Chiou and Paul Spudich

6.1 BEYOND THE *IDP*

We have developed a new directivity predictor, the Direct Point Parameter (*DPP*, formerly known as the *IEP*, (no acronym)) to remedy the following flaws in the directivity predictor *IDP* of Spudich and Chiou [2008] (See Appendix G for the definition of the IDP and related quantities.):

- Maps of the *IDP* around simple rectangular ruptures sometimes have streaks of non-intuitive high and low directivity that are the result of similar behavior in the isochrone velocity ratio $\tilde{c}'$ (Figure 6.1).
- For multi-segment or multi-fault ruptures the *IDP* can be spatially discontinuous (Spudich and Chiou [2013], this volume; Figure 6.2), which could be traced to the dependence of $\tilde{c}'$ and the radiation pattern on the "closest point," the point on a fault closest to a given target site where the *IDP* was to be calculated. For multi-segment ruptures, moving the target site by 1 m can cause the closest point to jump discontinuously from one fault segment to another. This jump does not introduce a discontinuity into the rupture distance or the Joyner-Boore distance, but it does introduce a discontinuity into the isochrone velocity ratio $\tilde{c}'$ and hence into the *IDP*.
- The radiation pattern used for the *IDP* of the finite source is approximated by a point source radiation pattern modified by a coordinate transform.
- The calculations of the radiation pattern and the coordinate transforms are cumbersome when calculating the *IDP*.

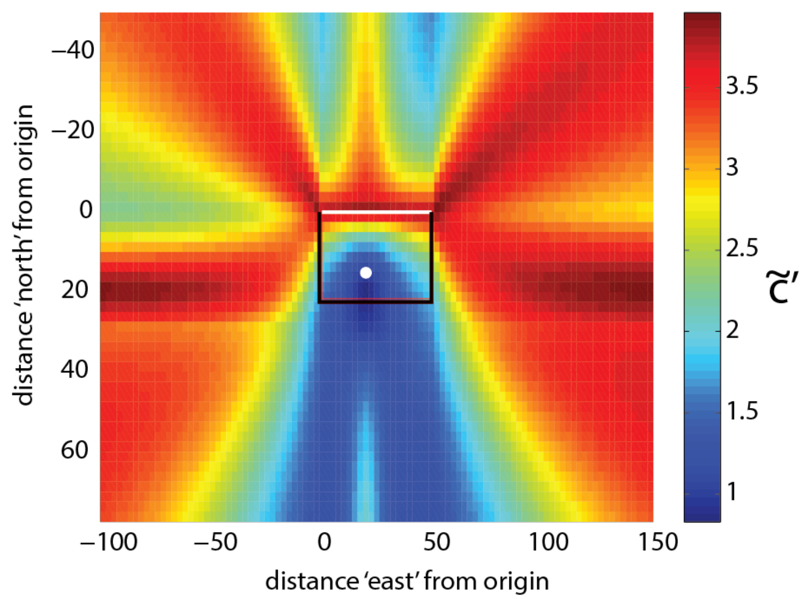

Figure 6.1 Map of the isochrone velocity ratio $\tilde{c}'$ around a dipping fault. White dot is hypocenter, white line is fault trace, black rectangle shows extent of rupture down-dip.

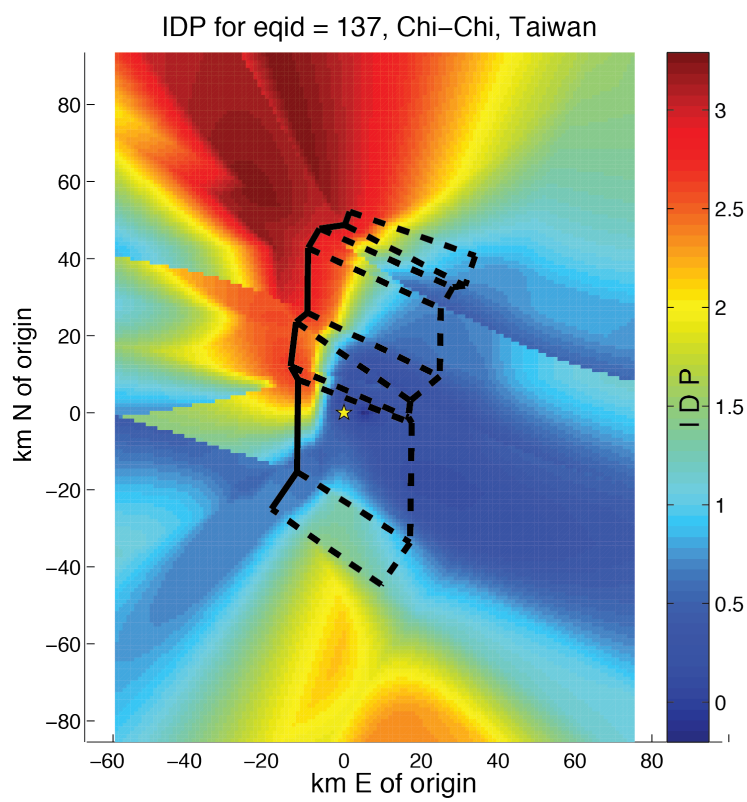

Figure 6.2 Map of IDP (colors) around Chi-Chi, Taiwan, rupture. Solid black line is surface trace of the fault segments, dashed lines show vertical projection of the buried fault segments. Yellow star is hypocenter. Discontinuities in IDP such as that seen near -40 km E, 40 km N, are caused by the closest point jumping from segment to segment.

Moreover, $\tilde{c}'$ uses the closest point primarily because the closest point is routinely calculated for GMPE evaluation, not because of that point's primacy in directivity. This can be seen in Figure 6.3, which shows in colors the actual isochrone velocity c as a function of position on a 25 by 50 km dipping fault for a site located 75 km north of the fault trace. Note that the section of the fault having high isochrone velocity, strong directivity (shown in warm colors), points directly toward the site, but that the closest point to the site is nowhere near this strong directivity zone. Consequently, the isochrone velocity ratio $\tilde{c}'$, which is a two-point approximation of the isochrone velocity based on the hypocenter and the closest point, is a poor approximation of the directivity in this case. Also indicated on Figure 6.3 is the "direct point," which we will define later. Our use of the direct point instead of the closest point to define an approximate isochrone velocity distinguishes the *DPP* (Direct Point Parameter) model of directivity from the *IDP*.

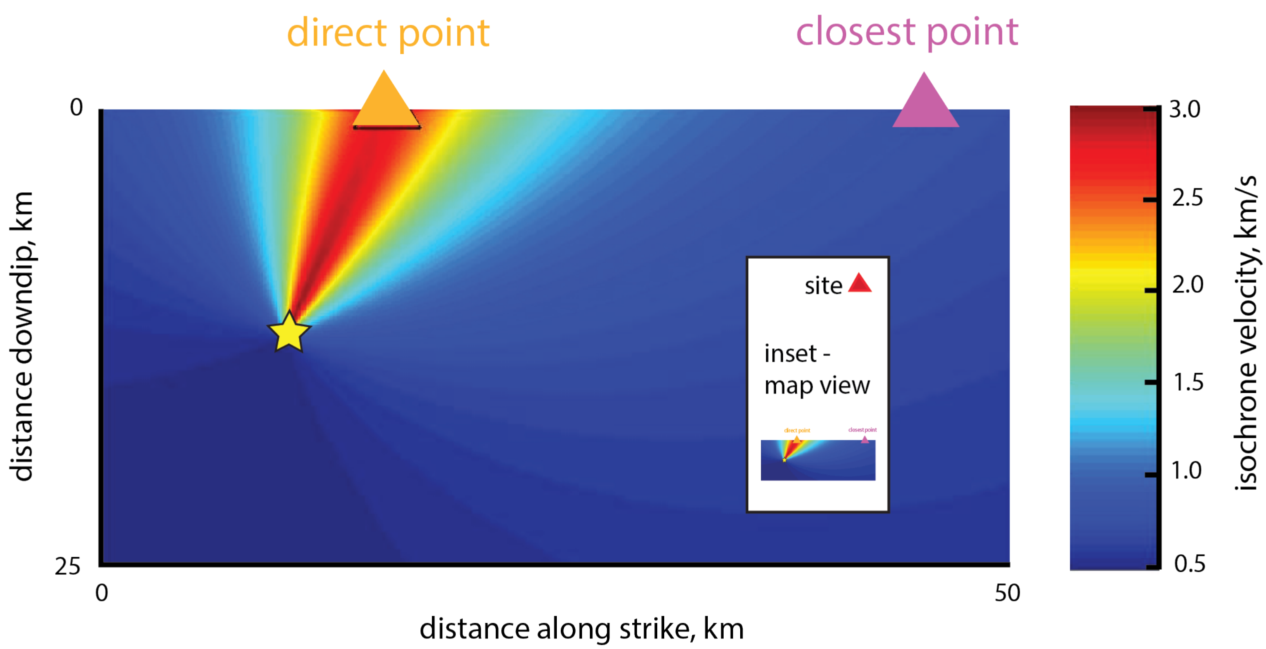

Figure 6.3 **Isochrone velocity on the fault plane of a 30° dipping fault. Inset shows relative location of site 75 km north of fault. Direct point and closest point on the fault to the site are indicated. Yellow star is hypocenter.**

6.2 DIRECT POINT AND E-PATH

The direct point P_D (Figure 6.4) is the intersecting point of the fault-projected direct ray $\overrightarrow{P_H P_P}$ with the slipped-area boundary Γ, where P_H is the hypocenter and P_P is the projection of the site onto the plane containing the slipped area. When a site is normal to the slipped area (i.e., P_P is inside Γ), its direct point is P_p.

Line segment $P_H P_D$, which we call the "E-path," has length E. In the context of the isochrone method of ground-motion simulation [Spudich and Frazier 1984], the part of the fault traversed by the E-path is closely associated with the highest isochrone velocity on the fault (such as the example in Figure 6.3) and hence the determining factor of directivity pulse at a specific site.

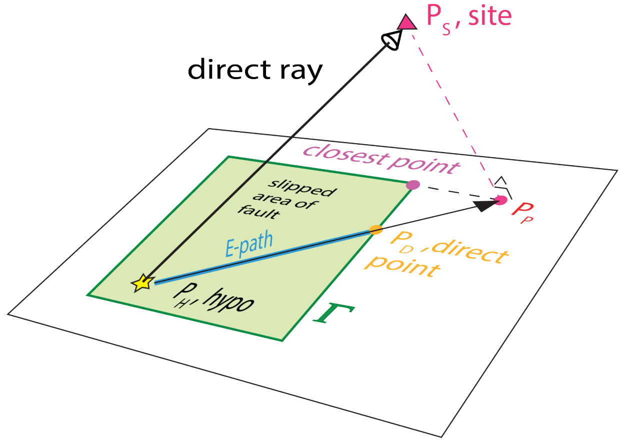

Figure 6.4 **Geometry of direct point and E-path: P_H : hypocenter; P_S : site of interest; P_P : perpendicular projection of P_S onto the fault plane; Γ : boundary of slipped area; P_D : direct point. The fault-projected direct ray $\overrightarrow{P_H P_P}$ is the projection of $\overrightarrow{P_H P_S}$ onto the plane containing the slipped area.**

Using this geometry, we define a new approximate isochrone velocity ratio $\hat{c}'$ analogous to the old $\tilde{c}'$. $\hat{c}'$ (called "c-hat-prime") is identical in form to the old isochrone velocity ratio $\tilde{c}'$ of Spudich and Chiou [2008] except that $\hat{c}'$is based on the direct point (see Appendix G for more details),

$$\hat{c}' = \frac{1}{\left(\frac{1}{0.8} - \frac{R_{HYP} - R_D}{E}\right)}, \quad E > 0;$$

$$\hat{c}' = 0.8, \quad E = 0.$$

where R_{HYP} is the hypocenter distance (line segment $P_S P_H$) and R_D is the distance to direct point (line segment $P_S P_D$). As noted earlier, a map of $\hat{c}'$ (Figure 6.5) shows it to be much more smooth spatially than $\tilde{c}'$ (Figure 6.1). Rowshandel [personal communication] has noted, "Besides and in addition to the smoothness, the distribution of the new parameter (DPP), shown in Figure 6.5, is seen to be more sensible than that of IDP shown in Figure 6.1. In particular, comparing Figures 6.1 and 6.5, it is observed that the zones of high IDP, directly above the hypocenter, and also on both sides of the fault going in the horizontal direction from the hypocenter have disappeared (in Figure 6.1). Instead, zones of high directivity, corresponding to large DPP values are now in the zones beyond the top corners of the fault, where the lengths of rupture are about the maximum. This feature is expected to bring the Chiou and Spudich results more in agreement with the predictions from Rowshandel model. Inspecting Figures 1.8 through 1.10, accounting for the features of DPP in Figure 6.5 (and including the distance taper) will demonstrate this further."

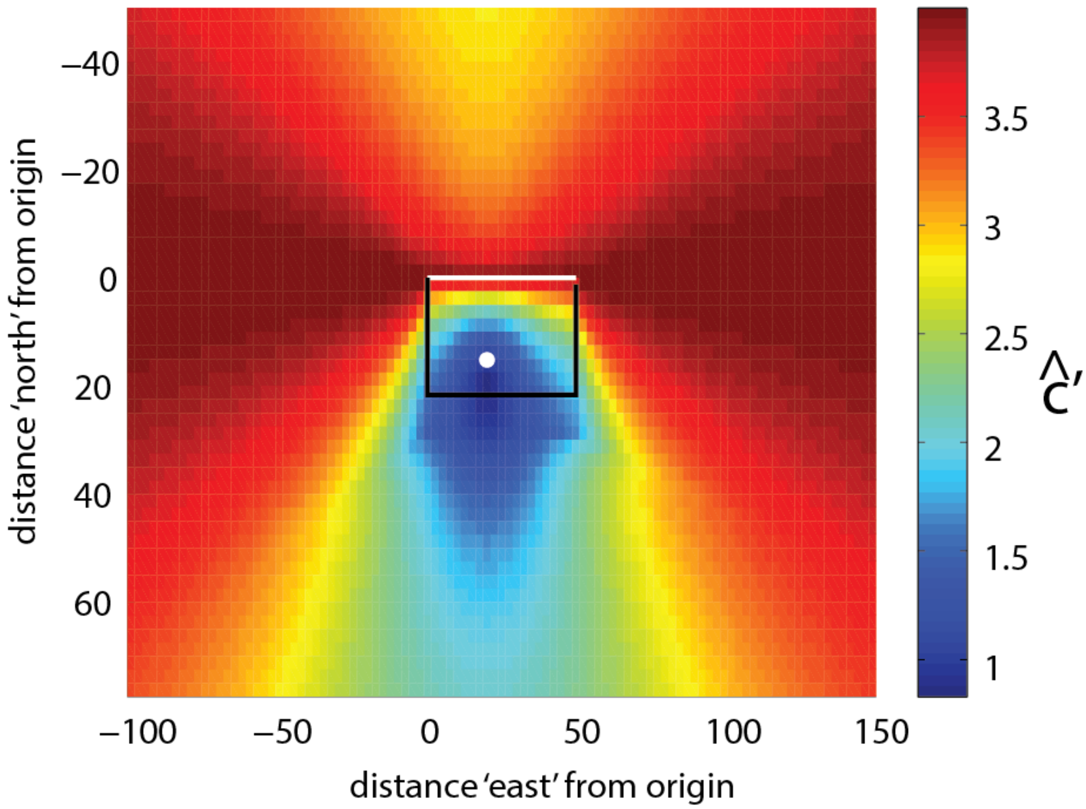

Figure 6.5 Map of $\hat{c}'$ for the same geometry as Figure 6.1. Note greater smoothness in $\hat{c}'$ as compared to $\tilde{c}'$ shown in Figure 6.1.

6.3 DEFINITION OF PREDICTOR *DPP*

Our proposed isochrone directivity predictor *DPP* has three factors analogous to the three factors comprising the *IDP* (see Appendix G): a measure of isochrone velocity; a measure of rupture propagation distance; and a radiation pattern term. *DPP* for a single planar rupture surface is the logarithm of a product of three terms constructed from the E-path,

$$DPP = \ln\left(\hat{c}' \cdot \max\left(E,\ 0.1f\right) \cdot \max\left(\overline{FS},\ 0.2\right)\right) \tag{6.1}$$

where:

- $\hat{c}'$ is the isochrone velocity ratio, as previously discussed;
- E (=$P_H P_D$) is the length of E-path in km. We set a floor of $0.1f$ on E, where f is the larger of fault length and fault width; and
- $\overline{FS}$ is the average S-wave radiation pattern over E-path. As in Spudich and Chiou [2008), we put a floor of 0.2 on $\overline{FS}$ filling the radiation nodes. A simple expression for $\overline{FS}$ is provided in Equation (6.11).

The *DPP* might appear to be larger than the *IDP*, but it will have smaller coefficients when regressed against data, preserving the total directivity in the data. It can be used to form a narrow-band directivity model exactly analogously to the *IDP* [Spudich and Chiou 2013].

Section 6.6 describes an extension of *DPP* for use with multi-segment ruptures and multi-fault ruptures.

As in Spudich and Chiou [2008], we recommend that the hypocenter not be placed on or near the edge of the slipped area. For NGA-West2 earthquakes, if the hypocenter is less than 10% of fault length (or fault width) from an edge, we move the hypocenter perpendicularly to the 10% location for the purpose of calculating *DPP*. This location is a reasonable placement of hypocenter based on the work of Mai and others [2005].

6.4 EXPRESSION FOR POINT-SOURCE RADIATION PATTERN

The *IDP* uses the formulae given in Appendix A of Spudich and Chiou [2008] to calculate the magnitude of the point double-couple radiation pattern of the S wave. For the purpose of computing scalar radiation pattern, we now favor using Aki and Richard [1980] Equation (4.33) because it has a simpler and more compact expression than that of Spudich and Chiou [2008] and gives exactly the same result for the magnitude of the point-source radiation pattern. Furthermore, it is based on the same geometry as that used for constructing the direct point. However, unlike the Spudich and Chiou [2008] equations, the expression of Aki and Richard [1980] does not yield the fault-normal and fault-parallel components of motion (which is why it is simpler). We illustrate in Figure 6.6 the common geometry used for calculating both direct point and point-source radiation pattern. Unit vectors $\vec{n}$, $\vec{u}$, and $\vec{x}$ are in the directions of fault perpendicular, fault slip, and projected direct ray ($\overrightarrow{P_H P_P}$), respectively. Note that vector $\vec{u}$ here differs from vector $\vec{u}$ in Spudich and Chiou [2008, 2013].

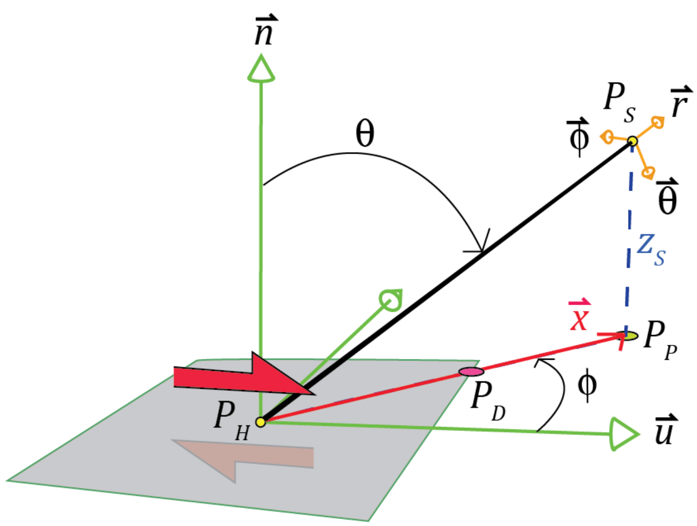

Figure 6.6 Cartesian and spherical polar coordinates for calculation of radiation pattern.

From Aki and Richards [1980, p. 81], the far-field S-wave radiation pattern (A^{FS}) of a point source is

$$A^{FS} = \vec{\theta}\ \cos 2\theta\ \cos\phi\ - \vec{\phi}\ \cos\theta\ \sin\phi \tag{6.2}$$

with angle ϕ is measured counterclockwise from $\vec{u}$ to $\vec{x}$, and angle θ is clockwise from $\vec{n}$ to $\overrightarrow{P_H P_S}$. Angle ϕ and vector $\vec{\phi}$ are invariant with location for a source anywhere on the E-path, while angle θ and $\vec{\theta}$ vary with location. For a specific point on E-path,

$$\vec{\theta} = \vec{x}\cos\theta - \vec{n}\sin\theta \tag{6.3}$$

$$\cos\theta = \frac{z_S}{\sqrt{z_S^2 + (l_2 - l)^2}} \tag{6.4}$$

where l is the distance from the hypocenter to a source point location on the E-path, l_2 is the fixed distance between P_H and P_P, and z_s is the signed distance between P_S and P_P (Figure 6.7).

6.5 MAGNITUDE OF THE LINE-SOURCE RADIATION PATTERN

In modeling the effect of radiation pattern on a directivity pulse, unlike Spudich and Chiou [2008] we do not use a single point-source radiation pattern, warped by their Generalized Coordinate Transform, for long ruptures. Conceptually following Watson-Lamprey [unpublished notes Sept. 2012], the radiation pattern averaged over the E-path is an improvement over a single point source radiation. The simplicity of Equation (6.2) allows us to derive such average analytically, as described below.

The magnitude of S-wave average radiation pattern over the E-path is

$$\overline{FS} = \left| \int_0^E A^{FS}\, dl \right| / E \tag{6.5}$$

From Equations (6.2) and (6.3), we have

$$\int_0^E A^{FS} dl = \vec{x}\ \cos\phi \int_0^E \cos\theta\cos 2\theta\ dl - \vec{n}\ \cos\phi \int_0^E \sin\theta\cos 2\theta\ dl - \vec{\phi}\sin\phi \int_0^E \cos\theta\ dl \tag{6.6}$$

Plugging in Equation (6.4) and evaluating the three integrals in Equation (6.6), we obtain

$$\begin{aligned} I_x &= \cos\phi \int_0^E \cos\theta\cos 2\theta\ dl \\ &= \cos\phi \cdot \left[-2z_S \frac{l_2 - l}{\sqrt{z_S^2 + (l_2 - l)^2}} + z_S \ln\left((l_2 - l) + \sqrt{z_S^2 + (l_2 - l)^2} \right) \right] \Bigg|_{l=0}^{l=E} \\ &= \cos\phi \cdot \left\{ 2z_S \left(\frac{l_2}{R_{Hyp}} - \frac{l_2 - E}{R_D} \right) - z_S \ln \frac{l_2 + R_{Hyp}}{l_2 - E + R_D} \right\} \end{aligned} \tag{6.7}$$

$$I_n = \cos\phi \int_0^E \sin\theta \cos 2\theta \; dl$$

$$= \cos\phi \cdot \left[\frac{2z_S^2}{\sqrt{z_S^2 + (l_2 - l)^2}} + \sqrt{z_S^2 + (l_2 - l)^2} \right] \Bigg|_{l=0}^{l=E}$$

$$= \cos\phi \cdot \left\{ -2z_S^2 \left(\frac{1}{R_{Hyp}} - \frac{1}{R_D} \right) - (R_{Hyp} - R_D) \right\} \tag{6.8}$$

$$I_\phi = \sin\phi \int_0^E \cos\theta \; dl$$

$$= \sin\phi \cdot \left[-z_S \ln\left((l_2 - l) + \sqrt{z_s^2 + (l_2 - l)^2} \right) \right] \Bigg|_{l=0}^{l=E}$$

$$= \sin\phi \cdot \left\{ z_S \ln \frac{l_2 + R_{Hyp}}{l_2 - E + R_D} \right\} \tag{6.9}$$

Note that since $R_D = \sqrt{(l_2 - E)^2 + z_S^2}$ and $R_{Hyp} = \sqrt{l_2^2 + z_S^2}$, only four variables are needed to evaluate the integrals. They are: z_S, l_2, E, and ϕ. The first three variables are easily obtained from the locations of the four points shown in Figures 6.6 and 6.7. Variable z_S, the $\vec{n}$-coordinate of P_S, is positive when P_S is above the fault plane. Angle ϕ can be obtained with the additional information of slip direction $\vec{u}$ (or rake angle). We have

$$\int_0^E A^{FS} dl = \vec{x} \; I_x - \vec{n} \; I_n - \vec{\phi} \; I_\phi \tag{6.10}$$

and the average scalar radiation pattern is

$$\overline{FS} = \sqrt{I_x^2 + I_n^2 + I_\phi^2} \; / \, E \tag{6.11}$$

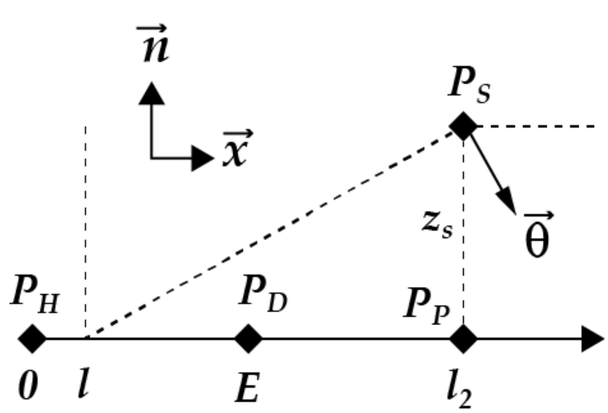

Figure 6.7 Definition of points and other quantities used by the radiation term.

6.6 MULTI-SEGMENT AND MULTI-FAULT RUPTURES

DPP described above is for a single rupture surface with only one segment. In reality, ruptures occur on multi-segment faults or on multiple faults. A multi-segment rupture is a rupture surface consisting of two or more contiguous planar quadrilaterals joined along their dipping edges, sharing a single hypocenter. A multi-fault rupture implies a rupture that occurs on two or more non-contiguous surfaces (which could each be multi-segment) with each surface having its own hypocenter. In this section, we describe how to compute *DPP* for multi-segment and multi-fault ruptures.

The simplest way to compute *DPP* for multi-segment rupture is to sum the products of individual segments, beginning with the segment containing the hypocenter, and working through subsequent segments toward the site. The summation ends at the segment where the direct point fails to be on the down-dip edge joining the next segment. Suppose the hypocenter segment number and the ending segment number are *iH* and *iD*, respectively,

$$DPP = \ln\left(\sum_{i=iH}^{i=iD} \hat{c}_i' \cdot \max\left(E_i,\ 0.1 f_i\right) \cdot \max\left(\overline{FS}_i,\ 0.2\right)\right) \tag{6.12}$$

where, $\hat{c}_i'$, E_i, $\overline{FS}_i$ are the isochrone velocity ratio, the length of the E-path, and the magnitude of the S-wave average radiation pattern of the i-th segment. For $i \neq iH$, a reasonable choice of segment "hypocenter" is the direct point of the previous segment. The full effect of the new formalism on the multi-segment Chi-Chi earthquake is seen by comparing Figure 6.2 with Figure 6.8. The map of directivity amplification in this figure compares well with Rowshandel's result for Chi-Chi (see Appendix C), indicating that the DPP formalism produces a result more in agreement with Rowshandel's result.

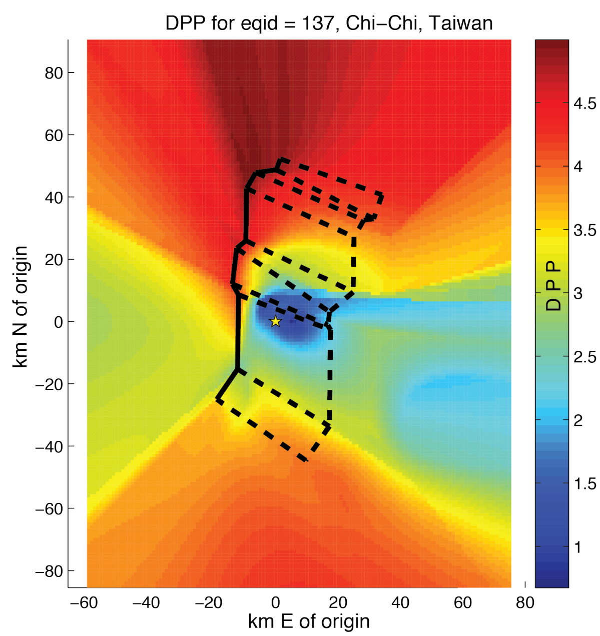

Figure 6.8 DPP map for Chi-Chi, Taiwan, earthquake. DPP is smoother than IDP (Figure 6.1).

In the case of multi-fault rupture, suppose there are n faults, each having, at a specific site, the value DPP_i of direct point parameter, the chosen DPP is the maximum over all faults (strands), i.e., $DPP = \max_i(DPP_i)$, $i = 1, \ldots, n$.

6.7 SUMMARY

- The *DPP* has a stronger theoretical underpinning than the *IDP* has:
  - It is based on the direct point, which is more closely correlated with directivity than the IDP closest point.
  - It includes the radiation pattern of a finite source (a line source rather than a point source).
- The DPP is simpler to calculate than the IDP:
  - The radiation pattern formulae are easier to calculate.
  - It uses a simpler algorithm for handling multi-segment and multi-fault ruptures.
  - No generalized coordinates are needed for non-planar faults.
- The DPP has smoother spatial variations than that of the IDP:
  - It is not dependent on the location of the closest point.
  - It is less likely that a user's specific site will unknowingly be on the high or low side of a discontinuity in the predictor.

If the DPP actually fits data better than the IDP, a directivity model based on the DPP should be chosen in preference to a model using the IDP.

REFERENCES

Abrahamson, N. (2000). Effects of rupture directivity on probabilistic seismic hazard analysis, *6th Int. Conf. on Seismic Zonation*, **Proceedings:** Earthq. Eng. Res. Inst. CD-2000-01.

Abrahamson, N., and W. Silva (2008). Summary of the Abrahamson and Silva NGA ground motion relations, *Earthq. Spectra* 24(1), 67-97.

Abrahamson, N., G. Atkinson, D. Boore, Y. Bozorgnia, K. Campbell, B. Chiou, I.M. Idriss, W. Silva, and R. Youngs (2008). Comparisons of the NGA ground-motion relations. *Earthq. Spectra* 24(1), 45-66.

Abrahamson, N.A. and R.R. Youngs (1992). A stable algorithm for regression analysis using the random effects model. *Bull. Seismol. Soc. Am.* 82(1), 505-510.

Aki, K. and P. Richards (1980). *Quantitative Seismology*, Freeman, New York.

Baker, J. (2007). Quantitative classification of near-fault ground motions using wavelet analysis. *Bull. Seismol. Soc. Am.* 97(5), 1486-1501.

Boatwright, J. (2007). The persistence of directivity in small earthquakes, *Bull. Seismol. Soc. Am.* 97(6), 1850-1861, doi: 10.1785/0120050228.

Boore, D.M. and G.M. Atkinson (2008). Ground-motion prediction equations for the average horizontal component of PGA, PGV, and 5%-damped PSA at spectral periods between 0.01 s and 10.0 s. *Earthq. Spectra* 24(1), 99-138.

Boore, D.M., J. Watson-Lamprey, and N.A. Abrahamson (2006). Orientation-independent measures of ground motion. *Bull. Seismol. Soc. Am.* 96(4A), 1502-1511.

Boore, D.M. (2010). Orientation-independent, nongeometric-mean measures of seismic intensity from two horizontal components of motion. *Bull. Seismol. Soc. Am.* 100(4), 1830-1835.

Brillinger, D.R. and H.K. Preisler (1985). Further analysis of the Joyner-Boore attenuation data. *Bull. Seismol. Soc. Am.* 75(2), 611-614.

Campbell, K.W. and Y. Bozorgnia (2008). NGA ground motion model for the geometric mean horizontal component of PGA, PGV, PGD and 5% damped linear elastic response spectra for periods ranging from 0.01 to 10 s. *Earthq. Spectra* 24(1), 139-171.

Chiou, B.S.-J, R. Darragh, N. Gregor, and W. Silva (2008). NGA project strong-motion database. *Earthq. Spectra* 24(1), 23-44.

Chiou, B.S-J., and P. Spudich (2012). Preliminary description of the IEP directivity parameter. Unpublished working notes, 10 pp.

Chiou, B. S.-J, and P. Spudich (2013). The Chiou and Spudich NGA-West2 directivity predictor DPP. This volume.

Chiou, B.S.-J., and R.R. Youngs (2008). An NGA model for the average horizontal component of peak ground motion and response spectra. *Earthq. Spectra* 24, 173.

Joyner, W.B., and D.M. Boore (1993). Methods for regression analysis of strong-motion data. *Bull. Seismol. Soc. Am.* 83(2), 469-487

Mai, P.M., P. Spudich, and J. Boatwright (2005). Hypocenter locations in finite-source rupture models. *Bull. Seismol. Soc. Am.* 95(3), 965-980.

Oglesby, D.D., R.J. Archuleta, and S.B. Nielsen (2000). The three-dimensional dynamics of dipping faults. *Bull. Seismol. Soc. Am.* 90(3), 616-628.

Rowshandel, B. (2006). Incorporating Source Rupture Characteristics into Ground Motion Hazard Analysis Models. *Seismol. Res. Let.* 77, 708-722.

Rowshandel, B. (2010). Directivity correction for the Next Generation Attenuation (NGA) relations. *Earthq. Spectra* 26(2), 525-559, doi 10.1193/1.3381043.

Rowshandel, B. (2013). Rowshandel's NGA-West2 directivity model. This volume.

Schmedes, J., and R.J. Archuleta (2008). Near-source ground motion along strike-slip faults: Insights into magnitude saturation of PGV and PGA. *Bull. Seismol. Soc. Am.* 95(5), 2278-2290.

Seekins, L. and J. Boatwright (2010). Rupture directivity of moderate earthquakes in northern California. *Bull. Seismol. Soc. Am.* 100(3), 107-1119.

Shahi, S.K. (2013). *A probabilistic framework to include the effects of near-fault directivity in seismic hazard assessment.* PhD Thesis, Dept. of Civil and Environmental Engineering, Stanford University, Stanford, CA. Available at www.stanford.edu/~bakerjw/pulse-classification.html.

Shahi, S.K. and J.W. Baker (2011). An empirically calibrated framework for including the effects of near-fault directivity in probabilistic seismic hazard analysis. *Bull. Seismol. Soc. Am.* 101(2), 742-755.

Shahi, S.K. and J.W. Baker (2012). NGA West2 Models for Directionality, *PEER Report 2012/xx*. Pacific Earthquake Engineering Research Center, University of California, Berkeley, CA

Shahi, S.K. and J.W. Baker (2013). The Shahi Baker directivity model. This volume.

Somerville, P.G. (2003). Magnitude scaling of the near fault rupture directivity pulse. *Phys. Earth Planet. Inter.* 137(1), 201-212.

Somerville, P.G., N.F. Smith, R.W. Graves, and N.A. Abrahamson (1997). Modification of empirical strong ground motion attenuation relations to include the amplitude and duration effects of rupture directivity. *Seismol. Res. Let.* 68(1), 199-222.

Spudich, P., B.S.-J.Chiou, R. Graves, N. Collins, and P. Somerville (2004). A formulation of directivity for earthquake sources using isochrone theory. *U.S. Geological Survey Open File Report 2004-1268*. 54 pp

Spudich, P., and B.S.-J. Chiou (2008). Directivity in NGA earthquake ground motions: Analysis using isochrone theory. *Earthq. Spectra* 25(1), 279-298.

Spudich, P., and B.S.-J. Chiou (2013). The Spudich and Chiou NGA-West2 narrow-band directivity model with predictor DPP. This volume.

Spudich, P., and L.N. Frazer (1984). Use of ray theory to calculate high-frequency radiation from earthquake sources having spatially variable rupture velocity and stress drop. *Bull. Seismol. Soc. Am.* 74(6), 2061-2082.

Spudich, P., and K.B. Olsen (2001). Fault zone amplified waves as a possible seismic hazard along the Calaveras fault in central California. *Geophys. Res. Let.* 28, 2533-2536.

Appendix A: Examples of Rupture Length De-Normalization, Rowshandel Model

In this appendix, example effective rupture lengths, used for de-normalization in the directivity parameter, as expressed in Equations (3.7) and (3.8) and shown in Figure 3.2 in the main text, are graphically illustrated for a number of multi-segment strike-slip and dip-slip faults. Specifically, L_s, the "along-strike" effective rupture length, and $L_{-effective}$ (same as L_{rup} in Equation 3.7), which includes the up-dip rupture length (L_w) are shown for Loma Prieta, Landers, Kocaeli, Chi-Chi, and Duce' earthquake faults. Numbers on the contours are in km, representing site-specific L_s and L_{rup}, respectively.

For "multiple-event" earthquakes (EQIDs: #12, #30, #129, #158, #169, #277, and #280), each event (consisting of one or multiple fault segments with own hypocenter), as was explained in the main text, for computation of contributions to the ξ parameter, and hence for computation of L_s and L_{rup}, is treated as a separate source.

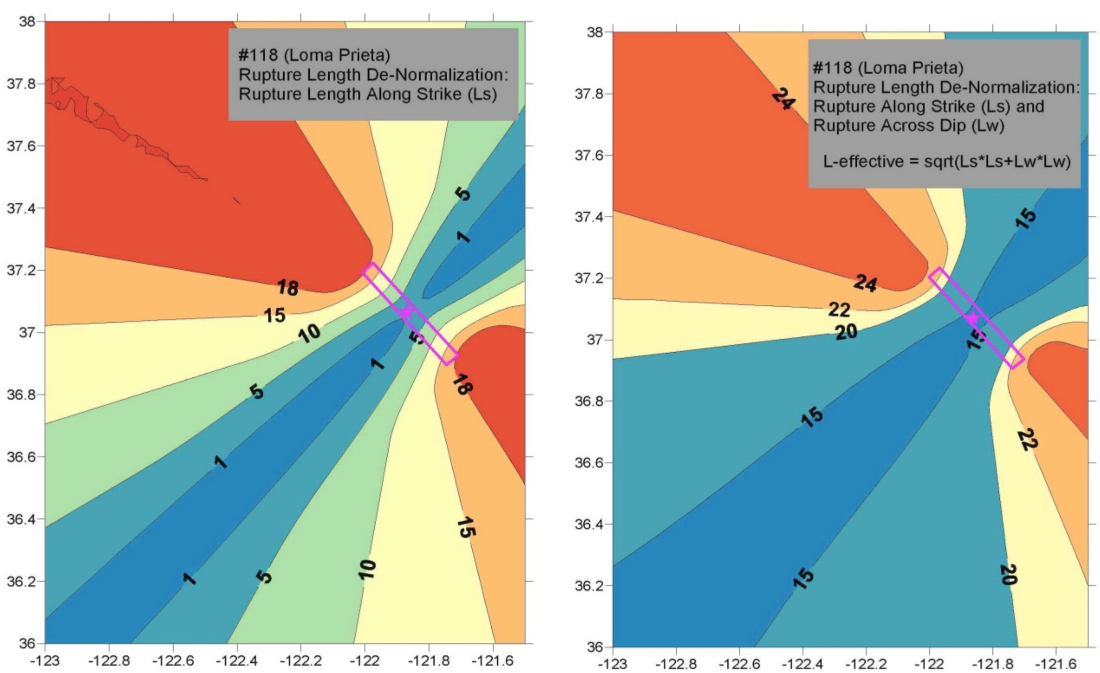

Figure A.1 **Example effective rupture lengths, used for de-normalization in the directivity parameter, graphically illustrated for a number of multi-segment strike-slip and dip-slip faults. Numbers on the contours are in km, representing site-specific L_s (left) and L_{rup}(right) respectively.**

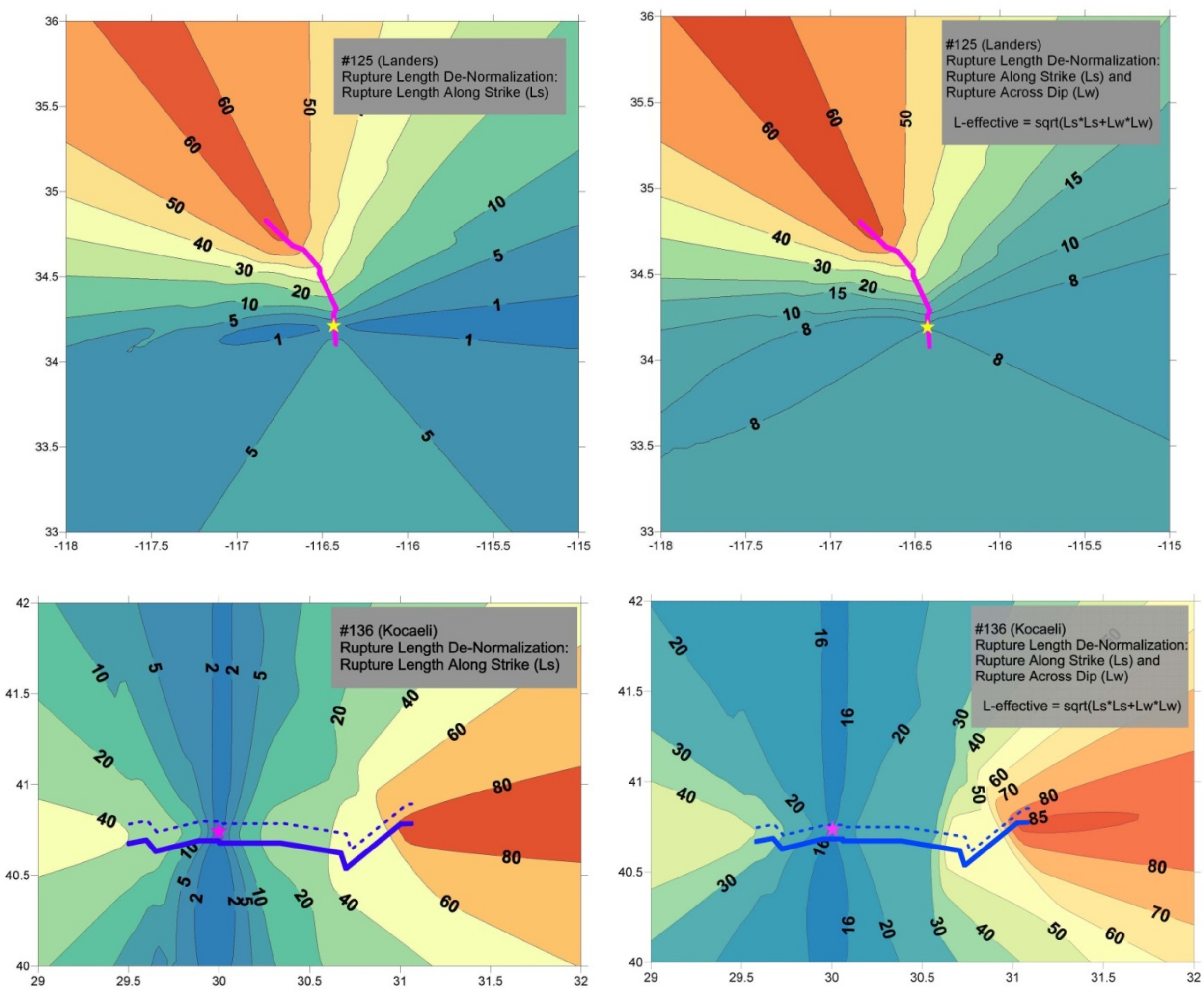

Figure A.1 (Continued)

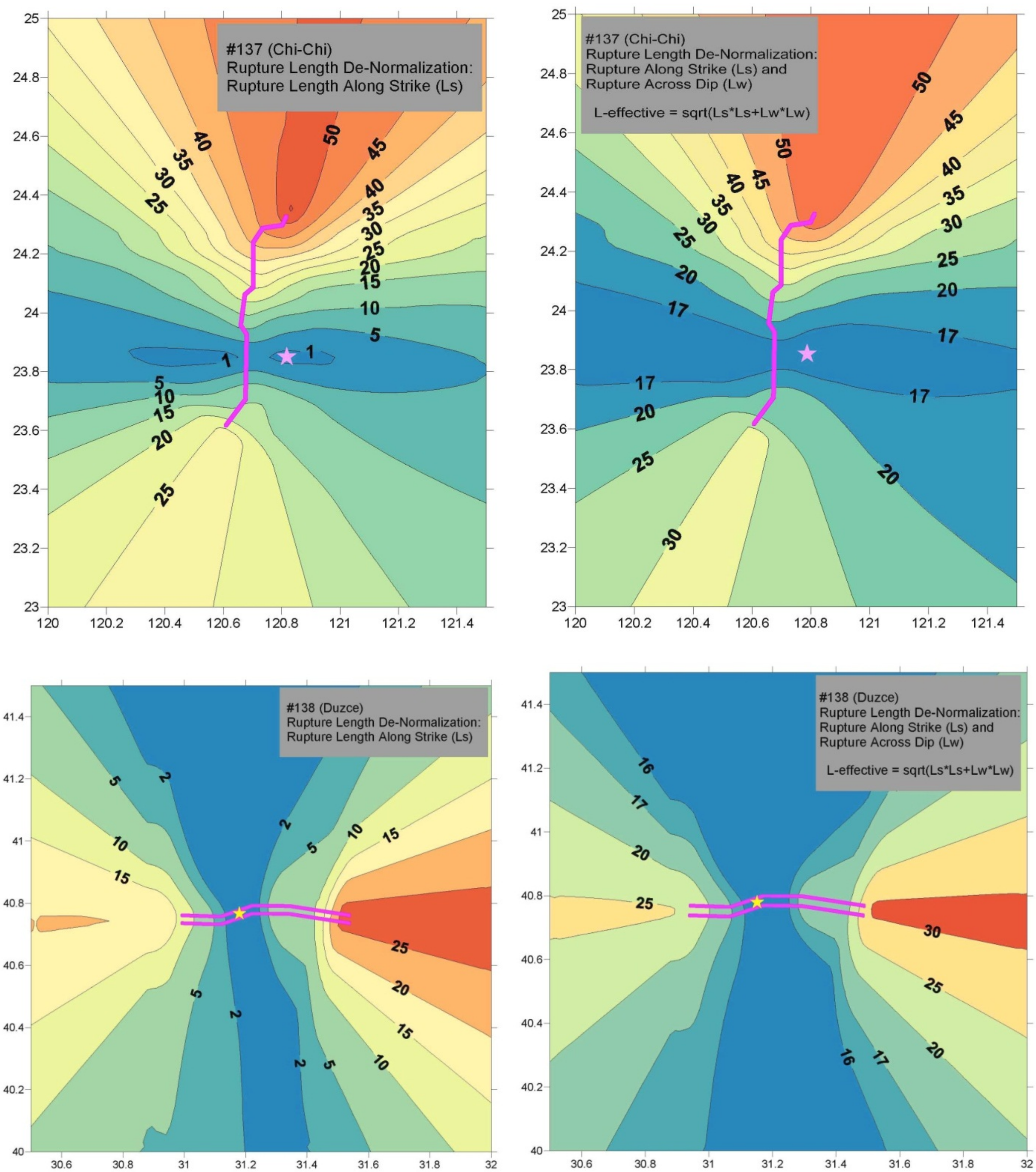

Figure A.1 (Continued)

Appendix B: Narrow-Band Analyses, Rowshandel Model

Linear regression is performed on five sets of intra-event ground motion residuals (based on the five GMPEs) to study the level of correlation of the residuals with the directivity parameter. The directivity coefficient C_1 and the correlation coefficient R^2 are obtained for individual earthquakes with finite fault data, used in each GMPE and for periods of 0.5, 1, 2, 3, 5, 7.5, and 10 seconds. In the majority of the cases positive correlations, resulting in positive values for C_1, are observed. C_1 and R^2 values, when the former turns out to be positive and using directivity Model-I, are listed in Tables B.1 through B.5.

The level or strength of directivity in each earthquake is observed to depend on the period. For the majority of the earthquakes the directivity coefficient C_1 and the correlation coefficient R^2 attain their maximum values at a single period for the majority of the earthquakes. This would indicate the period at which directivity attains its largest values for these earthquakes. However, these coefficients might gain large values (i.e., multiple peaks) at more than one period for each earthquake. This corresponds to multiple directivity-dominant periods for some earthquakes. The period corresponding to maximum directivity for each earthquake, identified by maximum or large values of C_1 (> 0) and R^2 is taken as the "directivity pulse period", and is shown by T_p.

In order to facilitate identifying the directivity pulse period for different earthquakes, according to the five sets of GMPE intra-event residuals, the variation of C_1 and R^2 values, shown in Tables B.1 through B.5 are graphically depicted in Figure B.1.

Table B.1 Directivity coefficient C_1 (left) and correlation coefficients R^2 (right) based on A&S GMPE.

EQID	M	SA0.5	SA1	SA2	SA3	SA4	SA5	SA7.5	SA10
30	6.61	1.85		0.22	4.41	6.5	7.31	14.93	
48	5.74	5.21							
50	6.53			0.08	1.6	1.71	2.04		0.4
68	6.9					1.13			
73	5.9	0.26			2.5	5.31	4.24	6.19	
76	6.36	5.97							
90	6.19		0.21		0.32	0.4	1.43	1.61	
91	5.8		1.57						
101	6.06		0.37	0.14			0.6		
102	5.77	2.98							
103	6.19	5.73	6.92	2.6	2.49	2.05	2.38	0.48	
116	6.54	0.04	0.26	0.96	0.59	1.1	1.61		
118	6.93	0.82	1.73	2.09	2.99	2.06	1.17	1.65	1.19
123	7.01				2.24	4.25		1.13	5.67
125	7.28	1.88	2.34	1.65	1.57	1.8	2	3.16	5.62
127	6.69		1.24	1.11	0.95	0.43	0.78	1.6	
129	6.9		1.25						
136	7.51	0.31				1.29	1.21	2.03	1.73
137	7.62	0.78	0.71	1.65	2.16	2.65	3.41	3.78	4.12
158	7.13								0.61
172	6.2	6.2	9.22	9.7	8.81	8.68	10.38	12.06	10.85
173	6.2			0.14	0.28	0.5	0.68	0.53	0.09
174	6.2	0.83	1.71	6.75	11.47	8.1	4.48	4.45	4.29
175	6.3	2.27	2.76	5.48	5.29	4.98	5.02	5.51	5.2
176	6.6		1.33	1.28	0.05				
177	6.5	2.46	0.51	3.87	3.69	5.35	7.91		
179	6		0.36	0.53	0.52	0.2		0.4	1.38
180	6.6								0.22
274	6.3						0.5	0.84	0.05
277	7.9			1.16	1.67	1.5	1.84	2.01	2.66
278	6.8	2.7	1.09	1.13	0.53			1.4	2.54
279	6.9	0.09					0.16	0.72	0.14
280	7.2	2.13	1.56					0.4	
281	7	0.75	0.74	1.52	2.12	2.14	1.59	2.31	2.3

EQID	M	SA0.5	SA1	SA2	SA3	SA4	SA5	SA7.5	SA10
30	6.61	0.05		0	0.57	0.66	0.68	0.88	
48	5.74	0.28							
50	6.53			0	0.12	0.16	0.21		0.01
68	6.9					0.09			
73	5.9	0			0.02	0.09	0.06	0.1	
76	6.36	0.07							
90	6.19		0		0.01	0.01	0.09	0.06	
91	5.8		0.02						
101	6.06		0.01	0			0.02		
102	5.77	0.1							
103	6.19	0.61	0.64	0.23	0.29	0.19	0.24	0.02	
116	6.54	0	0.02	0.06	0.02	0.08	0.18		
118	6.93	0.08	0.26	0.32	0.48	0.31	0.1	0.12	0.07
123	7.01				0.05	0.12		0	0.1
125	7.28	0.19	0.37	0.24	0.19	0.19	0.2	0.29	0.52
127	6.69		0.06	0.04	0.03	0.01	0.03	0.15	
129	6.9		0.12						
136	7.51	0.01				0.12	0.13	0.82	0.37
137	7.62	0.03	0.03	0.13	0.21	0.27	0.35	0.41	0.42
158	7.13								0.05
172	6.2	0.11	0.21	0.32	0.24	0.19	0.29	0.48	0.42
173	6.2			0	0	0.01	0.02	0.01	0
174	6.2	0.01	0.03	0.21	0.46	0.26	0.08	0.08	0.13
175	6.3	0.13	0.19	0.39	0.32	0.29	0.35	0.45	0.48
176	6.6		0.08	0.16	0				
177	6.5	0.8	0.03	0.58	0.43	0.61	0.71		
179	6		0	0.01	0.01	0		0.01	0.11
180	6.6								0
274	6.3						0.01	0.01	0
277	7.9			0.07	0.11	0.09	0.13	0.14	0.25
278	6.8	0.11	0.01	0.02	0			0.03	0.09
279	6.9	0					0	0.02	0
280	7.2	0.45	0.24					0.02	
281	7	0.04	0.04	0.14	0.31	0.46	0.33	0.48	0.56

Table B.2 Directivity coefficient C_1 (left) and correlation coefficients R^2 (right) based on B&A GMPE.

EQID	M	SA0.5	SA1	SA2	SA3	SA4	SA5	SA7.5	SA10
25	6.19	10.85	6.03	1.39	0.38		0.11		
30	6.61	0.32		0.16	5.22	8.02	8.88		
48	5.74	0.14				0.75			
50	6.53			0.13	1.66	1.76	2.06		0.19
64	6.33	8.1	7.28	6.14					
68	6.9				2.51	6.73			
73	5.9	0.13				1.87	0.17	1.37	
76	6.36	4.87							
90	6.19					0.32	1.16	1.03	6.07
91	5.8		2.39	0.1					
101	6.06		0.74	0.84	0.09	0.63	0.75		
102	5.77	5.24					2.22		
103	6.19	5.8	7.21	3.22	3.16	3.09	3.15	0.78	
113	5.99								
116	6.54	0.08	0.3	0.96	0.43	0.85	1.31		
118	6.93	0.01	1.25	2.23	3.3	2.58	1.79	2.17	1.25
123	7.01				4.23	7.51	4.92	9.8	10.99
125	7.28	1.82	2.49	1.93	1.86	2.11	2.34	3.62	5.9
127	6.69		1.34	1.11	1.14	0.68	1.14	2.07	
136	7.51	0.6	0.06			1.51	1.41	2.16	2.06
137	7.62	0.94	0.86	1.73	2.25	2.74	3.4	3.67	4.03
145	5.61	1.68	3.85	25.2					
176	6.6		1.4	1.33	0.1				
177	6.5	2.27		3.13	2.4	4.41	5.86		
179	6		0.22	0.49	0.5	0.28		0.95	1.18
180	6.6	0.24							
262	7.1	6.24							
274	6.3				0.74	0.46	1.85	2.55	0.64
277	7.9			1.36	1.78	1.53	1.74	1.86	2.69
278	6.8	2.79	1.37	1.66	1.56	0.46	0.93	2.48	3.54
279	6.9	0.03					0.57	1.3	0.79
280	7.2	2.29	1.9	0.28		0.26	0.85	1.42	0.3
281	7	0.63	0.57	1.45	2.25	2.26	1.78	2.61	2.97

EQID	M	SA0.5	SA1	SA2	SA3	SA4	SA5	SA7.5	SA10
25	6.19	0.84	0.92	0.08	0.01		0		
30	6.61	0		0	0.59	0.66	0.76		
48	5.74	0				0.03			
50	6.53			0	0.1	0.12	0.16		0
64	6.33	0.75	0.62	0.86					
68	6.9				0.08	0.78			
73	5.9	0				0.01	0	0.01	
76	6.36	0.05							
90	6.19					0.02	0.52	0.42	1
91	5.8		0.06	0					
101	6.06		0.02	0.03	0	0.03	0.05		
102	5.77	0.25					0.07		
103	6.19	0.57	0.61	0.27	0.34	0.32	0.29	0.06	
113	5.99								
116	6.54	0	0.03	0.06	0.01	0.06	0.18		
118	6.93	0	0.14	0.39	0.55	0.46	0.23	0.2	0.11
123	7.01				0.21	0.5	0.13	0.28	0.34
125	7.28	0.18	0.41	0.28	0.24	0.26	0.27	0.39	0.57
127	6.69		0.07	0.04	0.05	0.02	0.06	0.3	
136	7.51	0.04	0			0.26	0.35	0.8	0.86
137	7.62	0.04	0.04	0.14	0.21	0.25	0.33	0.39	0.44
145	5.61	0.08	0.3	0.48					
176	6.6		0.09	0.15	0				
177	6.5	0.5		0.5	0.29	0.54	0.61		
179	6		0	0.01	0.01	0		0.05	0.16
180	6.6	0							
262	7.1	0.49							
274	6.3				0.01	0	0.06	0.08	0
277	7.9			0.08	0.1	0.07	0.08	0.08	0.16
278	6.8	0.11	0.02	0.04	0.04	0	0.02	0.1	0.21
279	6.9	0					0.01	0.05	0.02
280	7.2	0.44	0.27	0.01		0.01	0.05	0.17	0.01
281	7	0.03	0.02	0.13	0.34	0.49	0.37	0.49	0.65

Table B.3 Directivity coefficient C1 (left) and correlation coefficients R2 (right) based on C&B GMPE.

EQID	M	SA0.5	SA1	SA2	SA3	SA4	SA5	SA7.5
25	6.19	10.53	5.68	1.11	0.06			
30	6.61				2.83	8.02	5.94	
48	5.74	4.55				0.75		
50	6.53		0.04	0.2	1.68	1.76	2.04	
64	6.33	8.36	7.69	6.61				
68	6.9				2.47	6.73		
73	5.9				1	1.87	1.59	2.55
76	6.36	5.75					0.55	
90	6.19				0.23	0.32	1.64	2.54
91	5.8		1.87					
101	6.06		0.05			0.63	0.18	
102	5.77	4.05						
103	6.19	5.62	6.71	2.7	2.74	3.09	2.86	1.16
116	6.54	0.18	0.21	0.93	0.6		1.76	
118	6.93	0.62	1.69	2.28	3.37	0.85	1.74	2.21
123	7.01					2.58		2.4
125	7.28	1.69	2.23	1.61	1.49	7.51	1.88	3.31
127	6.69		1.38	1.4	1.12	2.11	1.49	2
129	6.9		1.17		0.19	0.68		0.44
136	7.51	0.14				1.51	0.89	1.74
137	7.62	0.42	0.17	0.94	1.36	2.74	2.48	2.9
138	7.14	0.09	1.12					
146	6.1		0.26				0.32	
176	6.6		1.29	1.15		4.41		
177	6.5	4.29	4.49	7.35	7.26	0.28	7.52	
179	6		0.71	1.12	1.08		0.42	1.32
180	6.6							
262	7.1	7.3	1.59			0.46		
274	6.3	1.77	3.85	3.57	2.79	1.53	4.27	3.99
277	7.9			0.28	0.66	0.46	0.81	1.13
278	6.8	2.45	1.14	1.29	0.88			1.41
279	6.9					0.26	0.05	0.88
280	7.2	2.13	1.63			2.26	0.29	1.09
281	7	0.45	0.42	1.31	2.07		1.55	2.25

EQID	M	SA0.5	SA1	SA2	SA3	SA4	SA5	SA7.5
25	6.19	0.84	0.88	0.04	0			
30	6.61				0.28	0.51	0.71	
48	5.74	0.15						
50	6.53		0	0	0.13	0.16	0.2	
64	6.33	0.8	0.68	0.94				
68	6.9				0.07	0.64		
73	5.9				0	0.04	0.01	0.02
76	6.36	0.06					0	
90	6.19				0	0.02	0.18	0.23
91	5.8		0.02					
101	6.06		0				0	
102	5.77	0.16						
103	6.19	0.6	0.67	0.25	0.34	0.26	0.31	0.11
116	6.54	0	0.01	0.05	0.02	0.08	0.2	
118	6.93	0.05	0.23	0.42	0.57	0.46	0.25	0.24
123	7.01					0.02		0.04
125	7.28	0.17	0.38	0.24	0.16	0.18	0.18	0.36
127	6.69		0.08	0.08	0.07	0.04	0.13	0.23
129	6.9		0.12		0	0.01		0.02
136	7.51	0				0.13	0.16	0.63
137	7.62	0.01	0	0.05	0.1	0.15	0.25	0.31
138	7.14	0	0.05					
146	6.1		0.01				0.02	
176	6.6		0.08	0.14				
177	6.5	0.79	0.67	0.72	0.56	0.49	0.56	
179	6		0.01	0.04	0.04	0.03	0.01	0.09
180	6.6							
262	7.1	0.49	0.03					
274	6.3	0.04	0.21	0.09	0.08	0.08	0.21	0.09
277	7.9			0	0.02	0.01	0.03	0.06
278	6.8	0.09	0.02	0.02	0.01			0.03
279	6.9						0	0.02
280	7.2	0.48	0.3				0.01	0.13
281	7	0.01	0.01	0.11	0.31	0.47	0.37	0.45

Table B.4 Directivity coefficient C_1 (left) and correlation coefficients R^2 (right) based on C&Y GMPE.

EQID	M	SA0.5	SA1	SA2	SA3	SA4	SA5	SA7.5	SA10
30	6.61	1.64		0.19	4.39	6.47	7.21	13.17	
48	5.74	6.03							
50	6.53		0.13	0.36	1.93	1.88	2.24		0.44
68	6.9					1.09			
69	6.2			0.29					
73	5.9	0.55			2.01	4.64	3.4	4.84	
76	6.36	6.01							
90	6.19				0.21	0.13	2.58	1.94	
91	5.8	0.31	4.55	2.12					
101	6.06						0.48		
102	5.77	2.3							
103	6.19	5.65	6.79	2.56	2.45	2.08	2.54	0.89	
116	6.54			0.15	0.13	0.69	1.25		
118	6.93	0.66	1.63	2.11	3.14	2.36	1.63	2.1	1.94
125	7.28	2.57	2.51	1.18	1.72	2.25	3.63	3.98	5.32
127	6.69	0.13	1.64	1.2	0.92	0.35	0.73	1.81	
129	6.9		0.69						
136	7.51	0.24				1.09	0.99	1.69	0.75
137	7.62			1.12	1.82	2.39	3.16	3.24	3.36
146	6.1						0.15		
172	6.2	4.16	8.04	9.22	8.98	9.6	11.84	14.56	13.9
173	6.2			0.09	0.32	0.62	0.81	0.93	0.68
174	6.2	0.65	1.48	6.33	11.12	7.77	4.23	3.88	3.31
175	6.3	2.37	2.83	5.31	4.99	4.64	4.71	5.14	4.75
176	6.6		1.26	1.14					
177	6.5	2.77	0.83	3.97	3.75	5.35	8.06		
179	6		0.2	0.36	0.31	0		0.21	1.63
262	7.1	6.34							
274	6.3	1.75	1.65	0.92	0.91	1.01	2.43	2.87	2.29
277	7.9			0.3	0.68	0.43	0.75	0.89	1.63
278	6.8	2.75	1.12	0.95	0.36			1.63	2.82
279	6.9						0.12	0.88	0.31
280	7.2	1.52	0.81						
281	7	0.67	0.67	1.46	2.08	2.11	1.57	2.22	2.48

EQID	M	SA0.5	SA1	SA2	SA3	SA4	SA5	SA7.5	SA10
30	6.61	0.05		0	0.57	0.69	0.76	0.93	
48	5.74	0.39							
50	6.53		0	0.01	0.15	0.17	0.18		0.01
68	6.9					0.04			
69	6.2			0					
73	5.9	0.01			0.02	0.09	0.05	0.08	
76	6.36	0.07							
90	6.19				0	0	0.21	0.1	
91	5.8	0	0.14	0.03					
101	6.06						0.01		
102	5.77	0.06							
103	6.19	0.63	0.7	0.24	0.31	0.21	0.29	0.06	
116	6.54			0	0	0.03	0.09		
118	6.93	0.06	0.21	0.42	0.55	0.4	0.21	0.2	0.2
125	7.28	0.34	0.44	0.2	0.24	0.26	0.54	0.44	0.65
127	6.69	0	0.09	0.05	0.04	0.01	0.03	0.14	
129	6.9		0.04						
136	7.51	0.01				0.15	0.22	0.58	0.95
137	7.62			0.06	0.16	0.23	0.32	0.34	0.35
146	6.1						0		
172	6.2	0.05	0.17	0.33	0.26	0.22	0.34	0.55	0.56
173	6.2			0	0	0.02	0.03	0.04	0.02
174	6.2	0.01	0.02	0.19	0.44	0.26	0.08	0.07	0.13
175	6.3	0.15	0.21	0.39	0.31	0.27	0.32	0.4	0.41
176	6.6		0.1	0.18					
177	6.5	0.72	0.05	0.49	0.35	0.5	0.57		
179	6		0	0	0	0		0	0.14
262	7.1	0.4							
274	6.3	0.07	0.06	0.01	0.01	0.03	0.12	0.11	0.06
277	7.9			0.01	0.02	0.01	0.02	0.03	0.12
278	6.8	0.11	0.02	0.01	0			0.04	0.14
279	6.9						0	0.02	0
280	7.2	0.27	0.06						
281	7	0.03	0.03	0.14	0.3	0.47	0.37	0.47	0.61

Table B.5 Directivity coefficient C_1 (left) and correlation coefficients R^2 (right) based on Id GMPE.

EQID	M	SA0.5	SA1	SA2	SA3	SA4	SA5	SA7.5	SA10	EQID	M	SA0.5	SA1	SA2	SA3	SA4	SA5	SA7.5	SA10
30	6.61	4.49	2.92							30	6.61	0.05	0.02						
68	6.9				3.06	7.27				68	6.9				0.1	0.76			
90	6.19				0.01	0.76				90	6.19				0	0.32			
118	6.93	0.05	0.29	1.9	3.26	1.99	1.5	1.84	0.39	118	6.93	0	0.02	0.46	0.75	0.68	0.41	0.19	0.03
127	6.9						1.39	5.65		127	6.9						0.07	0.75	
137	7.62		0.21	1.36	2.25	2.56	3.15	3.26	3.84	137	7.62		0	0.09	0.26	0.34	0.43	0.44	0.48
138	7.14			4.91	2.54	7.43	8.54	15.56	14.62	138	7.14			0.33	0.06	0.41	0.71	0.91	0.9
171		0.09	1.7							171		0	0.02						
172	6.2	8.14	10.31	10.92	10.19	10.99	13.28	16.92	16.61	172	6.2	0.11	0.14	0.32	0.25	0.3	0.41	0.61	0.57
173	6.2			0.3	0.04	0.47	0.89	0.88	0.78	173	6.2			0	0	0.01	0.03	0.03	0.03
174	6.2	0.36	0.51	4.87	11.28	7.54	4.83	3.6	2.97	174	6.2	0	0	0.14	0.59	0.38	0.16	0.09	0.21
175	6.3	2.13	2.09	3.85	3.68	3.04	2.92	3.65	3.55	175	6.3	0.11	0.1	0.25	0.21	0.16	0.18	0.32	0.32
274	6.3						1.42	3.11	3.36	274	6.3						0.03	0.09	0.09

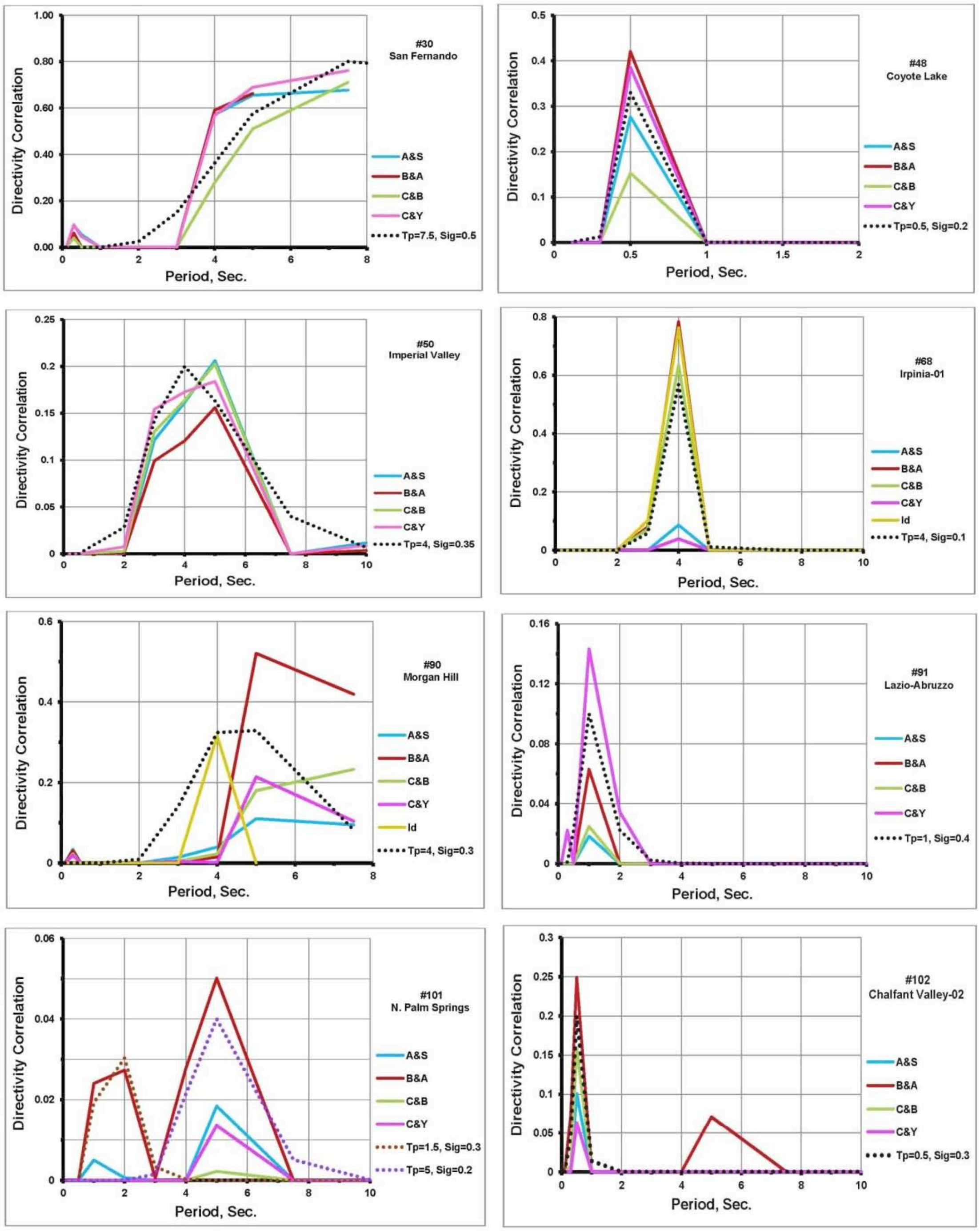

Figure B.1 **Directivity correlation R^2 for different ground motion periods for individual earthquakes with finite fault data based on the five sets of GMPE residuals. Also shown in the individual figures are the identified pulse period(s) based on the maximum value(s) of R^2 and the value(s) of the bandwidth *sig* based on Equation (3.16) in the main text.**

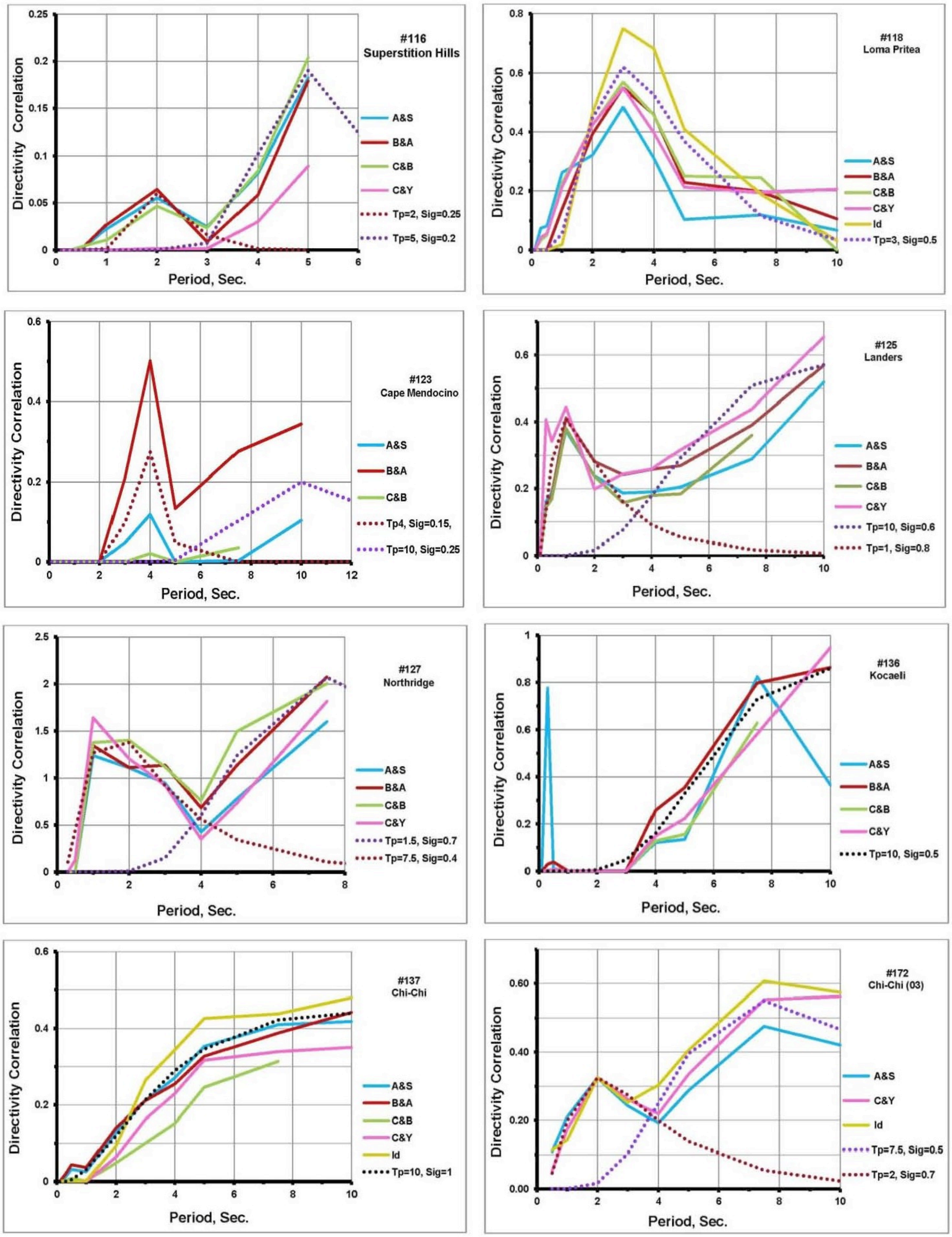

Figure B.1 (Continued)

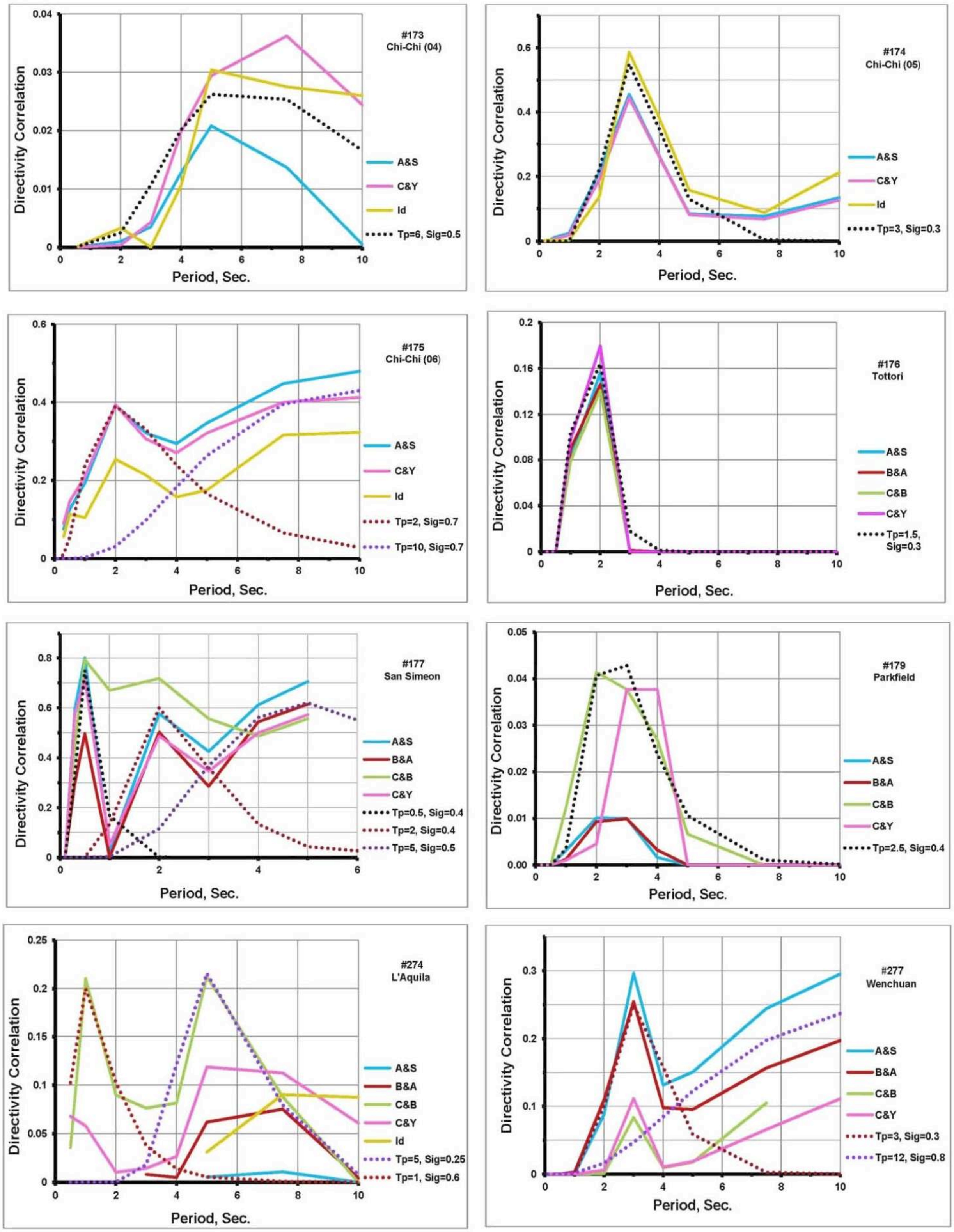

Figure B.1 (Continued)

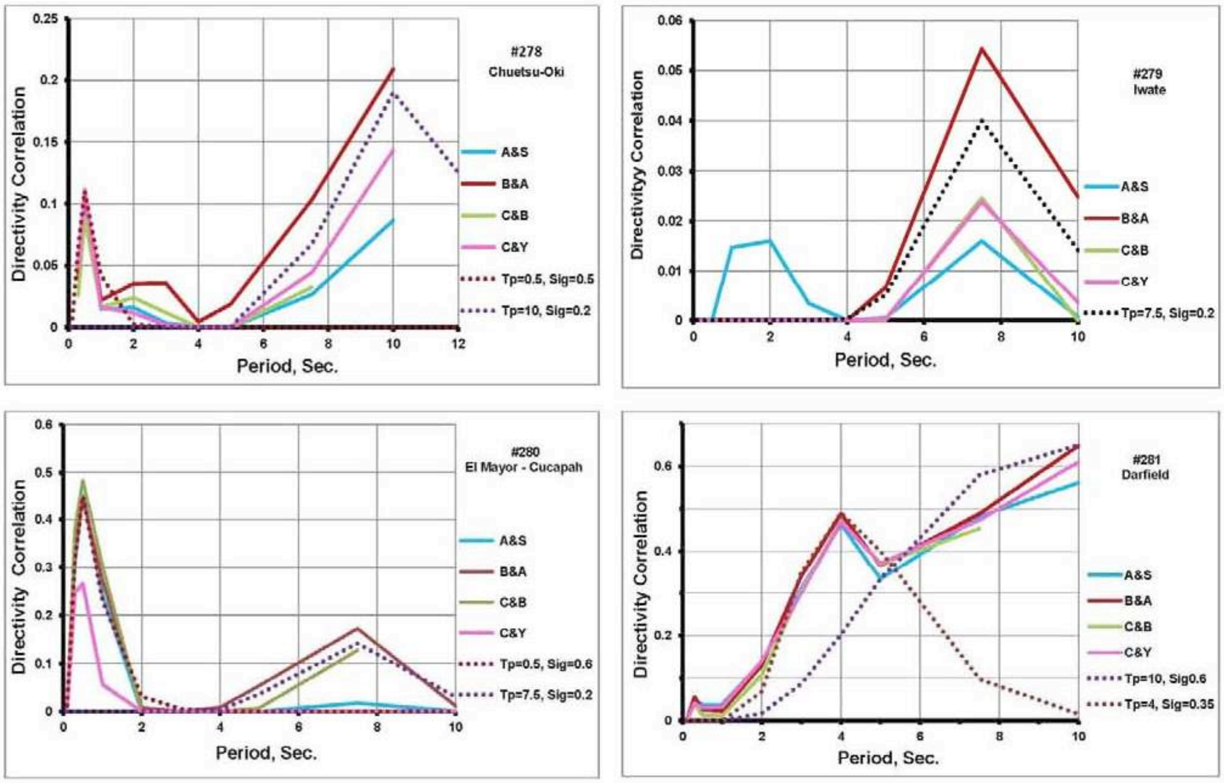

Figure B.1 (Continued)

Appendix C: Sample Results, Rowshandel Model

Using a set of average directivity coefficients, based on the values presented in Table 3.2 (equally weighted using based on A&S, B&A, C&B, and C&Y results), the distributions of the directivity amplification term, defined as *exp*($C_1\xi$) were obtained for a number of earthquakes in the NGA-W2 database. Results for different periods for Landers (EQID #125), Chi-Chi (EQID #137) and Denali (EQID #169) are presented in this appendix. It is to be noted that the effect of the free parameter C_2 may not be present in these results. Also, since the directivity coefficients used to produce these results are based on an older and preliminary version of ground motion residuals of four GMPEs, the numerical vales of the directivity amplification factor, presented in these figures, should not be taken as a final prediction of this model, as with the changes and modifications of the GMPEs during the time since the release of the preliminary residuals the contour levels shown in these figures will change. But the shape and the distribution of the amplification factors (e.g., locations of high and low directivity) will remain the same.

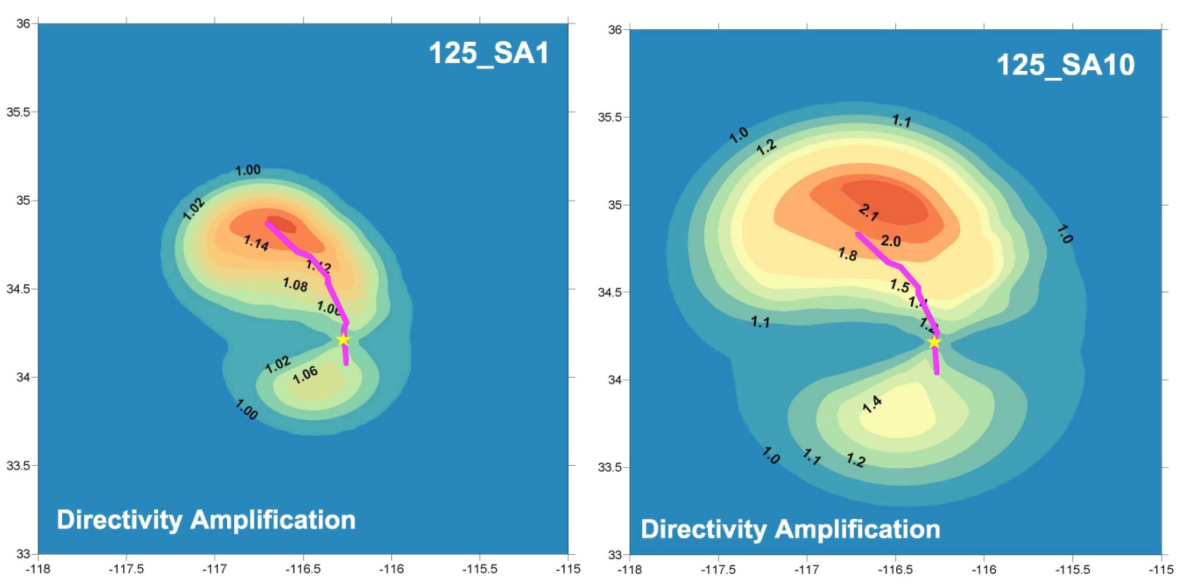

Figure C.1 Maps of the directivity amplification term *exp*($C_1\xi$) for the Landers (#125), Chi-Chi (#137) and Denali (#169) earthquakes. In label SA*nn*, *nn* = period (sec).

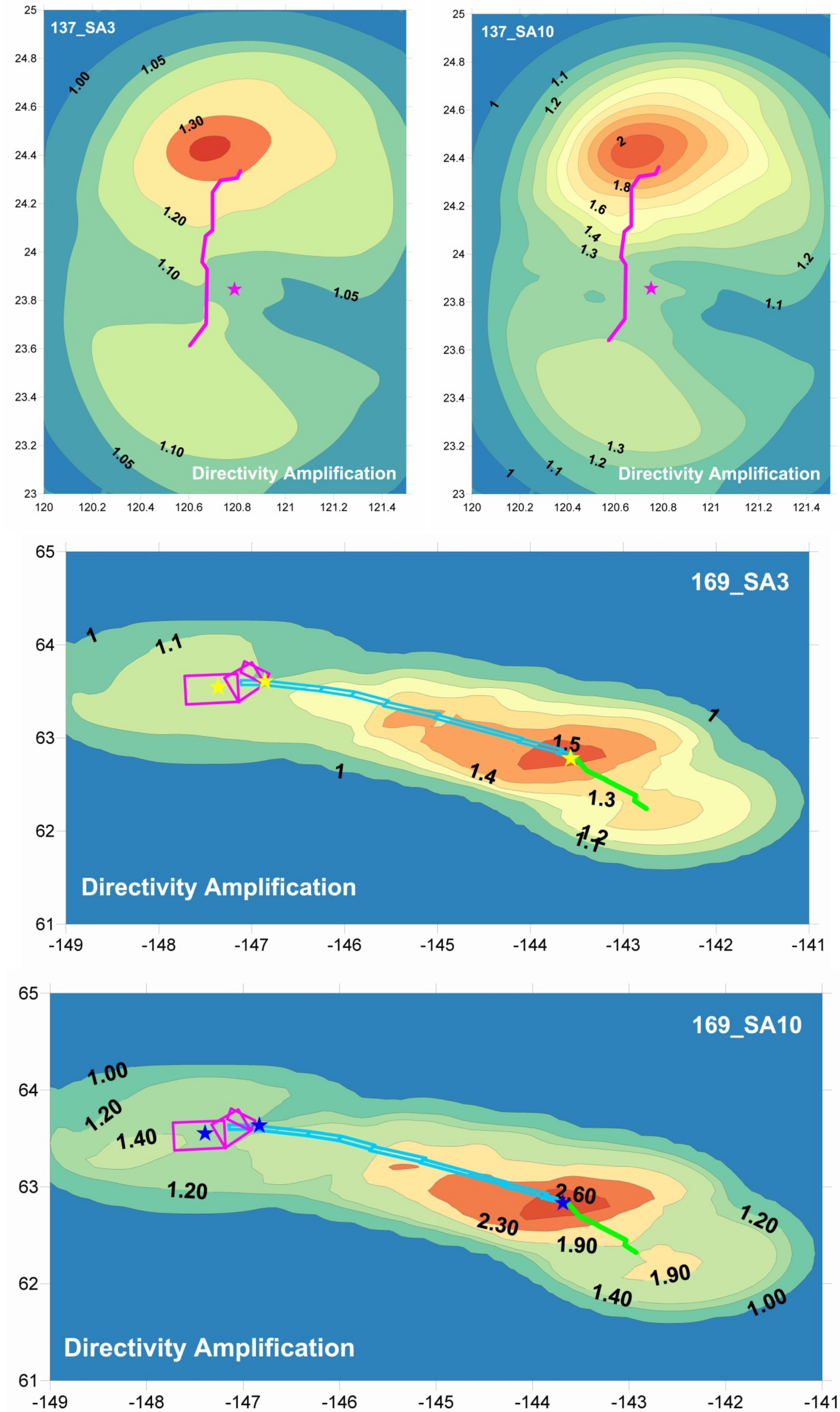

Figure C.1 (Continued)

Appendix D: Calculation of Distance D, Spudich and Chiou Model

In this appendix, we give the specific algorithm we use to calculate parameters *D* and *s*, used in the *IDP*. This algorithm was described in general terms in Spudich and Chiou [2008] Appendix A, text and Figure A13.

D.1 FAULT GEOMETRY INPUTS

We use the Cartesian coordinate system shown in Figure D.1 Terms used below include:

- The *X*-, *Y*-, and *Z*-coordinates of hypocenter $\vec{P}_{Hyp}$
- The *X*-, *Y*-, and *Z* -coordinates of corner points $\{\vec{P}_1^k, \vec{P}_2^k, \vec{P}_3^k, \vec{P}_4^k\}$ which are arranged sequentially around the *k*th quadrilateral. $\vec{P}_1^k$ and $\vec{P}_2^k$ are at the top of the quadrilateral, with strike pointing from $\vec{P}_1^k$ to $\vec{P}_2^k$, and $\vec{P}_3^k$ and $\vec{P}_4^k$ are at the bottom of the quadrilateral, with $\vec{P}_3^k$ on the same edge as $\vec{P}_2^k$.
- The total number (*n*) of fault segments (quadrilaterals);
- Depth[1] to the top of fault H_{Top}, which is constant and equal for all quadrilaterals.
- Depth to the bottom of fault H_{Bottom}, which is constant and equal for all quadrilaterals.

The superscript denotes the fault segment number, and the subscript indicates the name of a point (such as $\vec{P}_{Hyp}$ for hypocenter) or the numbering of a vertex. The top of the fault is defined by $\{\vec{P}_1^1, \vec{P}_1^2, \cdots, \vec{P}_1^i, \cdots \vec{P}_1^n,\ \vec{P}_2^n\}$ (Figure D.2). Note that the corner point $\vec{P}_2^i$ is co-located with $\vec{P}_1^{i+1}$. The top of fault is placed at a constant depth of H_{Top}, so all its vertices have the same *Z*-coordinate of -H_{Top}.

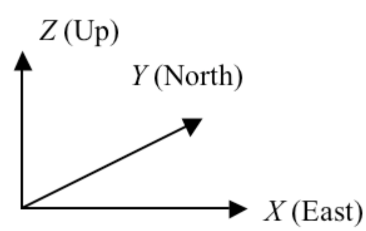

Figure D.1 The Cartesian coordinate system.

[1] We use the capital letter *H* for depth, and the letter *Z* for *Z*-coordinate.

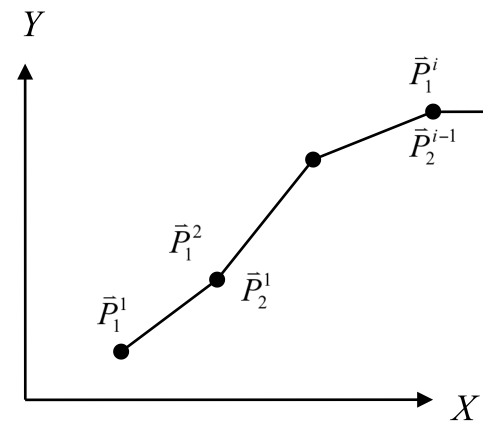

Figure D.2 Parameters defining the fault trace.

Fault strike is not explicitly given as input, but it is implied by the corner points defining the top of the fault and the order they are given. Specifically, strike direction of the i-th segment is the direction of vector $\vec{P}_1^{i+1} - \vec{P}_1^i$. The fault width is implicitly given by $Width = (H_{Bottom} - H_{Top}) / \sin(\delta)$, where δ is dip of the particular quadrilateral.

D.2 AUXILIARY LINE ON CURVED FAULT

One can draw on fault a piecewise linear curve subparallel to the top of the fault. We call it the "auxiliary line" (some call it "line of strike"). An auxiliary line is characterized by its Z-coordinate (all points on an auxiliary line have the same Z-coordinate). For example, the bottom of fault is the auxiliary line of $Z = -H_{Bottom}$. At a given z, the auxiliary line is defined by

$$\left\{\vec{Q}_1^1(z), \vec{Q}_1^2(z), \vec{Q}_1^3(z), \cdots, \vec{Q}_1^i(z), \cdots, \vec{Q}_1^n(z), \vec{Q}_2^n(z)\right\}, \tag{D.1}$$

where

$$\begin{aligned} \vec{Q}_1^i(z) &= \vec{Q}_2^{i-1}(z) \\ &= \vec{P}_1^i + (\vec{P}_4^i - \vec{P}_1^i)(z - z_{\vec{P}_1^i})/(z_{\vec{P}_4^i} - z_{\vec{P}_1^i}) \\ \vec{Q}_2^n(z) &= \vec{P}_2^n + (\vec{P}_3^n - \vec{P}_2^n)(z - z_{\vec{P}_2^n})/(z_{\vec{P}_3^n} - z_{\vec{P}_2^n}). \end{aligned} \tag{D.2}$$

$$s_{\vec{P}} = \left|\vec{P} - \vec{Q}_1^k(z_{\vec{P}})\right| + \sum_{i=1}^{i=k-1}\left|\vec{Q}_2^i(z_{\vec{P}}) - \vec{Q}_1^i(z_{\vec{P}})\right| \tag{D.3}$$

The auxiliary line is useful in specifying location on a curved fault. A point $\vec{P}$ on the curved fault has two degrees of freedom: its Z-coordinate $z_{\vec{P}}$ and its distance $s_{\vec{P}}$ to the reference point $\vec{Q}_1^1$ measured along the auxiliary line, where k is the segment on which $\vec{P}$ lies, $s_{\vec{Q}_1^k} \le s_{\vec{P}} <$

$s_{\vec{Q}_2^k}$. In practice, $s_{\vec{P}}$ is needed only for elevation $z_{\vec{P}_{HYP}}$. The Cartesian coordinates of $\vec{P}$ can be obtained by

$$\vec{P}(z_{\vec{P}}, s_{\vec{P}}) = \vec{Q}_1^k(z_{\vec{P}}) + (s_{\vec{P}} - s_{\vec{Q}_1^k}) * (\vec{Q}_2^k(z_{\vec{P}}) - \vec{Q}_1^k(z_{\vec{P}})) / \left|\vec{Q}_2^k(z_{\vec{P}}) - \vec{Q}_1^k(z_{\vec{P}})\right| \tag{D.4}$$

D.3 CALCULATING ISOCHRONE PARAMETERS D AND S ON CURVED FAULT

For the case of planar fault, *D* is simply the straight-line distance between $\vec{P}_{Hyp}$ and $\vec{P}_c$ [Spudich and Chiou 2008]. For a curved fault, $\vec{P}_{Hyp}$ and $\vec{P}_c$ may be on two different quadrilaterals. If this situation occurs, then *D* can no longer be measured as the straight-line distance between $\vec{P}_{Hyp}$ and $\vec{P}_c$. Depending on how one draws on fault the line connecting these two points, different values of *D* may be obtained. We prefer a multi-segment line that ascends (or descends) gradually toward $\vec{P}_c$, gaining (or losing) elevation by an amount proportional to the horizontal distance traversed inside a quadrilateral. This is formalized as followed. If i_{Pc} is greater than or equal to i_{Hyp}, the connecting line, starting from $\vec{P}_{Hyp}$, is defined by $\{\vec{O}^{i_{Hyp}}, \vec{O}^{i_{Hyp+1}}, \cdots, \vec{O}^{i}, \cdots \vec{O}^{i_{Pc}}, \vec{O}^{i_{Pc+1}}\}$, where

$$\begin{aligned}
&\vec{O}^{i_{Hyp}} = \vec{P}_{Hyp} \\
&\vec{O}^{i_{P_c}+1} = \vec{P}_{P_c} \\
&\vec{O}^{i} = \vec{P}_1^i + (\vec{P}_4^i - \vec{P}_1^i)\frac{z_{\vec{O}^i} - z_{\vec{P}_1^i}}{z_{\vec{P}_4^i} - z_{\vec{P}_1^i}}, \qquad i \neq i_{Hyp}\ \&\ i \neq i_{P_c}+1 \\
&z_{\vec{O}^i} = z_{\vec{P}_{HYP}} + \frac{s_{\vec{Q}_1^i} - s_{\vec{P}_{Hyp}}}{s_{\vec{P}_c^*} - s_{\vec{P}_{Hyp}}}(z_{\vec{P}_c} - z_{\vec{P}_{HYP}}) \\
&D = \sum_{i=i_{HYP}}^{i=i_{P_c}} \left|\vec{O}^{i+1} - \vec{O}^{i}\right|
\end{aligned} \tag{D.5}$$

If i_{Pc} is less than i_{Hyp}, the connecting line, starting from $\vec{P}_c$, is then defined by the set of points $\{\vec{O}^{i_{Pc}}, \vec{O}^{i_{Pc+1}}, \cdots, \vec{O}^{i}, \cdots, \vec{O}^{i_{Hyp}}, \vec{O}^{i_{Hyp+1}}\}$, where

$$
\begin{aligned}
&\vec{O}^{i_{P_c}} = \vec{P}_{P_c} \\
&\vec{O}^{i_{Hyp}+1} = \vec{P}_{Hyp} \\
&\vec{O}^{i} = \vec{P}_1^{i} + (\vec{P}_4^{i} - \vec{P}_1^{i})\frac{z_{\vec{O}^i} - z_{\vec{P}_1^i}}{z_{\vec{P}_4^i} - z_{\vec{P}_1^i}}, \qquad i \neq i_{P_c} \;\&\; i \neq i_{Hyp}+1 \\
&z_{\vec{O}^i} = z_{\vec{P}_c} + \frac{s_{\vec{Q}_1^i} - s_{\vec{P}_c^*}}{s_{\vec{P}_{Hyp}} - s_{\vec{P}_c^*}}(z_{\vec{P}_{HYP}} - z_{\vec{P}_c}) \\
&D = \sum_{i=i_{P_c}}^{i=i_{Hyp}} \left|\vec{O}^{i+1} - \vec{O}^{i}\right|
\end{aligned}
\tag{D.6}
$$

$\vec{P}_{Hyp}$ and $\vec{P}_c$ are likely to be at a different depth. One thus must pick one of the two points to define the auxiliary line on which $s_{\vec{Q}_1^i}$ will be measured. The choice is arbitrary; in Spudich and Chiou [2008], $\vec{P}_{Hyp}$ was used and we continue to use it here. When $\vec{P}_c$ does not lie on the auxiliary line $\left\{\vec{Q}_1^{i_{Pc}}(z_{Hyp}), \vec{Q}_2^{i_{Pc}}(z_{Hyp})\right\}$ (which is usually the case), we use point $\vec{P}_c^*$ on that line segment for the purpose of computing D and hence $s_{\vec{P}_c^*}$ in the above equation. Point $\vec{P}_c^*$ is at the same fraction of distance from the edge as $\vec{P}_c$ is on line segment $\left\{\vec{Q}_1^{i_{Pc}}(z_{\vec{P}_c}), \vec{Q}_2^{i_{Pc}}(z_{\vec{P}_c})\right\}$, as shown in Figure D.3.

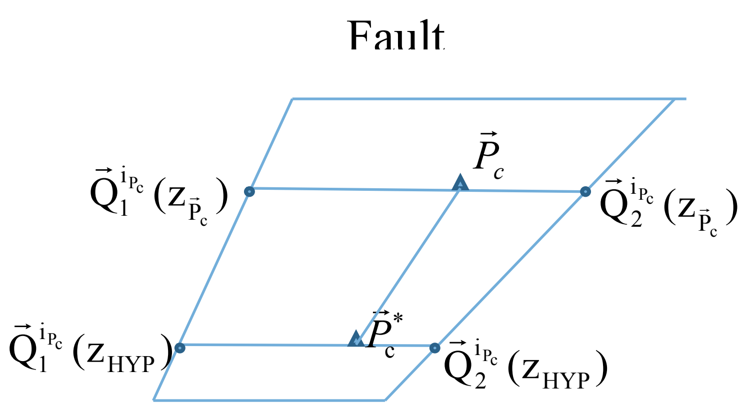

$$
\frac{\left|\vec{P}_c^* - \vec{Q}_1^{i_{Pc}}(z_{HYP})\right|}{\left|\vec{Q}_2^{i_{Pc}}(z_{HYP}) - \vec{Q}_1^{i_{Pc}}(z_{HYP})\right|} = \frac{\left|\vec{P}_c - \vec{Q}_1^{i_{Pc}}(z_{\vec{P}_c})\right|}{\left|\vec{Q}_2^{i_{Pc}}(z_{\vec{P}_c}) - \vec{Q}_1^{i_{Pc}}(z_{\vec{P}_c})\right|}
$$

Figure D.3 A schematic plot showing the definition of point $\vec{P}_c^*$

D.4 EXAMPLES OF THE D-PATHS PRODUCED

Figure D.4 shows example D-paths produced by the above algorithm for the NGA Chi-Chi earthquake geometry. While the algorithm does not purport to find the shortest path between hypocenter and closest point, the paths obtained in this example are plausible.

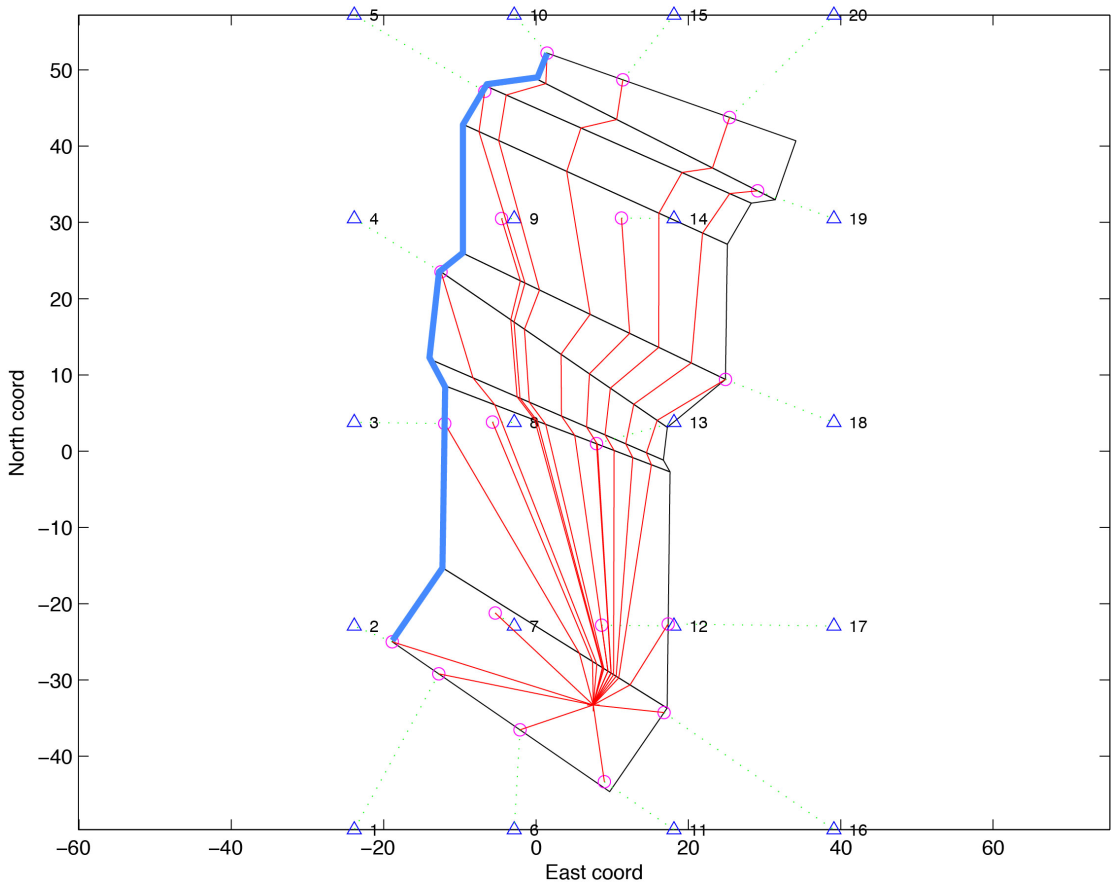

Figure D.4 **D-paths for the 1999 Chi-Chi, Taiwan, earthquake for a test hypocenter located on the southernmost segment. Triangles are a set of hypothetical sites, magenta circles are the closest points on the fault surface to the hypothetical sites, and D-paths are the red lines going from hypocenter to each magenta closest point. Heavy blue line is the fault trace. Black lines are the segment boundaries, seen in map view.**

Appendix E: Parametric Equations for Average IDP of NGA-West 2 Events, Spudich and Chiou

In order to simplify the calculation of $\overline{IDP}(R_{rup})$ for the GMPE developers, we created a parametric approximation of it. First, for each earthquake we calculated IDP on a dense grid of points extending to $R_{jb} = 70$ km. We then fit those data with a simple parametric equation. The following parametric equation gives $\overline{IDP}(R_{rup})$:

$$\overline{IDP}(R_{rup}) = a + \frac{b}{cosh\left(c\ max(R_{rup} - z, 0)\right)} \tag{E.1}$$

where coefficients *a, b, c,* and *z* are given in Table E.1. Variable *z* is the depth to the top of rupture (Z_{TOR} in the flatfile).

Table E.1 Coefficients of parametric average *IDP* as function of R_{rup}

EQID	*a*	*b*	*c*	*z*	EQID	*a*	*b*	*c*	*z*
0006	1.319612	0.952244	0.169479	0	0125	1.19635	1.692021	0.146347	0
0012	0.957419	1.718711	0.14569	0	0127	1.254269	1.320357	0.328484	5
0025	0.764729	1.070378	0.183825	0	0128	0.488613	0.470857	0.382726	3
0028	0.910207	0.887714	0.189113	0	0129	1.27048	0.594765	0.086309	0.2
0030	0.828378	1.40074	0.199661	0	0130	1.064798	1.147045	0.328684	2
0031	0.619972	0.197139	0.226674	2	0134	0.564071	1.012339	0.406464	0
0040	1.194086	1.22584	1.947485	2	0135	1.113392	1.314097	0.132446	0
0041	0.919146	1.484914	0.204516	3	0136	1.577992	1.37516	0.095172	0
0043	0.886756	1.083029	1.548599	1	0137	1.372694	0.828144	0.307079	0
0045	0.642346	-0.402922	0.410293	11.6	0138	1.293188	0.364478	0.100273	0
0046	1.406495	-0.310209	0.08947	1	0140	1.606369	1.705601	0.070505	0
0048	0.341442	0.398286	0.10461	3	0141	1.196887	1.088898	0.170209	2
0050	1.192885	0.909248	0.155513	0	0142	1.851539	2.128102	0.199638	0
0056	0.948427	0.322113	0.626218	1.3	0144	1.342127	0.839406	0.126778	0

EQID	***a***	***b***	***c***	***z***	**EQID**	***a***	***b***	***c***	***z***
0057	0.221331	0.527736	0.021391	9	0145	0.320127	0.213792	0.076465	10
0064	1.021724	0.376252	0.168458	4	0146	0.379026	0.477325	0.079456	5
0068	0.740736	1.152547	0.272931	0	0152	0.299394	0.91847	0.27843	6.3
0069	0.520164	1.405515	0.424279	0.2	0158	1.139464	0.451427	0.077055	0
0072	0.936165	1.487385	0.230019	0	0168	0.984686	0.756766	0.332895	0
0073	0.589254	-0.17859	2.853467	2	0169	2.145449	1.470985	0.055243	0
0076	0.708679	-0.147444	0.085406	3	0171	0.518551	0.067375	0.043254	6.4
0083	1.004328	1.067161	0.170491	1	0172	1.043122	-0.680229	0.339605	6.7
0087	1.011351	1.826301	0.153362	0	0173	0.511438	0.691369	0.056374	1.5
0090	0.788576	1.134191	0.202305	0	0174	0.569555	0.124679	0.198964	7
0091	0.720221	0.566465	0.158731	8	0175	-3.805168	5	0.001794	10
0096	0.484478	1.747166	0.274033	0	0176	1.079042	0.454092	0.131948	0.5
0097	1.169409	1.087583	0.833886	2	0177	0.684477	0.91811	0.261074	2
0101	1.181736	-0.216917	0.038752	4	0178	0.614429	0.717327	0.271022	1.4
0102	0.368664	0.414556	0.152011	2	0179	1.107132	0.729474	0.251596	2
0103	0.956228	-0.113642	0.061463	4	0180	0.845726	0.714293	0.316584	4
0108	0.403674	0.358343	0.070888	5.9	0262	1.59081	-0.47502	0.090247	3.6
0111	0.854314	1.380369	0.389027	0	0274	0.836783	1.323437	0.32338	0
0113	0.614948	-0.479028	0.132068	14.5	0277	1.747446	1.187949	0.109395	0
0115	0.694814	0.937594	0.189094	0	0278	0.925459	0.676867	0.451691	3.1
0116	0.683883	0.745763	0.176598	0	0279	0.918616	0.65576	0.560713	0
0118	1.088626	0.54298	0.230968	3	0280	1.705629	1.315802	0.139997	0.6
0119	0.735299	1.626748	0.245068	0	0281	1.250044	0.683286	0.164739	0
0121	1.106969	0.205975	0.410198	3	0346	0.417792	0.398219	0.425904	0.5
0123	1.697213	-0.418702	0.067968	5.2					

The following parametric equation gives $\overline{IDP}\left(R_{jb}\right)$:

$$\overline{IDP}\left(R_{jb}\right) = a + \frac{b}{cosh\left(c\, R_{jb}\right)} \tag{E.2}$$

where coefficients *a, b,* and *c* are given in Table E.2.

Table E.2 Coefficients of parametric average IDP as function of R_{jb}

EQID	*a*	*b*	*c*	EQID	*a*	*b*	*c*
0006	1.326	0.878	0.196	0125	1.194	1.68	0.145
0012	0.981	1.199	0.158	0127	1.341	-0.346	10*
0025	0.759	1.012	0.172	0128	0.484	0.496	0.271
0028	0.918	0.815	0.222	0129	1.268	0.532	0.086
0030	0.828	0.693	0.148	0130	0.489	0.746	0.023
0031	0.618	0.181	0.187	0134	0.495	0.222	0.071
0040	1.234	-0.169	10*	0135	1.13	1.207	0.155
0041	0.826	0.862	0.091	0136	1.638	1.28	0.118
0043	0.823	0.124	0.057	0137	1.477	-0.41	10*
0045	0.649	-0.534	0.197	0138	1.322	0.101	0.103
0046	1.349	-0.356	0.623	0140	1.614	1.706	0.071
0048	0.308	0.358	0.069	0141	1.174	1.149	0.138
0050	1.203	0.848	0.182	0142	2.002	0.727	0.191
0056	0.958	-0.114	0.35	0144	1.348	0.846	0.136
0057	0.719	-0.339	0.665	0145	-0.373	0.817	0.01
0064	0.995	0.395	0.105	0146	0.316	0.541	0.056
0068	0.756	0.561	0.26	0152	0.282	0.956	0.165
0069	0.533	0.91	0.53	0158	1.13	0.397	0.071
0072	0.921	0.874	0.167	0168	0.984	0.742	0.321
0073	0.588	-0.35	2.403	0169	-1.953	5*	0.012
0076	0.664	-0.434	0.957	0171	0.582	-0.355	0.931
0083	0.998	1.031	0.165	0172	1.041	-0.885	0.256
0087	1.06	1.03	0.149	0173	0.447	0.72	0.046
0090	0.778	1.083	0.177	0174	0.6	-0.245	1.714
0091	0.061	0.844	0.018	0175	1.22	-0.843	0.561
0096	0.498	1.393	0.298	0176	1.082	0.488	0.138
0097	1.243	-0.238	10*	0177	0.642	0.544	0.118
0101	1.07	-0.452	0.195	0178	0.609	0.754	0.249
0102	0.357	0.419	0.119	0179	1.092	0.739	0.177

EQID	*a*	*b*	*c*	EQID	*a*	*b*	*c*
0103	0.93	-0.265	0.156	0180	0.945	-0.23	6.734
0108	0.323	0.416	0.044	0262	1.488	-0.708	0.587
0111	0.821	0.57	0.166	0274	0.662	0.415	0.051
0113	0.646	-0.604	0.08	0277	-0.059	2.118	0.012
0115	0.691	0.899	0.18	0278	0.99	-0.375	7.848
0116	0.684	0.75	0.177	0279	0.967	-0.229	8.007
0118	1.092	0.364	0.237	0280	1.743	1.043	0.156
0119	0.683	0.671	0.118	0281	1.249	0.598	0.204
0121	1.156	-0.056	0.03	0346	0.417	0.138	0.276
0123	1.538	-0.923	0.446				

* - integer values in the coefficients are nominal values assigned

Appendix F: Regression Analysis of Narrow-Band Isochrone Directivity Effects, Spudich and Chiou

In this appendix, we discuss the motivation for the narrow-band directivity model, which yielded the *ad hoc* model coefficients, and we subsequently discuss the development of the favored regression model, Model 3.

F.1 MOTIVATION FOR THE NARROW-BAND DIRECTIVITY MODEL

We adopted a narrow-band directivity model because we could see a correlation between the earthquake magnitude and the oscillator period at which the intra-event residuals correlated best with *IDP*. This is explained in more detail in the following sections.

In addition, there was other circumstantial evidence for narrow-band directivity. Two curious features of many older directivity models, such as Somerville et al. [1997], Abrahamson [2000], and Spudich and Chiou [2008] are that (1) all earthquakes have their peak directivity at the longest spectral periods, regardless of magnitude, and (2) earthquakes having magnitudes less than about 6.0 have very little or no directivity. Seekins and Boatwright [2010] have shown that many earthquakes of M 3.5 - 5.4 have clear directivity in their PGA and PGV, so the lack of directivity for small earthquakes in these older directivity models points to a flaw in the functional forms. Baker [2007] has shown that the presence of a directivity pulse in a record causes a peak in the spectral velocity near the period of the pulse, and it causes the long period corner of the PSA to be near the pulse period.

F.2 INITIAL EARTHQUAKE DATA SET

For our analysis, we selected all earthquakes having 4 or more recordings, reasonably distributed in azimuth, within R_{rup}= 50 km. We fit the function $A(T) + b(T)\,IDP$ to the intra-event residuals for each earthquake at each period in 0.5, 0.75, 1.0, 1.5, 2.0, 3.0, 4.0, 5.0, 7.5, 10.0 s, yielding estimates of coefficient $b(T)$ and the standard error $\sigma(T)$ of $b(T)$ estimates. In Figure F.1 we show $b(T)$ only where $|b(T)/\,\sigma(T)| > 1.5$. (Note: Figure F.2, Figure F.3, Figure F.4, and Table F.1 contain b values from our initial data exploration described above. Figure F.1 shows b values recomputed more recently by fitting the function $b(T)\ (IDP - \overline{IDP})$ to a slightly larger set of earthquakes. The new b values in Figure F.1 are very similar to the earlier ones, and we present the newer b values because we regard them as more reliable.)

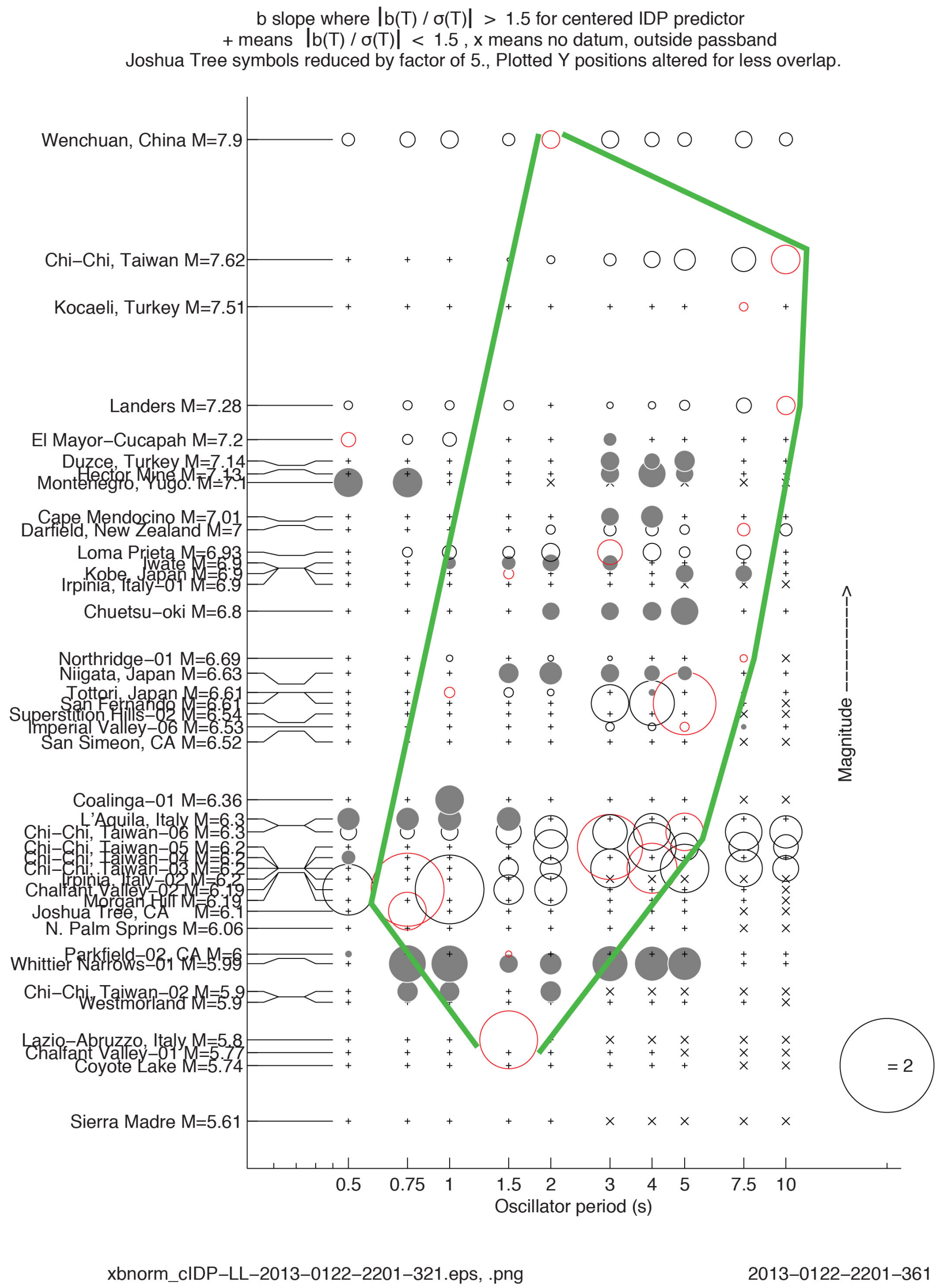

Figure F.1 **Centered *IDP* coefficient $b(T)$ for the initial earthquake data set is plotted only where $|b(T)/\sigma(T)| > 1.5$. Radius of circle is proporrtional to $b(T)$, whcre the key indicates a value of 2. Joshua Tree symbols are reduced by a factor of 5. Gray-filled circles indicate ne1gative coefficients. For each earthquake the red circle indicates the maximum (and positive) coefficient over all periods. Locus of peak values (except one) of the coefficient is indicated. × indicates periods outside the filter passband where there is no datum. + indicates no datum because $|b(T)/\sigma(T)| < 1.5$. Magnitude scale is linear, but some earthquakes' results have been shifted vertically to minimize overlap.**

The first question to address is whether these data support a "broad-band" model, in which the directivity effect continues to rise with period, or a "narrow-band" model, in which the directivity effect is peaked at some period. The easiest way to answer this question is to ask whether $b(T)$ rises monotonically for smaller earthquakes. ($b(T)$ rises monotonically for Chi-Chi to 10 sec, but this could be interpreted either as a broad-band model or a narrow-band model with peak $b(T)$ occurring at 10 sec or greater.) The Chi-Chi aftershocks 3, 5, and 6 are well recorded and show a narrow-band characteristic. Reinforcing this conclusion is inspection of the other quakes in Figure F.1. Other earthquakes not appearing broad-band are Wenchuan, El Mayor - Cucahpah, Darfield, Loma Prieta, Tottori, and Chalfant Valley-2. Four earthquakes that might be broad band are Chi-Chi*, Landers*, Northridge, and Imperial Valley (* the quake could be narrow-band with peak at T ≥ 10 sec), and three quakes are ambiguous: Kobe, Kocaeli, and Parkfield. This tally supports the narrow-band hypothesis. The convex-hull (green lines in Figure F.1) around the points with peak b slope (excluding one datum, El Mayor-Cucapah) support a narrow-band model in which the period of peak $b(T)$ increases with magnitude.

Consequently, we modeled these spectra with a narrow-band model. We did this in two steps. In the first step, explained below, we chose a subset of "good" earthquakes with a strong directivity signal, in order to develop a model functional form. In the second step, to determine model coefficients we included the data from all earthquakes having finite fault models.

To learn the period-dependence of the peak of $b(T)$, for each earthquake we picked the period T_{max} at which $b(T)$ was maximum. We then plotted the functions $b^i(T_j/T^i_{max})/b^i_{max}$ where $b^i_{max} = \max_j [b^i(T_j)] = b^i(T^i_{max})$ for $i = 1 \ldots n$ earthquakes together, i.e. we normalized $b^i(T)$ to unit amplitude and shifted for all i so that the peaks aligned for T^i_{max} and b^i_{max} (Table F.1). This superposition, shown in Figure F.2 for a subset of 12 earthquakes showing the clearest narrow-band characteristics, suggests that the period-dependence of $b(T)$ is approximately Gaussian with a width parameter of 0.4 for these quakes. The b_{max} and T_{max} shown in Figures F.3 and F.4 suggest that, to complete the functional form, we need expressions for b_{max} and T_{max} as a function of M.

Table F.1 Maximum *IDP* coefficient and period of maximum coefficient of the 21 earthquakes used to build the directivity model.

EQID	EQNAME	Mag	b_max	T_max	sig
48	CoyoteLake	5.74	0.5095	1.5	0.9051
102	ChalfantValley-01	5.77	0.5855	0.5	0.5766
179	Parkfield-02,CA	6	0.0738	2	0.0751
101	N.Palm Springs	6.06	0.2091	1	0.1928
90	MorganHill	6.19	0.1146	0.75	0.0929
103	ChalfantValley-02	6.19	1.5273	0.75	0.4413
172	Chi-chi,Taiwan-03	6.2	1.0128	4	0.1413
173	Chi-chi,Taiwan-04	6.2	0.1406	1	0.1689
174	Chi-chi,Taiwan-05	6.2	1.3579	3	0.2976
175	Chi-chi,Taiwan-06	6.3	0.9058	4	0.1034
50	ImperialValley-06	6.53	0.1924	3	0.0931
116	SuperstitionHills-02	6.54	0.245	2	0.1906
30	SanFernando	6.61	0.8641	7.5	0.4646
176	Tottori,Japan	6.61	0.2644	1	0.0968
127	Northridge-01	6.69	0.2062	3	0.064
129	Kobe,Japan	6.9	0.1905	1.5	0.1573
118	LomaPrieta	6.93	0.514	3	0.0856
281	Darfield,New Zealand	7	0.2808	7.5	0.0917
125	Landers	7.28	0.4692	10	0.1138
136	Kocaeli, Turkey	7.51	0.3385	7.5	0.0959
137	Chi-chi,Taiwan	7.62	0.6032	10	0.0508

$$b/b_{\max} = e^{-[\log_{10}(T/T_{\max})]^2/2(0.4)^2}$$

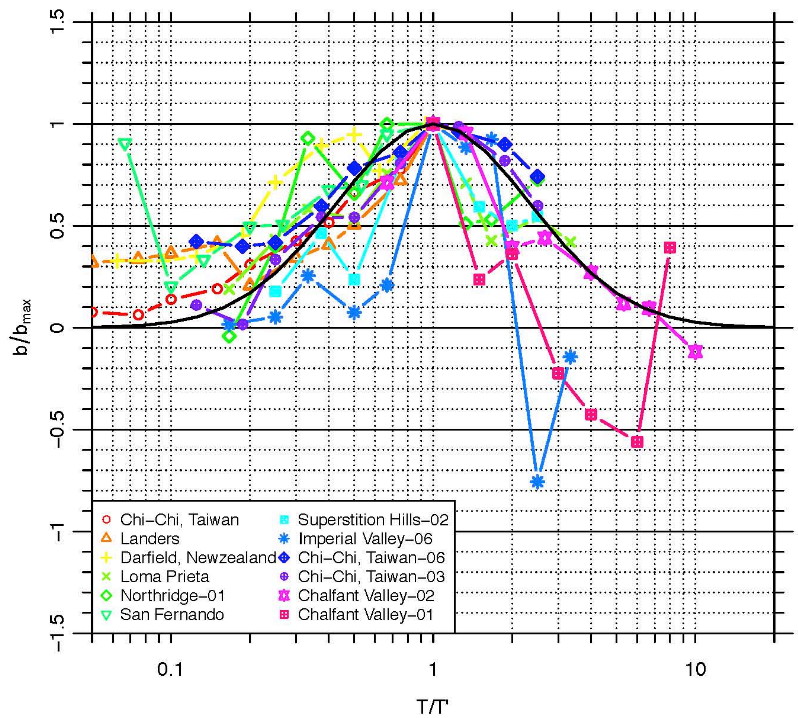

Figure F.2 Alignment of peaks of *b(T)* (colored lines) with Gaussian (black line).

F.3 RESTRICTED EARTHQUAKE DATA SET

Thirty-six earthquakes in NGA-2 database have a finite fault model and produce at least five recordings. Among them, 21 earthquakes exhibit good azimuthal coverage and apparent directivity; this subset of 21 good earthquakes is used in this analysis to build the functional forms for b_{max} and T_{max}.

The high apparent directivity of the Chi-Chi main shock and its aftershocks might be biased high. Note in Table F.1 that these quakes tend to have high values of b_{max}. During the prepartion of this report one of us (B. Chiou) performed a regression in which the site terms for the Chi-Chi stations were obtained. These terms correlated well with an apparent directivity signal. Consequently, the directivity estimated for individual Chi-Chi quakes might be overestimated.

F.4 BUILDING EXPRESSIONS FOR B_{MAX} AND T_{MAX} (MODEL 1, AD HOC MODEL)

Based on the variation of b_{max} with magnitude, we chose to model $b_{max}(M)$ as a two-segment line having a flat slope at low magnitude and a positive slope at high magnitude (Figure F.3).

$$b_{\max} = 0.2785 + 0.1655 \ \max(M - 6.2,\ 0)$$

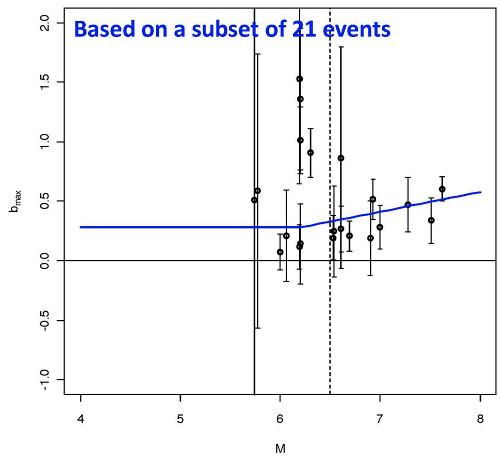

Figure F.3 Blue line is inferred functional form of b_{max}. Data points are from Table F.1.

Similarly, based on Figure F.4, we chose to model T_{max} as a linear function of M.

Ad hoc model (model 1) functional form

$$\log_{10}(T_{\max}) = -3.1884 + 0.5479M$$

Based on a subset of 21 events

In the regression model (model 2) (later) the functional form is the same but the coefficients change

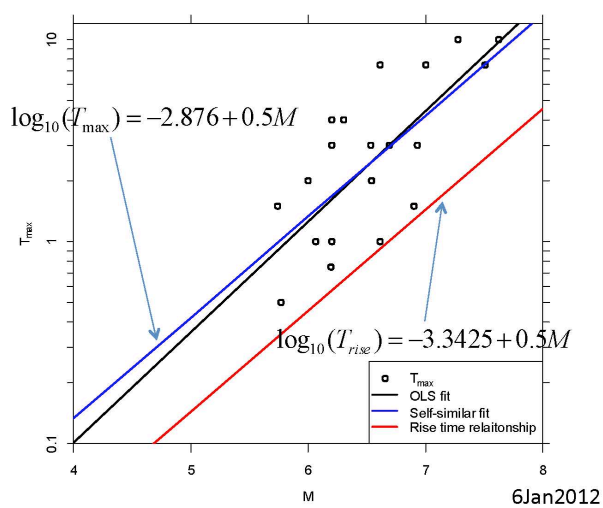

Figure F.4 Black line: Fitted line for T_{max}. Blue line: Self-similar fit (0.5M) for T_{max}. Red line: Self-similar rise times from Somerville [2003].

F.5 REGRESSION APPROACH (MODEL 3)

To estimate model coefficients directly from the residual data, we performed a regression.

Coefficients c_1, c_2, c_3, c_4, c_5, and g of Equation (5.1) are period independent, therefore these coefficients are estimated by a joint regression with combined data of all periods. Correlation between residual data at different neighboring periods is ignored in the regression analysis.

The lowest magnitude of the good earthquake set is 5.7. The lack of small-magnitude data renders coefficients c_1 and c_2 (which define the directivity at moderate to small magnitude) inseparable from each other. In the regression analysis, we fix c_1 and estimate c_2.

We conduct regression for a set of plausible c_1 values, ranging from 5.7 (the minimum M of the dataset) to 6.2 (the eyeballed best value from Figure F.3). The value 5.7 yields the highest likelihood among the test values. We thus take the regression model with c_1 fixed to 5.7 (Model 3) as our favored model. Coefficients are given in Table 5.1.

Appendix G: Definition of the IDP and Related Quantities, Chiou and Spudich Predictor

This appendix briefly recapitulates the most important parts of the derivations in Spudich et al. [2004] and Spudich and Chiou [2008]. Let $\mathbf{x}$ be a point on a rupturing fault, and let $t_r(\mathbf{x})$ be the time that point $\mathbf{x}$ ruptures. Directivity is to be evaluated at a site $\mathbf{x}_s$ on the ground surface. Let the S-wave travel time from $\mathbf{x}$ to $\mathbf{x}_s$ be $t_S(\mathbf{x},\mathbf{x}_s)$. The S wave liberated from $\mathbf{x}$ arrives at $\mathbf{x}_s$ at time $t_a(\mathbf{x},\mathbf{x}_s) = t_r(\mathbf{x}) + t_S(\mathbf{x},\mathbf{x}_s)$. The S wave liberated from the hypocenter $\mathbf{x}_h$ arrives at $\mathbf{x}_s$ at time $t_a(\mathbf{x}_h,\mathbf{x}_S)$. If D is the distance on the fault from $\mathbf{x}_h$ to $\mathbf{x}$, then all the S waves radiated between those two points arrive in time interval $t_a(\mathbf{x}) - t_a(\mathbf{x}_h)$, and clearly $\bar{c} := \dfrac{D}{t_a(\mathbf{x}) - t_a(\mathbf{x}_h)}$ is a measure of the rate at which 'signal' from the fault arrives at the site. It is a measure of directivity. If $\mathbf{x}$ is the closest point $\mathbf{x}_C$ on the fault to the site, then $\bar{c}/v_S = \tilde{c}'$, the directivity measure used in the *IDP*. If $\mathbf{x}$ is the direct point $\mathbf{x}_D$ on the fault to the site, then $\bar{c}/v_S = \hat{c}'$, , the directivity measure used in the *DDP*. If we assume the Earth is a uniform wholespace with shear speed v_S, and we assume that rupture speed is 0.8 of the shear wave speed, we can arrive at the definition of $\hat{c}'$given earlier in this paper.

The *IDP* is defined by $IDP = C\ S\ R_{ri}$ where

$$C = \frac{min(\tilde{c}', 2.45) - 0.8}{(2.45 - 0.8)} \tag{G.1}$$

$$S = ln\left[min(75, max(s,h))\right] \tag{G.2}$$

All the above terms are evaluated at a site $\mathbf{x}_S$. s is the along-strike distance in km from the hypocenter $\mathbf{x}_h$ to the point $\mathbf{x}_c$ on the fault closest to the site, and h is the down-dip distance in km from the top of the rupture to the hypocenter. C is a normalized form of $\tilde{c}'$, lying in the range [0,1]. R_{ri} is a scalar point source radiation pattern amplitude ranging from 0 to about 1.

PEER REPORTS

PEER reports are available as a free PDF download from http://peer.berkeley.edu/publications/peer_reports_complete.html. Printed hard copies of PEER reports can be ordered directly from our printer by following the instructions at http://peer.berkeley.edu/publications/peer_reports.html. For other related questions about the PEER Report Series, contact the Pacific Earthquake Engineering Research Center, 325 Davis Hall mail code 1792, Berkeley, CA 94720. Tel.: (510) 642-3437; Fax: (510) 665-1655; Email: peer_editor@berkeley.edu

PEER 2013/09 *Final Report of the NGA-West2 Directivity Working Group.* Paul Spudich, Jeffrey R. Bayless, Jack W. Baker, Brian S.J. Chiou, Badie Rowshandel, Shrey K. Shahi, and Paul Somerville. May 2013.

PEER 2013/08 *NGA-West2 Model for Estimating Average Horizontal Values of Pseudo-Absolute Spectral Accelerations Generated by Crustal Earthquakes.* I. M. Idriss. May 2013.

PEER 2013/07 *Update of the Chiou and Youngs NGA Ground Motion Model for Average Horizontal Component of Peak Ground Motion and Response Spectra.* Brian S.J. Chiou and Robert R. Youngs. May 2013.

PEER 2013/06 *NGA-West2 Campbell-Bozorgnia Ground Motion Model for the Horizontal Components of PGA, PGV, and 5%-Damped Elastic Pseudo-Acceleration Response Spectra for Periods Ranging from 0.01 to 10 sec.* Kenneth W. Campbell and Yousef Bozorgnia. May 2013.

PEER 2013/05 *NGA-West2 Equations for Predicting Response Spectral Accelerations for Shallow Crustal Earthquakes.* David M. Boore, Jonathan P. Stewart, Emel Seyhan, Gail M. Atkinson. May 2013.

PEER 2013/04 *Update of the AS08 Ground-Motion Prediction Equations Based on the NGA-West2 Data Set.* Norman SA. Abrahamson, Walter J. Silva, and Ronnie Kamai. May 2013.

PEER 2013/03 *PEER NGA-West2 Database.* Timothy D. Ancheta, Robert B. Darragh, Jonathan P. Stewart, Emel Seyhan, Walter J. Silva, Brian S.J. Chiou, Katie E. Wooddell, Robert W. Graves, Albert R. Kottke, David M. Boore, Tadahiro Kishida, and Jennifer L. Donahue. May 2013.

PEER 2013/02 *Hybrid Simulation of the Seismic Response of Squat Reinforced Concrete Shear Walls.* Catherine A. Whyte and Bozidar Stojadinovic. May 2013.

PEER 2013/01 *Housing Recovery in Chile: A Qualitative Mid-program Review.* Mary C. Comerio. February 2013.

PEER 2012/08 *Guidelines for Estimation of Shear Wave Velocity.* Bernard R. Wair, Jason T. DeJong, and Thomas Shantz. December 2012.

PEER 2012/07 *Earthquake Engineering for Resilient Communities: 2012 PEER Internship Program Research Report Collection.* Heidi Tremayne (Editor), Stephen A. Mahin (Editor), Collin Anderson, Dustin Cook, Michael Erceg, Carlos Esparza, Jose Jimenez, Dorian Krausz, Andrew Lo, Stephanie Lopez, Nicole McCurdy, Paul Shipman, Alexander Strum, Eduardo Vega. December 2012.

PEER 2012/06 *Fragilities for Precarious Rocks at Yucca Mountain.* Matthew D. Purvance, Rasool Anooshehpoor, and James N. Brune. December 2012.

PEER 2012/05 *Development of Simplified Analysis Procedure for Piles in Laterally Spreading Layered Soils.* Christopher R. McGann, Pedro Arduino, and Peter Mackenzie–Helnwein. December 2012.

PEER 2012/04 *Unbonded Pre-Tensioned Columns for Bridges in Seismic Regions.* Phillip M. Davis, Todd M. Janes, Marc O. Eberhard, and John F. Stanton. December 2012.

PEER 2012/03 *Experimental and Analytical Studies on Reinforced Concrete Buildings with Seismically Vulnerable Beam-Column Joints.* Sangjoon Park and Khalid M. Mosalam. October 2012.

PEER 2012/02 *Seismic Performance of Reinforced Concrete Bridges Allowed to Uplift during Multi-Directional Excitation.* Andres Oscar Espinoza and Stephen A. Mahin. July 2012.

PEER 2012/01 *Spectral Damping Scaling Factors for Shallow Crustal Earthquakes in Active Tectonic Regions.* Sanaz Rezaeian, Yousef Bozorgnia, I. M. Idriss, Kenneth Campbell, Norman Abrahamson, and Walter Silva. July 2012.

PEER 2011/10 *Earthquake Engineering for Resilient Communities: 2011 PEER Internship Program Research Report Collection.* Eds. Heidi Faison and Stephen A. Mahin. December 2011.

PEER 2011/09 *Calibration of Semi-Stochastic Procedure for Simulating High-Frequency Ground Motions.* Jonathan P. Stewart, Emel Seyhan, and Robert W. Graves. December 2011.

PEER 2011/08 *Water Supply in regard to Fire Following Earthquake.* Charles Scawthorn. November 2011.

PEER 2011/07 *Seismic Risk Management in Urban Areas. Proceedings of a U.S.-Iran-Turkey Seismic Workshop.* September 2011.

PEER 2011/06 *The Use of Base Isolation Systems to Achieve Complex Seismic Performance Objectives.* Troy A. Morgan and Stephen A. Mahin. July 2011.

PEER 2011/05 *Case Studies of the Seismic Performance of Tall Buildings Designed by Alternative Means.* Task 12 Report for the Tall Buildings Initiative. Jack Moehle, Yousef Bozorgnia, Nirmal Jayaram, Pierson Jones, Mohsen Rahnama, Nilesh Shome, Zeynep Tuna, John Wallace, Tony Yang, and Farzin Zareian. July 2011.

PEER 2011/04 *Recommended Design Practice for Pile Foundations in Laterally Spreading Ground.* Scott A. Ashford, Ross W. Boulanger, and Scott J. Brandenberg. June 2011.

PEER 2011/03 *New Ground Motion Selection Procedures and Selected Motions for the PEER Transportation Research Program.* Jack W. Baker, Ting Lin, Shrey K. Shahi, and Nirmal Jayaram. March 2011.

PEER 2011/02 *A Bayesian Network Methodology for Infrastructure Seismic Risk Assessment and Decision Support.* Michelle T. Bensi, Armen Der Kiureghian, and Daniel Straub. March 2011.

PEER 2011/01 *Demand Fragility Surfaces for Bridges in Liquefied and Laterally Spreading Ground.* Scott J. Brandenberg, Jian Zhang, Pirooz Kashighandi, Yili Huo, and Minxing Zhao. March 2011.

PEER 2010/05 *Guidelines for Performance-Based Seismic Design of Tall Buildings*. Developed by the Tall Buildings Initiative. November 2010.

PEER 2010/04 *Application Guide for the Design of Flexible and Rigid Bus Connections between Substation Equipment Subjected to Earthquakes.* Jean-Bernard Dastous and Armen Der Kiureghian. September 2010.

PEER 2010/03 *Shear Wave Velocity as a Statistical Function of Standard Penetration Test Resistance and Vertical Effective Stress at Caltrans Bridge Sites.* Scott J. Brandenberg, Naresh Bellana, and Thomas Shantz. June 2010.

PEER 2010/02 *Stochastic Modeling and Simulation of Ground Motions for Performance-Based Earthquake Engineering.* Sanaz Rezaeian and Armen Der Kiureghian. June 2010.

PEER 2010/01 *Structural Response and Cost Characterization of Bridge Construction Using Seismic Performance Enhancement Strategies.* Ady Aviram, Božidar Stojadinović, Gustavo J. Parra-Montesinos, and Kevin R. Mackie. March 2010.

PEER 2009/03 *The Integration of Experimental and Simulation Data in the Study of Reinforced Concrete Bridge Systems Including Soil-Foundation-Structure Interaction.* Matthew Dryden and Gregory L. Fenves. November 2009.

PEER 2009/02 *Improving Earthquake Mitigation through Innovations and Applications in Seismic Science, Engineering, Communication, and Response. Proceedings of a U.S.-Iran Seismic Workshop.* October 2009.

PEER 2009/01 *Evaluation of Ground Motion Selection and Modification Methods: Predicting Median Interstory Drift Response of Buildings.* Curt B. Haselton, Ed. June 2009.

PEER 2008/10 *Technical Manual for Strata.* Albert R. Kottke and Ellen M. Rathje. February 2009.

PEER 2008/09 *NGA Model for Average Horizontal Component of Peak Ground Motion and Response Spectra.* Brian S.-J. Chiou and Robert R. Youngs. November 2008.

PEER 2008/08 *Toward Earthquake-Resistant Design of Concentrically Braced Steel Structures.* Patxi Uriz and Stephen A. Mahin. November 2008.

PEER 2008/07 *Using OpenSees for Performance-Based Evaluation of Bridges on Liquefiable Soils.* Stephen L. Kramer, Pedro Arduino, and HyungSuk Shin. November 2008.

PEER 2008/06 *Shaking Table Tests and Numerical Investigation of Self-Centering Reinforced Concrete Bridge Columns.* Hyung IL Jeong, Junichi Sakai, and Stephen A. Mahin. September 2008.

PEER 2008/05 *Performance-Based Earthquake Engineering Design Evaluation Procedure for Bridge Foundations Undergoing Liquefaction-Induced Lateral Ground Displacement.* Christian A. Ledezma and Jonathan D. Bray. August 2008.

PEER 2008/04 *Benchmarking of Nonlinear Geotechnical Ground Response Analysis Procedures.* Jonathan P. Stewart, Annie On-Lei Kwok, Yousseff M. A. Hashash, Neven Matasovic, Robert Pyke, Zhiliang Wang, and Zhaohui Yang. August 2008.

PEER 2008/03 *Guidelines for Nonlinear Analysis of Bridge Structures in California.* Ady Aviram, Kevin R. Mackie, and Božidar Stojadinović. August 2008.

PEER 2008/02 *Treatment of Uncertainties in Seismic-Risk Analysis of Transportation Systems.* Evangelos Stergiou and Anne S. Kiremidjian. July 2008.

PEER 2008/01 *Seismic Performance Objectives for Tall Buildings.* William T. Holmes, Charles Kircher, William Petak, and Nabih Youssef. August 2008.

PEER 2007/12 *An Assessment to Benchmark the Seismic Performance of a Code-Conforming Reinforced Concrete Moment-Frame Building.* Curt Haselton, Christine A. Goulet, Judith Mitrani-Reiser, James L. Beck, Gregory G. Deierlein, Keith A. Porter, Jonathan P. Stewart, and Ertugrul Taciroglu. August 2008.

PEER 2007/11 *Bar Buckling in Reinforced Concrete Bridge Columns.* Wayne A. Brown, Dawn E. Lehman, and John F. Stanton. February 2008.

PEER 2007/10 *Computational Modeling of Progressive Collapse in Reinforced Concrete Frame Structures.* Mohamed M. Talaat and Khalid M. Mosalam. May 2008.

PEER 2007/09 *Integrated Probabilistic Performance-Based Evaluation of Benchmark Reinforced Concrete Bridges.* Kevin R. Mackie, John-Michael Wong, and Božidar Stojadinović. January 2008.

PEER 2007/08 *Assessing Seismic Collapse Safety of Modern Reinforced Concrete Moment-Frame Buildings.* Curt B. Haselton and Gregory G. Deierlein. February 2008.

PEER 2007/07 *Performance Modeling Strategies for Modern Reinforced Concrete Bridge Columns.* Michael P. Berry and Marc O. Eberhard. April 2008.

PEER 2007/06 *Development of Improved Procedures for Seismic Design of Buried and Partially Buried Structures.* Linda Al Atik and Nicholas Sitar. June 2007.

PEER 2007/05 *Uncertainty and Correlation in Seismic Risk Assessment of Transportation Systems.* Renee G. Lee and Anne S. Kiremidjian. July 2007.

PEER 2007/04 *Numerical Models for Analysis and Performance-Based Design of Shallow Foundations Subjected to Seismic Loading.* Sivapalan Gajan, Tara C. Hutchinson, Bruce L. Kutter, Prishati Raychowdhury, José A. Ugalde, and Jonathan P. Stewart. May 2008.

PEER 2007/03 *Beam-Column Element Model Calibrated for Predicting Flexural Response Leading to Global Collapse of RC Frame Buildings.* Curt B. Haselton, Abbie B. Liel, Sarah Taylor Lange, and Gregory G. Deierlein. May 2008.

PEER 2007/02 *Campbell-Bozorgnia NGA Ground Motion Relations for the Geometric Mean Horizontal Component of Peak and Spectral Ground Motion Parameters.* Kenneth W. Campbell and Yousef Bozorgnia. May 2007.

PEER 2007/01 *Boore-Atkinson NGA Ground Motion Relations for the Geometric Mean Horizontal Component of Peak and Spectral Ground Motion Parameters.* David M. Boore and Gail M. Atkinson. May. May 2007.

PEER 2006/12 *Societal Implications of Performance-Based Earthquake Engineering.* Peter J. May. May 2007.

PEER 2006/11 *Probabilistic Seismic Demand Analysis Using Advanced Ground Motion Intensity Measures, Attenuation Relationships, and Near-Fault Effects.* Polsak Tothong and C. Allin Cornell. March 2007.

PEER 2006/10 *Application of the PEER PBEE Methodology to the I-880 Viaduct.* Sashi Kunnath. February 2007.

PEER 2006/09 *Quantifying Economic Losses from Travel Forgone Following a Large Metropolitan Earthquake.* James Moore, Sungbin Cho, Yue Yue Fan, and Stuart Werner. November 2006.

PEER 2006/08 *Vector-Valued Ground Motion Intensity Measures for Probabilistic Seismic Demand Analysis.* Jack W. Baker and C. Allin Cornell. October 2006.

PEER 2006/07 *Analytical Modeling of Reinforced Concrete Walls for Predicting Flexural and Coupled–Shear-Flexural Responses.* Kutay Orakcal, Leonardo M. Massone, and John W. Wallace. October 2006.

PEER 2006/06 *Nonlinear Analysis of a Soil-Drilled Pier System under Static and Dynamic Axial Loading.* Gang Wang and Nicholas Sitar. November 2006.

PEER 2006/05 *Advanced Seismic Assessment Guidelines.* Paolo Bazzurro, C. Allin Cornell, Charles Menun, Maziar Motahari, and Nicolas Luco. September 2006.

PEER 2006/04 *Probabilistic Seismic Evaluation of Reinforced Concrete Structural Components and Systems.* Tae Hyung Lee and Khalid M. Mosalam. August 2006.

PEER 2006/03 *Performance of Lifelines Subjected to Lateral Spreading.* Scott A. Ashford and Teerawut Juirnarongrit. July 2006.

PEER 2006/02 *Pacific Earthquake Engineering Research Center Highway Demonstration Project.* Anne Kiremidjian, James Moore, Yue Yue Fan, Nesrin Basoz, Ozgur Yazali, and Meredith Williams. April 2006.

PEER 2006/01 *Bracing Berkeley. A Guide to Seismic Safety on the UC Berkeley Campus.* Mary C. Comerio, Stephen Tobriner, and Ariane Fehrenkamp. January 2006.

PEER 2005/16 *Seismic Response and Reliability of Electrical Substation Equipment and Systems.* Junho Song, Armen Der Kiureghian, and Jerome L. Sackman. April 2006.

PEER 2005/15 *CPT-Based Probabilistic Assessment of Seismic Soil Liquefaction Initiation.* R. E. S. Moss, R. B. Seed, R. E. Kayen, J. P. Stewart, and A. Der Kiureghian. April 2006.

PEER 2005/14 *Workshop on Modeling of Nonlinear Cyclic Load-Deformation Behavior of Shallow Foundations.* Bruce L. Kutter, Geoffrey Martin, Tara Hutchinson, Chad Harden, Sivapalan Gajan, and Justin Phalen. March 2006.

PEER 2005/13 *Stochastic Characterization and Decision Bases under Time-Dependent Aftershock Risk in Performance-Based Earthquake Engineering.* Gee Liek Yeo and C. Allin Cornell. July 2005.

PEER 2005/12 *PEER Testbed Study on a Laboratory Building: Exercising Seismic Performance Assessment.* Mary C. Comerio, editor. November 2005.

PEER 2005/11 *Van Nuys Hotel Building Testbed Report: Exercising Seismic Performance Assessment.* Helmut Krawinkler, editor. October 2005.

PEER 2005/10 *First NEES/E-Defense Workshop on Collapse Simulation of Reinforced Concrete Building Structures.* September 2005.

PEER 2005/09 *Test Applications of Advanced Seismic Assessment Guidelines.* Joe Maffei, Karl Telleen, Danya Mohr, William Holmes, and Yuki Nakayama. August 2006.

PEER 2005/08 *Damage Accumulation in Lightly Confined Reinforced Concrete Bridge Columns.* R. Tyler Ranf, Jared M. Nelson, Zach Price, Marc O. Eberhard, and John F. Stanton. April 2006.

PEER 2005/07 *Experimental and Analytical Studies on the Seismic Response of Freestanding and Anchored Laboratory Equipment*. Dimitrios Konstantinidis and Nicos Makris. January 2005.

PEER 2005/06 *Global Collapse of Frame Structures under Seismic Excitations*. Luis F. Ibarra and Helmut Krawinkler. September 2005.

PEER 2005//05 *Performance Characterization of Bench- and Shelf-Mounted Equipment.* Samit Ray Chaudhuri and Tara C. Hutchinson. May 2006.

PEER 2005/04 *Numerical Modeling of the Nonlinear Cyclic Response of Shallow Foundations.* Chad Harden, Tara Hutchinson, Geoffrey R. Martin, and Bruce L. Kutter. August 2005.

PEER 2005/03 *A Taxonomy of Building Components for Performance-Based Earthquake Engineering.* Keith A. Porter. September 2005.

PEER 2005/02 *Fragility Basis for California Highway Overpass Bridge Seismic Decision Making*. Kevin R. Mackie and Božidar Stojadinović. June 2005.

PEER 2005/01 *Empirical Characterization of Site Conditions on Strong Ground Motion.* Jonathan P. Stewart, Yoojoong Choi, and Robert W. Graves. June 2005.

PEER 2004/09 *Electrical Substation Equipment Interaction: Experimental Rigid Conductor Studies.* Christopher Stearns and André Filiatrault. February 2005.

PEER 2004/08 *Seismic Qualification and Fragility Testing of Line Break 550-kV Disconnect Switches.* Shakhzod M. Takhirov, Gregory L. Fenves, and Eric Fujisaki. January 2005.

PEER 2004/07 *Ground Motions for Earthquake Simulator Qualification of Electrical Substation Equipment.* Shakhzod M. Takhirov, Gregory L. Fenves, Eric Fujisaki, and Don Clyde. January 2005.

PEER 2004/06 *Performance-Based Regulation and Regulatory Regimes.* Peter J. May and Chris Koski. September 2004.

PEER 2004/05 *Performance-Based Seismic Design Concepts and Implementation: Proceedings of an International Workshop.* Peter Fajfar and Helmut Krawinkler, editors. September 2004.

PEER 2004/04 *Seismic Performance of an Instrumented Tilt-up Wall Building.* James C. Anderson and Vitelmo V. Bertero. July 2004.

PEER 2004/03 *Evaluation and Application of Concrete Tilt-up Assessment Methodologies.* Timothy Graf and James O. Malley. October 2004.

PEER 2004/02 *Analytical Investigations of New Methods for Reducing Residual Displacements of Reinforced Concrete Bridge Columns.* Junichi Sakai and Stephen A. Mahin. August 2004.

PEER 2004/01 *Seismic Performance of Masonry Buildings and Design Implications.* Kerri Anne Taeko Tokoro, James C. Anderson, and Vitelmo V. Bertero. February 2004.

PEER 2003/18 *Performance Models for Flexural Damage in Reinforced Concrete Columns.* Michael Berry and Marc Eberhard. August 2003.

PEER 2003/17 *Predicting Earthquake Damage in Older Reinforced Concrete Beam-Column Joints.* Catherine Pagni and Laura Lowes. October 2004.

PEER 2003/16 *Seismic Demands for Performance-Based Design of Bridges.* Kevin Mackie and Božidar Stojadinović. August 2003.

PEER 2003/15 *Seismic Demands for Nondeteriorating Frame Structures and Their Dependence on Ground Motions.* Ricardo Antonio Medina and Helmut Krawinkler. May 2004.

PEER 2003/14 *Finite Element Reliability and Sensitivity Methods for Performance-Based Earthquake Engineering.* Terje Haukaas and Armen Der Kiureghian. April 2004.

PEER 2003/13 *Effects of Connection Hysteretic Degradation on the Seismic Behavior of Steel Moment-Resisting Frames.* Janise E. Rodgers and Stephen A. Mahin. March 2004.

PEER 2003/12 *Implementation Manual for the Seismic Protection of Laboratory Contents: Format and Case Studies.* William T. Holmes and Mary C. Comerio. October 2003.

PEER 2003/11 *Fifth U.S.-Japan Workshop on Performance-Based Earthquake Engineering Methodology for Reinforced Concrete Building Structures.* February 2004.

PEER 2003/10 *A Beam-Column Joint Model for Simulating the Earthquake Response of Reinforced Concrete Frames.* Laura N. Lowes, Nilanjan Mitra, and Arash Altoontash. February 2004.

PEER 2003/09 *Sequencing Repairs after an Earthquake: An Economic Approach.* Marco Casari and Simon J. Wilkie. April 2004.

PEER 2003/08 *A Technical Framework for Probability-Based Demand and Capacity Factor Design (DCFD) Seismic Formats.* Fatemeh Jalayer and C. Allin Cornell. November 2003.

PEER 2003/07 *Uncertainty Specification and Propagation for Loss Estimation Using FOSM Methods.* Jack W. Baker and C. Allin Cornell. September 2003.

PEER 2003/06 *Performance of Circular Reinforced Concrete Bridge Columns under Bidirectional Earthquake Loading*. Mahmoud M. Hachem, Stephen A. Mahin, and Jack P. Moehle. February 2003.

PEER 2003/05 *Response Assessment for Building-Specific Loss Estimation.* Eduardo Miranda and Shahram Taghavi. September 2003.

PEER 2003/04 *Experimental Assessment of Columns with Short Lap Splices Subjected to Cyclic Loads*. Murat Melek, John W. Wallace, and Joel Conte. April 2003.

PEER 2003/03 *Probabilistic Response Assessment for Building-Specific Loss Estimation.* Eduardo Miranda and Hesameddin Aslani. September 2003.

PEER 2003/02 *Software Framework for Collaborative Development of Nonlinear Dynamic Analysis Program.* Jun Peng and Kincho H. Law. September 2003.

PEER 2003/01 *Shake Table Tests and Analytical Studies on the Gravity Load Collapse of Reinforced Concrete Frames.* Kenneth John Elwood and Jack P. Moehle. November 2003.

PEER 2002/24 *Performance of Beam to Column Bridge Joints Subjected to a Large Velocity Pulse.* Natalie Gibson, André Filiatrault, and Scott A. Ashford. April 2002.

PEER 2002/23 *Effects of Large Velocity Pulses on Reinforced Concrete Bridge Columns.* Greg L. Orozco and Scott A. Ashford. April 2002.

PEER 2002/22 *Characterization of Large Velocity Pulses for Laboratory Testing.* Kenneth E. Cox and Scott A. Ashford. April 2002.

PEER 2002/21 *Fourth U.S.-Japan Workshop on Performance-Based Earthquake Engineering Methodology for Reinforced Concrete Building Structures*. December 2002.

PEER 2002/20 *Barriers to Adoption and Implementation of PBEE Innovations.* Peter J. May. August 2002.

PEER 2002/19 *Economic-Engineered Integrated Models for Earthquakes: Socioeconomic Impacts.* Peter Gordon, James E. Moore II, and Harry W. Richardson. July 2002.

PEER 2002/18 *Assessment of Reinforced Concrete Building Exterior Joints with Substandard Details.* Chris P. Pantelides, Jon Hansen, Justin Nadauld, and Lawrence D. Reaveley. May 2002.

PEER 2002/17 *Structural Characterization and Seismic Response Analysis of a Highway Overcrossing Equipped with Elastomeric Bearings and Fluid Dampers: A Case Study.* Nicos Makris and Jian Zhang. November 2002.

PEER 2002/16 *Estimation of Uncertainty in Geotechnical Properties for Performance-Based Earthquake Engineering.* Allen L. Jones, Steven L. Kramer, and Pedro Arduino. December 2002.

PEER 2002/15 *Seismic Behavior of Bridge Columns Subjected to Various Loading Patterns.* Asadollah Esmaeily-Gh. and Yan Xiao. December 2002.

PEER 2002/14 *Inelastic Seismic Response of Extended Pile Shaft Supported Bridge Structures.* T.C. Hutchinson, R.W. Boulanger, Y.H. Chai, and I.M. Idriss. December 2002.

PEER 2002/13 *Probabilistic Models and Fragility Estimates for Bridge Components and Systems.* Paolo Gardoni, Armen Der Kiureghian, and Khalid M. Mosalam. June 2002.

PEER 2002/12 *Effects of Fault Dip and Slip Rake on Near-Source Ground Motions: Why Chi-Chi Was a Relatively Mild M7.6 Earthquake.* Brad T. Aagaard, John F. Hall, and Thomas H. Heaton. December 2002.

PEER 2002/11 *Analytical and Experimental Study of Fiber-Reinforced Strip Isolators*. James M. Kelly and Shakhzod M. Takhirov. September 2002.

PEER 2002/10 *Centrifuge Modeling of Settlement and Lateral Spreading with Comparisons to Numerical Analyses***.** Sivapalan Gajan and Bruce L. Kutter. January 2003.

PEER 2002/09 *Documentation and Analysis of Field Case Histories of Seismic Compression during the 1994 Northridge, California, Earthquake.* Jonathan P. Stewart, Patrick M. Smith, Daniel H. Whang, and Jonathan D. Bray. October 2002.

PEER 2002/08 *Component Testing, Stability Analysis and Characterization of Buckling-Restrained Unbonded Braces™.* Cameron Black, Nicos Makris, and Ian Aiken. September 2002.

PEER 2002/07 *Seismic Performance of Pile-Wharf Connections.* Charles W. Roeder, Robert Graff, Jennifer Soderstrom, and Jun Han Yoo. December 2001.

PEER 2002/06 *The Use of Benefit-Cost Analysis for Evaluation of Performance-Based Earthquake Engineering Decisions*. Richard O. Zerbe and Anthony Falit-Baiamonte. September 2001.

PEER 2002/05 *Guidelines, Specifications, and Seismic Performance Characterization of Nonstructural Building Components and Equipment*. André Filiatrault, Constantin Christopoulos, and Christopher Stearns. September 2001.

PEER 2002/04 *Consortium of Organizations for Strong-Motion Observation Systems and the Pacific Earthquake Engineering Research Center Lifelines Program: Invited Workshop on Archiving and Web Dissemination of Geotechnical Data, 4–5 October 2001*. September 2002.

PEER 2002/03 *Investigation of Sensitivity of Building Loss Estimates to Major Uncertain Variables for the Van Nuys Testbed.* Keith A. Porter, James L. Beck, and Rustem V. Shaikhutdinov. August 2002.

PEER 2002/02 *The Third U.S.-Japan Workshop on Performance-Based Earthquake Engineering Methodology for Reinforced Concrete Building Structures*. July 2002.

PEER 2002/01 *Nonstructural Loss Estimation: The UC Berkeley Case Study.* Mary C. Comerio and John C. Stallmeyer. December 2001.

PEER 2001/16 *Statistics of SDF-System Estimate of Roof Displacement for Pushover Analysis of Buildings.* Anil K. Chopra, Rakesh K. Goel, and Chatpan Chintanapakdee. December 2001.

PEER 2001/15 *Damage to Bridges during the 2001 Nisqually Earthquake.* R. Tyler Ranf, Marc O. Eberhard, and Michael P. Berry. November 2001.

PEER 2001/14 *Rocking Response of Equipment Anchored to a Base Foundation.* Nicos Makris and Cameron J. Black. September 2001.

PEER 2001/13 *Modeling Soil Liquefaction Hazards for Performance-Based Earthquake Engineering.* Steven L. Kramer and Ahmed-W. Elgamal. February 2001.

PEER 2001/12 *Development of Geotechnical Capabilities in OpenSees.* Boris Jeremić. September 2001.

PEER 2001/11 *Analytical and Experimental Study of Fiber-Reinforced Elastomeric Isolators*. James M. Kelly and Shakhzod M. Takhirov. September 2001.

PEER 2001/10 *Amplification Factors for Spectral Acceleration in Active Regions.* Jonathan P. Stewart, Andrew H. Liu, Yoojoong Choi, and Mehmet B. Baturay. December 2001.

PEER 2001/09 *Ground Motion Evaluation Procedures for Performance-Based Design.* Jonathan P. Stewart, Shyh-Jeng Chiou, Jonathan D. Bray, Robert W. Graves, Paul G. Somerville, and Norman A. Abrahamson. September 2001.

PEER 2001/08 *Experimental and Computational Evaluation of Reinforced Concrete Bridge Beam-Column Connections for Seismic Performance.* Clay J. Naito, Jack P. Moehle, and Khalid M. Mosalam. November 2001.

PEER 2001/07 *The Rocking Spectrum and the Shortcomings of Design Guidelines.* Nicos Makris and Dimitrios Konstantinidis. August 2001.

PEER 2001/06 *Development of an Electrical Substation Equipment Performance Database for Evaluation of Equipment Fragilities*. Thalia Agnanos. April 1999.

PEER 2001/05 *Stiffness Analysis of Fiber-Reinforced Elastomeric Isolators.* Hsiang-Chuan Tsai and James M. Kelly. May 2001.

PEER 2001/04 *Organizational and Societal Considerations for Performance-Based Earthquake Engineering.* Peter J. May. April 2001.

PEER 2001/03 *A Modal Pushover Analysis Procedure to Estimate Seismic Demands for Buildings: Theory and Preliminary Evaluation.* Anil K. Chopra and Rakesh K. Goel. January 2001.

PEER 2001/02 *Seismic Response Analysis of Highway Overcrossings Including Soil-Structure Interaction.* Jian Zhang and Nicos Makris. March 2001.

PEER 2001/01 *Experimental Study of Large Seismic Steel Beam-to-Column Connections.* Egor P. Popov and Shakhzod M. Takhirov. November 2000.

PEER 2000/10 *The Second U.S.-Japan Workshop on Performance-Based Earthquake Engineering Methodology for Reinforced Concrete Building Structures.* March 2000.

PEER 2000/09 *Structural Engineering Reconnaissance of the August 17, 1999 Earthquake: Kocaeli (Izmit), Turkey.* Halil Sezen, Kenneth J. Elwood, Andrew S. Whittaker, Khalid Mosalam, John J. Wallace, and John F. Stanton. December 2000.

PEER 2000/08 *Behavior of Reinforced Concrete Bridge Columns Having Varying Aspect Ratios and Varying Lengths of Confinement.* Anthony J. Calderone, Dawn E. Lehman, and Jack P. Moehle. January 2001.

PEER 2000/07 *Cover-Plate and Flange-Plate Reinforced Steel Moment-Resisting Connections.* Taejin Kim, Andrew S. Whittaker, Amir S. Gilani, Vitelmo V. Bertero, and Shakhzod M. Takhirov. September 2000.

PEER 2000/06 *Seismic Evaluation and Analysis of 230-kV Disconnect Switches.* Amir S. J. Gilani, Andrew S. Whittaker, Gregory L. Fenves, Chun-Hao Chen, Henry Ho, and Eric Fujisaki. July 2000.

PEER 2000/05 *Performance-Based Evaluation of Exterior Reinforced Concrete Building Joints for Seismic Excitation.* Chandra Clyde, Chris P. Pantelides, and Lawrence D. Reaveley. July 2000.

PEER 2000/04 *An Evaluation of Seismic Energy Demand: An Attenuation Approach.* Chung-Che Chou and Chia-Ming Uang. July 1999.

PEER 2000/03 *Framing Earthquake Retrofitting Decisions: The Case of Hillside Homes in Los Angeles.* Detlof von Winterfeldt, Nels Roselund, and Alicia Kitsuse. March 2000.

PEER 2000/02 *U.S.-Japan Workshop on the Effects of Near-Field Earthquake Shaking.* Andrew Whittaker, ed. July 2000.

PEER 2000/01 *Further Studies on Seismic Interaction in Interconnected Electrical Substation Equipment.* Armen Der Kiureghian, Kee-Jeung Hong, and Jerome L. Sackman. November 1999.

PEER 1999/14 *Seismic Evaluation and Retrofit of 230-kV Porcelain Transformer Bushings.* Amir S. Gilani, Andrew S. Whittaker, Gregory L. Fenves, and Eric Fujisaki. December 1999.

PEER 1999/13 *Building Vulnerability Studies: Modeling and Evaluation of Tilt-up and Steel Reinforced Concrete Buildings.* John W. Wallace, Jonathan P. Stewart, and Andrew S. Whittaker, editors. December 1999.

PEER 1999/12 *Rehabilitation of Nonductile RC Frame Building Using Encasement Plates and Energy-Dissipating Devices.* Mehrdad Sasani, Vitelmo V. Bertero, James C. Anderson. December 1999.

PEER 1999/11 *Performance Evaluation Database for Concrete Bridge Components and Systems under Simulated Seismic Loads.* Yael D. Hose and Frieder Seible. November 1999.

PEER 1999/10 *U.S.-Japan Workshop on Performance-Based Earthquake Engineering Methodology for Reinforced Concrete Building Structures.* December 1999.

PEER 1999/09 *Performance Improvement of Long Period Building Structures Subjected to Severe Pulse-Type Ground Motions.* James C. Anderson, Vitelmo V. Bertero, and Raul Bertero. October 1999.

PEER 1999/08 *Envelopes for Seismic Response Vectors.* Charles Menun and Armen Der Kiureghian. July 1999.

PEER 1999/07 *Documentation of Strengths and Weaknesses of Current Computer Analysis Methods for Seismic Performance of Reinforced Concrete Members.* William F. Cofer. November 1999.

PEER 1999/06 *Rocking Response and Overturning of Anchored Equipment under Seismic Excitations.* Nicos Makris and Jian Zhang. November 1999.

PEER 1999/05 *Seismic Evaluation of 550 kV Porcelain Transformer Bushings.* Amir S. Gilani, Andrew S. Whittaker, Gregory L. Fenves, and Eric Fujisaki. October 1999.

PEER 1999/04 *Adoption and Enforcement of Earthquake Risk-Reduction Measures.* Peter J. May, Raymond J. Burby, T. Jens Feeley, and Robert Wood.

PEER 1999/03 *Task 3 Characterization of Site Response General Site Categories.* Adrian Rodriguez-Marek, Jonathan D. Bray, and Norman Abrahamson. February 1999.

PEER 1999/02 *Capacity-Demand-Diagram Methods for Estimating Seismic Deformation of Inelastic Structures: SDF Systems*. Anil K. Chopra and Rakesh Goel. April 1999.

PEER 1999/01 *Interaction in Interconnected Electrical Substation Equipment Subjected to Earthquake Ground Motions.* Armen Der Kiureghian, Jerome L. Sackman, and Kee-Jeung Hong. February 1999.

PEER 1998/08 *Behavior and Failure Analysis of a Multiple-Frame Highway Bridge in the 1994 Northridge Earthquake.* Gregory L. Fenves and Michael Ellery. December 1998.

PEER 1998/07 *Empirical Evaluation of Inertial Soil-Structure Interaction Effects.* Jonathan P. Stewart, Raymond B. Seed, and Gregory L. Fenves. November 1998.

PEER 1998/06 *Effect of Damping Mechanisms on the Response of Seismic Isolated Structures.* Nicos Makris and Shih-Po Chang. November 1998.

PEER 1998/05 *Rocking Response and Overturning of Equipment under Horizontal Pulse-Type Motions.* Nicos Makris and Yiannis Roussos. October 1998.

PEER 1998/04 *Pacific Earthquake Engineering Research Invitational Workshop Proceedings, May 14–15, 1998: Defining the Links between Planning, Policy Analysis, Economics and Earthquake Engineering.* Mary Comerio and Peter Gordon. September 1998.

PEER 1998/03 *Repair/Upgrade Procedures for Welded Beam to Column Connections.* James C. Anderson and Xiaojing Duan. May 1998.

PEER 1998/02 *Seismic Evaluation of 196 kV Porcelain Transformer Bushings.* Amir S. Gilani, Juan W. Chavez, Gregory L. Fenves, and Andrew S. Whittaker. May 1998.

PEER 1998/01 *Seismic Performance of Well-Confined Concrete Bridge Columns.* Dawn E. Lehman and Jack P. Moehle. December 2000.

ONLINE PEER REPORTS

The following PEER reports are available by Internet only at http://peer.berkeley.edu/publications/peer_reports_complete.html.

PEER 2012/103 *Performance-Based Seismic Demand Assessment of Concentrically Braced Steel Frame Buildings.* Chui-Hsin Chen and Stephen A. Mahin. December 2012.

PEER 2012/102 *Procedure to Restart an Interrupted Hybrid Simulation: Addendum to PEER Report 2010/103.* Vesna Terzic and Bozidar Stojadinovic. October 2012.

PEER 2012/101 *Mechanics of Fiber Reinforced Bearings.* James M. Kelly and Andrea Calabrese. February 2012.

PEER 2011/107 *Nonlinear Site Response and Seismic Compression at Vertical Array Strongly Shaken by 2007 Niigata-ken Chuetsu-oki Earthquake.* Eric Yee, Jonathan P. Stewart, and Kohji Tokimatsu. December 2011.

PEER 2011/106 *Self Compacting Hybrid Fiber Reinforced Concrete Composites for Bridge Columns.* Pardeep Kumar, Gabriel Jen, William Trono, Marios Panagiotou, and Claudia Ostertag. September 2011.

PEER 2011/105 *Stochastic Dynamic Analysis of Bridges Subjected to Spacially Varying Ground Motions.* Katerina Konakli and Armen Der Kiureghian. August 2011.

PEER 2011/104 *Design and Instrumentation of the 2010 E-Defense Four-Story Reinforced Concrete and Post-Tensioned Concrete Buildings.* Takuya Nagae, Kenichi Tahara, Taizo Matsumori, Hitoshi Shiohara, Toshimi Kabeyasawa, Susumu Kono, Minehiro Nishiyama (Japanese Research Team) and John Wallace, Wassim Ghannoum, Jack Moehle, Richard Sause, Wesley Keller, Zeynep Tuna (U.S. Research Team). June 2011.

PEER 2011/103 *In-Situ Monitoring of the Force Output of Fluid Dampers: Experimental Investigation.* Dimitrios Konstantinidis, James M. Kelly, and Nicos Makris. April 2011.

PEER 2011/102 *Ground-motion prediction equations 1964 - 2010.* John Douglas. April 2011.

PEER 2011/101 *Report of the Eighth Planning Meeting of NEES/E-Defense Collaborative Research on Earthquake Engineering.* Convened by the Hyogo Earthquake Engineering Research Center (NIED), NEES Consortium, Inc. February 2011.

PEER 2010/111 *Modeling and Acceptance Criteria for Seismic Design and Analysis of Tall Buildings.* Task 7 Report for the Tall Buildings Initiative - Published jointly by the Applied Technology Council. October 2010.

PEER 2010/110 *Seismic Performance Assessment and Probabilistic Repair Cost Analysis of Precast Concrete Cladding Systems for Multistory Buildlings.* Jeffrey P. Hunt and Božidar Stojadinovic. November 2010.

PEER 2010/109 *Report of the Seventh Joint Planning Meeting of NEES/E-Defense Collaboration on Earthquake Engineering. Held at the E-Defense, Miki, and Shin-Kobe, Japan, September 18–19, 2009.* August 2010.

PEER 2010/108 *Probabilistic Tsunami Hazard in California.* Hong Kie Thio, Paul Somerville, and Jascha Polet, preparers. October 2010.

PEER 2010/107 *Performance and Reliability of Exposed Column Base Plate Connections for Steel Moment-Resisting Frames.* Ady Aviram, Božidar Stojadinovic, and Armen Der Kiureghian. August 2010.

PEER 2010/106 *Verification of Probabilistic Seismic Hazard Analysis Computer Programs.* Patricia Thomas, Ivan Wong, and Norman Abrahamson. May 2010.

PEER 2010/105 *Structural Engineering Reconnaissance of the April 6, 2009, Abruzzo, Italy, Earthquake, and Lessons Learned.* M. Selim Günay and Khalid M. Mosalam. April 2010.

PEER 2010/104 *Simulating the Inelastic Seismic Behavior of Steel Braced Frames, Including the Effects of Low-Cycle Fatigue.* Yuli Huang and Stephen A. Mahin. April 2010.

PEER 2010/103 *Post-Earthquake Traffic Capacity of Modern Bridges in California.* Vesna Terzic and Božidar Stojadinović. March 2010.

PEER 2010/102 *Analysis of Cumulative Absolute Velocity (CAV) and JMA Instrumental Seismic Intensity (I_{JMA}) Using the PEER–NGA Strong Motion Database.* Kenneth W. Campbell and Yousef Bozorgnia. February 2010.

PEER 2010/101 *Rocking Response of Bridges on Shallow Foundations.* Jose A. Ugalde, Bruce L. Kutter, and Boris Jeremic. April 2010.

PEER 2009/109 *Simulation and Performance-Based Earthquake Engineering Assessment of Self-Centering Post-Tensioned Concrete Bridge Systems.* Won K. Lee and Sarah L. Billington. December 2009.

PEER 2009/108 *PEER Lifelines Geotechnical Virtual Data Center.* J. Carl Stepp, Daniel J. Ponti, Loren L. Turner, Jennifer N. Swift, Sean Devlin, Yang Zhu, Jean Benoit, and John Bobbitt. September 2009.

PEER 2009/107 *Experimental and Computational Evaluation of Current and Innovative In-Span Hinge Details in Reinforced Concrete Box-Girder Bridges: Part 2: Post-Test Analysis and Design Recommendations.* Matias A. Hube and Khalid M. Mosalam. December 2009.

PEER 2009/106 *Shear Strength Models of Exterior Beam-Column Joints without Transverse Reinforcement.* Sangjoon Park and Khalid M. Mosalam. November 2009.

PEER 2009/105 *Reduced Uncertainty of Ground Motion Prediction Equations through Bayesian Variance Analysis.* Robb Eric S. Moss. November 2009.

PEER 2009/104 *Advanced Implementation of Hybrid Simulation.* Andreas H. Schellenberg, Stephen A. Mahin, Gregory L. Fenves. November 2009.

PEER 2009/103 *Performance Evaluation of Innovative Steel Braced Frames.* T. Y. Yang, Jack P. Moehle, and Božidar Stojadinovic. August 2009.

PEER 2009/102 *Reinvestigation of Liquefaction and Nonliquefaction Case Histories from the 1976 Tangshan Earthquake.* Robb Eric Moss, Robert E. Kayen, Liyuan Tong, Songyu Liu, Guojun Cai, and Jiaer Wu. August 2009.

PEER 2009/101 *Report of the First Joint Planning Meeting for the Second Phase of NEES/E-Defense Collaborative Research on Earthquake Engineering.* Stephen A. Mahin et al. July 2009.

PEER 2008/104 *Experimental and Analytical Study of the Seismic Performance of Retaining Structures.* Linda Al Atik and Nicholas Sitar. January 2009.

PEER 2008/103 *Experimental and Computational Evaluation of Current and Innovative In-Span Hinge Details in Reinforced Concrete Box-Girder Bridges. Part 1: Experimental Findings and Pre-Test Analysis.* Matias A. Hube and Khalid M. Mosalam. January 2009.

PEER 2008/102 *Modeling of Unreinforced Masonry Infill Walls Considering In-Plane and Out-of-Plane Interaction.* Stephen Kadysiewski and Khalid M. Mosalam. January 2009.

PEER 2008/101 *Seismic Performance Objectives for Tall Buildings.* William T. Holmes, Charles Kircher, William Petak, and Nabih Youssef. August 2008.

PEER 2007/101 *Generalized Hybrid Simulation Framework for Structural Systems Subjected to Seismic Loading.* Tarek Elkhoraibi and Khalid M. Mosalam. July 2007.

PEER 2007/100 *Seismic Evaluation of Reinforced Concrete Buildings Including Effects of Masonry Infill Walls.* Alidad Hashemi and Khalid M. Mosalam. July 2007.

The Pacific Earthquake Engineering Research Center (PEER) is a multi-institutional research and education center with headquarters at the University of California, Berkeley. Investigators from over 20 universities, several consulting companies, and researchers at various state and federal government agencies contribute to research programs focused on performance-based earthquake engineering.

These research programs aim to identify and reduce the risks from major earthquakes to life safety and to the economy by including research in a wide variety of disciplines including structural and geotechnical engineering, geology/seismology, lifelines, transportation, architecture, economics, risk management, and public policy.

PEER is supported by federal, state, local, and regional agencies, together with industry partners.

PEER Core Institutions:
University of California, Berkeley (Lead Institution)
California Institute of Technology
Oregon State University
Stanford University
University of California, Davis
University of California, Irvine
University of California, Los Angeles
University of California, San Diego
University of Southern California
University of Washington

PEER reports can be ordered at http://peer.berkeley.edu/publications/peer_reports.html or by contacting

Pacific Earthquake Engineering Research Center
University of California, Berkeley
325 Davis Hall, mail code 1792
Berkeley, CA 94720-1792
Tel: 510-642-3437
Fax: 510-642-1655
Email: peer_editor@berkeley.edu

ISSN 1547-0587X